2017

The effects of wing flexibility on the flight performance and stability of flapping wing micro air vehicles

James Edward Bluman

THE EFFECTS OF WING FLEXIBILITY ON THE FLIGHT PERFORMANCE AND STABILITY OF FLAPPING WING MICRO AIR VEHICLES

by

JAMES EDWARD BLUMAN

A DISSERTATION

Submitted in partial fulfillment of the requirements
for the degree of Doctor of Philosophy
in
The Department of Mechanical and Aerospace Engineering
to
The School of Graduate Studies
of
The University of Alabama in Huntsville

HUNTSVILLE, ALABAMA

2017

In presenting this thesis in partial fulfillment of the requirements for a doctoral degree from The University of Alabama in Huntsville, I agree that the Library of this University shall make it freely available for inspection. I further agree that permission for extensive copying for scholarly purposes may be granted by my advisor or, in his/her absence, by the Chair of the Department or the Dean of the School of Graduate Studies. It is also understood that due recognition shall be given to me and to The University of Alabama in Huntsville in any scholarly use which may be made of any material in this thesis.

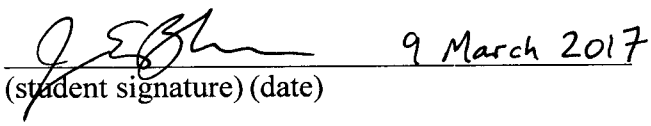

9 March 2017

(student signature) (date)

DISSERTATION APPROVAL FORM

Submitted by James Edward Bluman in partial fulfillment of the requirements for the degree of Doctor of Philosophy in Mechanical Engineering and accepted on behalf of the Faculty of the School of Graduate Studies by the dissertation committee.

We, the undersigned members of the Graduate Faculty of The University of Alabama in Huntsville, certify that we have advised and/or supervised the candidate on the work described in this dissertation. We further certify that we have reviewed the dissertation manuscript and approve it in partial fulfillment of the requirements for the degree of Doctor of Philosophy in Mechanical Engineering.

3/9/2017 Committee Chair
Dr. Chang-won Kang (Date)

3/9/2017
Dr. Farbod Fahimi (Date)

3/9/17
Dr. D. Brian Landrum (Date)

03/09/2017
Dr. Yuri Shtessel (Date)

3/9/17
Dr. Q.H. Ken Zuo (Date)

3/10/17 Department Chair
Dr. D. Keith Hollingsworth (Date)

03/21/17 College Dean
Dr. Shankar Mahalingam (Date)

4/11/17 Graduate Dean
Dr. David Berkowitz (Date)

ABSTRACT

School of Graduate Studies
The University of Alabama in Huntsville

Degree Doctor of Philosophy in Mechanical Engineering College/Dept. Engineering/Mechanical and Aerospace Engineering

Name of Candidate James Edward Bluman

Title The Effects of Wing Flexibility on the Flight Performance and Stability of Flapping Wing Micro Air Vehicles

Insect wings are flexible. However, the influence of wing flexibility on the flight dynamics of insects and flapping wing micro air vehicles is unknown. Most studies in the literature consider rigid wings and conclude that the hover equilibrium is unstable. This dissertation shows that a flapping wing flyer with flexible wings exhibits stable natural modes of the open loop system in hover, never reported before. The free-flight insect flight dynamics is modeled for both flexible and rigid wings. Wing mass and inertia are included in the nonlinear equations of motion. The flapping wing aerodynamics are modeled using a quasi-steady model, a well-validated two dimensional Navier Stokes model, and a coupled, two dimensional Navier Stokes – Euler Bernoulli beam model that accurately models the fluid-structure interaction of flexible wings. Hover equilibrium is systematically and efficiently determined with a coupled quasi-steady and Navier-Stokes equation trimmer. The power and stability are reported at hover while parametrically varying the pitch axis location for rigid wings and the

structural stiffness for flexible wings. The results indicate that the rigid wings possess an unstable oscillatory mode mainly due to their pitch sensitivity to horizontal velocity perturbations. The flexible wings stabilize this mode primarily by adjusting their wing shape in the presence of perturbations. The wing's response to perturbations generates significantly more horizontal velocity damping and pitch rate damping than in rigid wings. Furthermore, the flexible wings experience substantially less wing wake interaction, which, for rigid wings, is destabilizing. The power required to hover a fruit fly with actively rotating rigid wings varies between 16.9 and 34.2 W/kg. The optimal power occurs when the pitch axis is located at 30% chord, similar to some biological observations. Flexible wings require 23.1 to 38.5 W/kg. However, flexible wings exhibit more stable system dynamics and allow for simpler and lighter designs since they do not require pitch actuation mechanisms. This study is the first to evaluate the impact of wing flexibility on the hovering stability of flapping flyers, which can explain the ranges of flexibility seen in insects and can inform designs of synthetic flapping wing robots.

Abstract Approval: Committee Chair 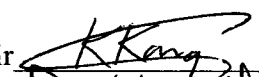

Department Chair 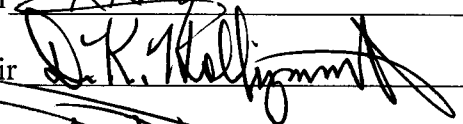

Graduate Dean 

ACKNOWLEDGMENTS

First and foremost, I must thank my advisor, Dr. Chang-kwon Kang. He has been an outstanding mentor and guide in this intellectual journey. He allowed me freedom to explore different facets of my research in various ways, but he always ensured that I stayed on task and focused on the ultimate goal. And his intellectual acumen and high standards of excellence in every facet of academic inquiry are an inspiration to me. I sincerely appreciate my committee for all of their contributions in both classes and in research: Dr. Fahimi, Dr. Landrum, Dr. Shtessel and Dr. Zuo. I would also like to thank the UAH staff, especially Euan Holton, Claudia Meyering, and Melissa Brown.

I also want to thank my fellow graduate students, Madhu Sridhar, Deepa Kodali, Louis Salmon, Kabilan Nedunchezian, and Jeremy Pohly. I particularly want to thank Madhu, who really keeps Dr. Kang's lab, and the ATOM lab in general, up and running. I learned so much from Madhu about working in a Linux environment, coding in Fortran, and other grad school life skills.

I also want to thank the US Army for giving me the time and funding support to pursue my Ph.D., and Colonels Crawford and Vanpoppel for giving me this opportunity. I also want to thank my wife, Kelly, and our children for all of their support.

"For what shall it profit a man, if he shall gain the whole world, and lose his soul?" -- Jesus of Nazareth

TABLE OF CONTENTS

LIST OF FIGURES

FIGURE PAGE

LIST OF TABLES

TABLE PAGE

LIST OF SYMBOLS

A	=	system matrix	varies
AoA	=	local aerodynamic angle of attack	[degrees]
$\mathbf{a}$	=	acceleration vector	[m/s^2]
B	=	control matrix	varies
b	=	denotes a body parameter of reference frame	[1]
C_α	=	square wave smoothing parameter for pitch angle	[1]
$C_{L,D,M}$	=	coefficient of lift, drag, or moment	[1]
CG	=	center of gravity of a body, lower case use in subscripts	[1]
c	=	chord	[m]
E	=	Young's modulus	[Pa]
F,$\mathbf{F}$	=	component of force, force vector	[N]
f	=	flapping frequency	[1/s]
f_1	=	first natural frequency of the wing	[1/s]
G,G	=	gravitational acceleration, units thereof	[m/s^2], [1]
h_s,h_s^*	=	thickness of the wing, thickness to chord ratio of the wing	[m], [1]
k	=	reduced frequency	[1]
I	=	mass moment of inertia	[kg-m^2]
$\mathbf{i}$,$\mathbf{j}$,$\mathbf{k}$	=	unit vectors of a reference system	[1]
LEV	=	leading edge vortex	[1]
M,$\mathbf{M}$	=	moment component, moment vector	[Nm]
$M_{u,w,q}$	=	stability derivative relating to the moment about the y_b axis	[varies]
m_b,m_w	=	mass of insect body or wing	[kg]
o	=	wing root location	[1]
P	=	power	[Watts]
p	=	pressure, also a reference point on the wing	[Pa]

p,q,r	=	angular velocities of the body in the body frame	[rad/s]
R	=	span; also rotation matrix	[m], [1]
Re	=	Reynolds number	[1]
$\mathbf{r}$	=	position vector	[m]
$r_1(v)$	=	radius to the first moment of virtual wing mass	[m]
r_2	=	radius to the second moment of wing area	[m]
S	=	planform area of a single wing	[m^2]
TEV	=	trailing edge vortex	[1]
t	=	time	[s]
U	=	maximum flapping velocity of wing during a full stroke	[m/s]
$\mathbf{u}$	=	vector of control inputs	[varies]
u,v,w	=	x-, y-, and z-components of velocity (body frame)	[m/s]
$\mathbf{V},\mathbf{v}$	=	velocity vector field of flow, velocity vector of a point	[m/s]
$\hat{v}$	=	Nondimensional virtual mass of wing	[1]
W	=	weight	[N]
$X_{u,w,q}$	=	stability derivative relating to the force in the x_b-direction	[varies]
$\mathbf{x}$	=	vector of state variables	[varies]
x,y,z	=	translational coordinates of a point or body	[m]
x_p/c	=	pitch axis location along chord	[1]
$Z_{q,u,w}$	=	stability derivative relating to the force in the z_b-direction	[varies]
A	=	pitch amplitude	[degrees]
α	=	instantaneous pitch of wing	[degrees]
α_φ	=	pitch phasing parameter	[1]
β	=	stroke plane angle	[degrees]
$\Delta\tau_R$	=	duration of pitch rotation in terms of flapping periods	[1]
δ	=	vertical deviation angle; also a numerical perturbation	[degrees]
Z	=	flapping amplitude	[degrees]
ζ	=	instantaneous stroke or flapping angle of the wing	[degrees]
ζ_φ	=	flapping offset angle	[degrees]
θ	=	pitch angle of body	[degrees]
λ	=	eigenvalues of the system matrix	[1/s]
ν	=	kinematic viscosity of the fluid	[m^2/s]
Π_0	=	effective inertia, in Euler Bernoulli equation	[1]

Π_1	=	effective stiffness, in Euler Bernoulli equation	[1]
ρ	=	density of the fluid	[kg/m^3]
ρ_w	=	density of the wing structure	[kg/m^3]
σ	=	real part of eigenvalues: rate of growth or decay of response	[1/s]
τ	=	nondimensional time, expressed in periods of flapping motion	[1]
ω	=	angular velocity, also natural frequency of body motion	[rad/s]

Superscripts

^	=	nondimensionalized distance (usually with respect to chord)
*	=	nondimensionalized parameter (usually in Navier Stokes equations)
.	=	time derivatives
’	=	denotes force per unit span or intermediate reference frame
~	=	matrix form of the cross product
^{T}	=	Matrix or vector transpose

Subscripts

Aero	=	aerodynamic contribution (usually to force, moment or power)
am	=	added mass
b	=	body
cg	=	center of gravity of the body
Iner	=	inertial contribution (usually to force, moment or power)
o	=	wing root
p	=	arbitrary point
req	=	required
rot	=	rotational (usually refers to rotational lift or force)
sp	=	stroke plane
trans	=	translational (usually refers to translational lift or force)
usp	=	upright stroke plane
w	=	a wing parameter or references frame
wg	=	wing center of gravity location
wo	=	from the wing root, i.e. moment of inertia about the wing root

Note: subscripts that appear before a vector indicate the reference frame in which it is defined. Subscripts that appear after a vector indicate the body, point, or axis (in the case of angular velocities and accelerations) to which it is referring.

CHAPTER 1

INTRODUCTION

1.1. Background and Motivation

Small flapping wing flyers such as insects are truly remarkable creatures. Across the insect class *Insecta,* they exhibit an enviable slate of characteristics that includes highly agile flight, the ability to perform long migrations, and the ability to carry excess loads approaching their own weight. They clearly must possess onboard energy stores, propulsion mechanisms, and control systems sufficient to achieve these aeronautical feats, as well as the sensing and processing abilities to command them. Furthermore, the physics of flapping small wings at high flapping frequencies in a low Reynolds number environment has only recently been elucidated. Therefore, the study of insect flight of a biological flyer or flapping wing micro air vehicle (FWMAV) is a complex endeavor. However, these enviable characteristics make insects a natural source of biomimicry for scientists and engineers attempting to design and construct artificial flapping wing micro air vehicles.

The design of such small flight vehicles presents many well-known challenges including aerodynamics, flight dynamics, power storage and transmission, sensory mechanisms, and control among others. In each field, significant progress has been made

in recent years, but an integrated framework for modeling and designing these complex systems remains elusive. For example, there is still open debate concerning the stability of insects in hover and the best way to assess it. There have been multiple studies on the longitudinal stability of hovering insects. These analyses have featured increasing modeling fidelity on multiple fronts. Virtually all previous work on the stability of FWMAVs conclude that the longitudinal dynamics of hover include an unstable oscillatory mode. However, the one modeling assumption that all previous work shares is that the wings are rigid.

The primary motivation for studying the flight mechanics of flexible wings is the recent observations of Kang and Shyy [1,2] based on their work with flexible wings. They demonstrate that the many conclusions based on rigid wing analysis cannot be blindly applied in the case of flexible wings with wing stiffness that is representative of live insects. Indeed, they showed that the force histories of flexible wings are significantly different from those produced by rigid wings. If the force production is different, it is logical to assume that the stability and power consequences might also be different.

Accurately modeling the flight dynamics of an insect of FWMAV with flexible wings is no easy task. The very nature of fluid-structure interaction demands tight two-way coupling between the aerodynamic and structural dynamic models. In order to capture all of the aerodynamic phenomena occurring in this unique fluid dynamic regime, direct simulation of the full Navier Stokes (NS) equations is required, which is computationally expensive. These equations must be coupled to an appropriate flexible beam or plate model since wing motion affects the aerodynamic forces, which in turn

affects the motion of the wing. Adding an additional layer of coupling by including the flight dynamics of the body raises new questions and challenges that shall be addressed in this study, including the extent to which body motion affects the passive wing motion and forces. Additionally, analysis of flight dynamics usually focuses on the natural modes of motion, which assumes the system is in equilibrium. Determining the required control inputs and initial conditions to place flexible wing flight simulation into equilibrium is also challenging given the three-way coupled nature of the problem.

A reasonable approach to understand the complex coupled nonlinear physics of flexible flapping wings is first to model and understand the implications of various rigid wing configurations. In the many studies on the aerodynamics, stability and control of insects and FWMAVs in recent years, we identified open questions regarding the following important modeling concerns:

1. An often neglected parameter in characterizing the wing rotation is the pivot point location, which significantly affects the instantaneous aerodynamic force generation [3]. In a study focused on minimizing the power required to hover for various insects, Berman and Wang [4] varied eleven different kinematical parameters in order to optimize flapping efficiency, but they did not examine the influence of changing the pitch axis, nor did they consider the stability implications of minimal-power kinematics. A recent study by Taha et al. [5] did explicitly examine the effect of pitch axis location, but their aerodynamic model was so oversimplified as to neglect many of the primary features that result from changing the pitch axis. The effect of the pitch axis location on the vehicle

dynamics and stability, as well as resulting aerodynamic performance is still inconclusive.

2. The role of wing rotation and wing wake interaction on the power and stability of insects and FWMAVs has not been adequately addressed. Even though these two phenomena are significant features in the flapping wing flight of rigid wings, there are few studies which even mention these effects, and most studies omit them from their modeling [5–11].
3. Despite the recent work [1,2,12,13] on the role of flexibility in the aerodynamics of flapping wing flyers, the role of wing flexibility in the stability and power consumption of insects and FWMAVs in free flight has not been previously investigated.

Finally, many previous studies do not consider the FWMAV system in equilibrium [11,14–18]. Most often, the attempt is made to ensure that lift balances weight, but full free-flight equilibrium is rarely considered. A key element of this study, therefore, is that all parametric analyses will be done at or near equilibrium. Beyond ensuring that lift balances weight, we determine both control inputs and initial conditions to ensure all accelerations are negligibly small in all degrees of freedom. Without this constraint on the problem, parametric studies are of little value in making design decisions since any gains in power that might be achieved by adjusting kinematics might be immediately lost when other parameters must change to balance horizontal forces or moments.

Additionally, the stability implications of adjusting certain parameters are equally important as power considerations. If a certain kinematic pattern is advantageous from

the standpoint of lift production or efficiency, but it is highly unstable, it might not be a suitable choice for a FWMAV. Aerodynamic force generation, performance and stability depend on multiple control inputs, which means that these different design considerations are likely coupled. Evaluating the coupled, multi-input system at equilibrium ensures that we do not assign more weight to one facet of the problem than another.

1.2. Research Objectives

The overarching objective of this study is to address the third assumption in Section 1.1 and determine the effect of wing flexibility in the chordwise direction on the longitudinal stability and flight performance of a hovering bumblebee. Based on Combes and Daniel's observation that insect wings are orders of magnitudes more flexible in the chordwise direction than in the spanwise direction [19,20], we consider only the chordwise flexibility.

Prior research indicates that the longitudinal and lateral-directional modes of flapping wing hovering flight are largely decoupled [7]. We focus on the longitudinal stability of the FWMAV because we expect that considering chordwise flexibility and the resulting passive pitch will have the most significant effect on the pitching moment of the wing and the timing of aerodynamic force generation. The shape adaptation associated with wing flexibility changes the effective angle of attack and hence the aerodynamic outcomes [1,21]. The pitching moment of the wing and the shape of the force histories affect the longitudinal motion of the flapping wing flyer and will likely influence the nature of the overall system dynamics. Therefore, we also investigate the effects of the pitch axis location, and wing wake interaction on the aerodynamic performance and flight stability of the flapping wing flyer, which were the first and the second assumptions in

Section 1.1, as secondary, but supporting, objectives. We further determine the power required to hover by directly calculating the power required to achieve wing motion in order to compare the flight performance of a flexible wing at hover to its rigid counterpart.

In summary, the specific objectives of this study are as follows.

1. To determine the effect of the varying the wing pitch axis on the required power and longitudinal stability of a FWMAV in hover.

2. To determine the influence of wing rotation and wing wake interaction on the power and longitudinal stability of a FWMAV in hover.

3. To determine the influence of utilizing flexible wings on the required power and longitudinal stability of a FWMAV in hover.

1.3. Dissertation Outline

This dissertation begins with a literature review in Chapter 2. In the literature review we present the previous work that formed the foundation of the research contained in this dissertation. Pertinent details of previous studies pertaining to the aerodynamics of both rigid and flexible wings as well as the flight dynamics of rigid wings are described in detail. Chapter 3 is an extensive survey of the modeling tools and analytical and computational methods used in the course of the study. We discuss the new material that we developed and applied in pursuit of our research goal. These include enhancements that we made to the quasi-steady aerodynamic model and a trim procedure that is able to find equilibrium for a vehicle in hover using both the Navier-Stokes (NS) solutions for rigid wings and the coupled NS – Euler Bernoulli beam equations that are needed to study flexible wings.

The results are presented in two different chapters. Chapter 4 covers the flight dynamics of rigid wings while considering parametric variation of the pitch axis location. The results of this rigid wing study unveil important insights that are required to understand the results of the flexible wing study. They also provide validation of our developed model and a basis of comparison for the flexible wing results. Finally, we provide the flexible wing results in Chapter 5. Within each chapter, we present our results in the following order: the wing kinematics, the required trim inputs, the resulting aerodynamic forces, the required power, and the open loop stability. In the stability section, we focus on the open loop poles and the relevant stability derivatives in order to identify the source of the stability or instability, as the case may warrant. The conclusion is presented in Chapter 6 which highlights the original contributions of this work and provides recommendations for future work as well.

CHAPTER 2

LITERATURE SURVEY

2.1. Overview and Highlights

Although a vast body of literature is available on flapping wing flight, it remains an active area of research on multiple fronts. The last few decades have seen an explosion of research activities by biologists, scientists, and engineers conducting observational studies on live insects, experiments on robotic flapping wing devices both in air and in oil tanks, analytical work, numerical studies of both rigid and flexible wing aerodynamics, flight dynamic simulations, and optimization and control studies. This literature survey highlights the findings and models that have particular bearing on this study. Additionally, in the following chapters, both models and results that confirm or seem to contradict previous work are emphasized.

Key lessons that are pertinent to this work are summarized below and described more in detail in Sections 2.2 to 2.6.

- Insect wings produce aerodynamic forces via four distinct aerodynamics mechanisms: circulatory "translational lift" associated with an attached leading edge vortex, "rotational lift" associated with wing rotation while flapping, "added mass" forces that develop when the wing accelerates, wake effects called wake capture or wing wake

interaction. All four of these influences are important in both rigid and flexible wings, but the role that each plays in flexible versus rigid wings changes significantly.

- Rigid wings can be actively pitched. The timing of the wing pitching motion relative to the flapping motion has a large influence on both the amount of lift produced and on the power required. Pitch rotations that are timed to occur prior to the flapping motion (termed advanced rotation) produce significantly more lift than delayed rotations, but also require significantly more pitching power to achieve.

- Passive pitch is possible with a wise selection of the pitch axis near the leading edge and results from both inertial and aerodynamic influences. The passive pitch of rigid wings is typically delayed with respect to the flapping motion, and so it does not produce as much lift as actively rotated wing, all else being equal. Passive pitch can also be achieved if the wings are flexible. The phasing of passive pitch is dependent on multiple factors.

- Flexible wings produce lift differently than their rigid counterparts. In part due to the instantaneous wing shape adaptation and partly because they experience much less wing wake interaction. They also appear to generate a given amount of lift with a lower power coefficient, resulting in higher efficiency.

- The required power to achieve flapping wing flight at the insect scale (in air) consists of both aerodynamic and inertial forces. For rigid wings, both contributions are of the same order of magnitude.

- Despite the nonlinearity of the equations of motion for flapping wing flight, the behavior of the system is typically determined by finding the open loop poles of the linearized system in equilibrium.

2.2. The Flapping Wing Aerodynamics of Rigid Wings

A host of research has been performed in order to understand the complex aerodynamics of rapidly moving wings at this flow regime where the Reynolds Number is of the range $Re = O(10^2)$-$O(10^4)$ [21–24]. Of particular interest in the analysis of this study on flapping wing stability is the experimental work of Sane and Dickinson [25–27], who used a dynamically-scaled model rigid wing in an oil tank. By conducting experiments using a robotic wing immersed in mineral oil, they identified four lift production mechanisms: the circulatory forces produced by the delayed stall of a wing in translation at high angles of attack (i.e. translational lift), the forces generated by circulation during wing rotation (i.e. rotational forces), the forces generated by accelerating a fluid (i.e. added mass forces), and the forces generated when the wing interacts with vortical structures shed in previous strokes (i.e. wing wake interaction or wake capture).

In addition to providing these important mechanisms of lift production that combine to make flight at low Reynolds number possible, they provided a straightforward quasi-steady model that is efficient for use in stability and control analysis because it has low computational cost. Based partly on the theoretical work of Theodorsen [3] and partly on their own experiments, their quasi-steady aerodynamic model accounts for the translational lift, the rotational lift, and the added mass forces. Quasi-steady models assume that the aerodynamic forces and moments on the wing depend on the instantaneous wing velocity and acceleration [22]. The wing wake interaction is a nonlinear phenomenon involving history effects, such as the vortices shed in the previous strokes interacting with the wing. A closed form analytical expression has

not yet been developed for the wing wake interaction and is omitted from the quasi-steady models of flapping wings [6].

One of their most seminal findings is the large effect that the timing of wing rotation has on the amount of lift produced by a flapping wing. More lift is created if the wing is actively rotated in an advanced rotation such that the pitch motion precedes the flapping motion. Dickinson et al. [25] showed that an 8% change in the timing of rotation from symmetric to advanced increases the lift produces by 32%, all else being equal. Additionally, they showed that the pitch axis of the wing can have a significant effect on the rotational lift produced and that the lift produced can vary from theoretical predictions by a factor of up to 2.25 [27].

Other studies have also demonstrated the various physical mechanisms of lift production at these low Reynolds numbers and have indicated the means by which this lift and thrust force can be made in the most efficient manner possible [4,13,23]. Several computational studies based on solutions to the Navier-Stokes equations are particularly informative [28,29]. In many ways, these studies have confirmed earlier experimental work, also showing that the lift can be decomposed into translational, rotational, added mass, and wing wake interactional components. They show that despite operating at a very large angle of attack (*AoA*), the wings at these low Reynolds numbers do not experience stall in the classic sense, which leads to the large region of positive lift generated during wing translation despite the high *AoA* [29].

These studies have also illuminated the importance of wing wake interaction and the ability of vortices shed in previous strokes to enhance the lift production, typically immediately following course reversal. Tang et al. [30] show that the wake-capture

mechanism of enhancing lift is only present in normal hovering kinematics (where a single edge remains the leading edge in both halves of the stroke) vice a water treading mode (where the leading edge and trailing edge of the wing alternate in each half stroke). Thus, we confine our kinematics to normal hovering where the wing orientation is vertical at stroke reversal. Tang et al. [30] also show that for low Reynolds numbers ($Re < 300$) and rigid flapping wings, the viscous effects tend to dissipate vorticity enough that the forces become half-cycle periodic, whereas at higher Reynolds numbers, the aerodynamic force histories are distinctly asymmetric.

Additionally, Tang and Sun [29], Ansari et al. [24], and Trizila et al. [31] note that wake effects are not confined to the near-field wake, but far-field wake effects are also important. In particular, a downwash associated with a reversed von Karman vortex street develops in hovering wings. When the wing travels through this downwash, the instantaneous effective angle of attack can reduce, resulting in a wake valley with a lowered lift.

Thus, wing wake interaction can both add to and subtract from the lift production depending on the wing kinematics and vortex orientation. These features are depicted in Figure 2.1, where we present a time history of the lift coefficient C_L across a single flapping cycle. The lift coefficient is defined in Section 3.3. Trizila et al. [31] also demonstrated that the comparison between 3D and 2D aerodynamic calculations is quite similar for most plunge motions using pitch angles and flapping amplitudes seen in the natural world and also used in this study.

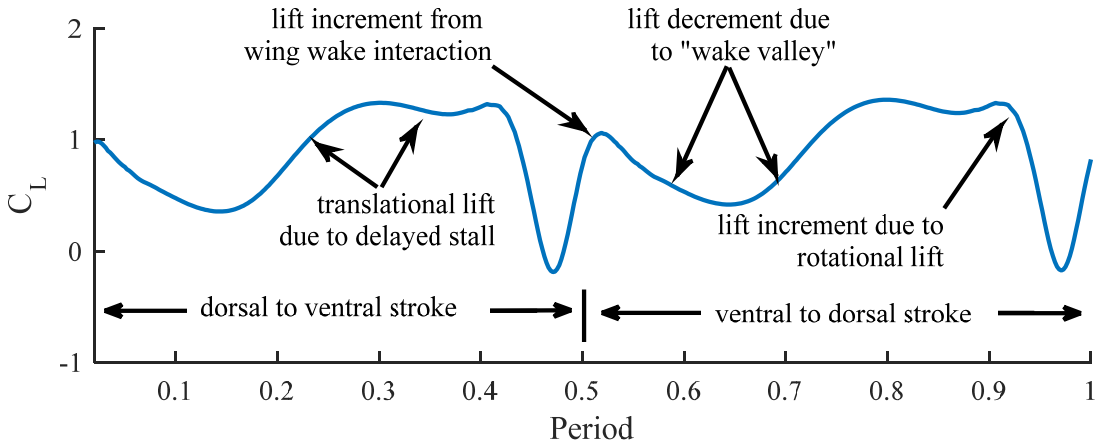

Figure 2.1. Lift coefficient across a full flapping cycle for a wing with advanced pitching rotation, depicting the regions associated with wing wake interaction, translational lift from delayed stall, and rotational lift.

2.3. Wing Kinematics

The aerodynamic forces are directly dependent on the imposed wing kinematics. There are three ways to represent wing kinematics that appear frequently in the literature: kinematics which seek to replicate insect wing motions exactly [32–34], the kinematics of Sun et al. [15,35], the kinematics of Berman and Wang [4], and first order harmonic motions [31,36].

Live insects utilize a wide range of kinematic patterns that are typically not sinusoidal in nature [32,33,37], however the motion is nearly periodic in the hover condition. Additionally, the kinematics between different insect species can vary significantly. Therefore, to model and analyze the underlying physical mechanisms that may be universal to most flapping wing insects, an abstracted kinematics is often employed. Sun and co-workers [7,15,17,18,35,38–40] rely on piecewise pure trigonometric functions in order to produce abstracted kinematics. In their work, they typically represent flapping motion using a cosine function. For pitching motion, they

typically utilize a piecewise function that permits rapid pitch rotations along a sinusoidal profile (per equation (2.1)) followed by portions of the stroke where the pitch is held strictly constant [35].

$$\alpha = \alpha_d + a\left\{\left(t - t_1\right) - \frac{\Delta t_r}{2\pi}\sin\left[\frac{2\pi}{\Delta t_r}\left(t - t_1\right)\right]\right\} \quad t_1 \le t \le t_1 + \Delta t_r \tag{2.1}$$

In Meng, Xu and Sun [35] as well as Wu, Zhang, and Sun [17], they define $a = \left(180 - \alpha_u - \alpha_d\right)/\Delta t_r$, and the rapid pitch rotation occurs between t_1 and $t_1 + \Delta t_r$. Although these kinematics have the benefit of expressing the pitch rotation in an intuitive sense such that the pitch motion occurs during a designated portion of the stroke (i.e. Δt_r), the higher derivatives of these piecewise functions are not smooth. In the course of our NS simulations, these unsmooth accelerations result in discontinuities and associated force peaks that are simply an artifact of the chosen kinematics. Therefore, we utilize an alternative method of producing abstracted kinematics by Berman and Wang [4] that is not subject to this problem.

Berman and Wang propose a set of functions for all three angular degrees of freedom for the wing: flapping, pitching, and vertical deviation angle (which is omitted in this study). Their relations allow the flapping angle to vary from a triangular wave to a sinusoidal wave, and the pitching angle can vary from a sinusoidal wave to a square wave. These kinematics are used in the present study, and we plot several representative wing motions in Figure 2.2. Additionally, a more complete discussion is provided in Section 3.3.

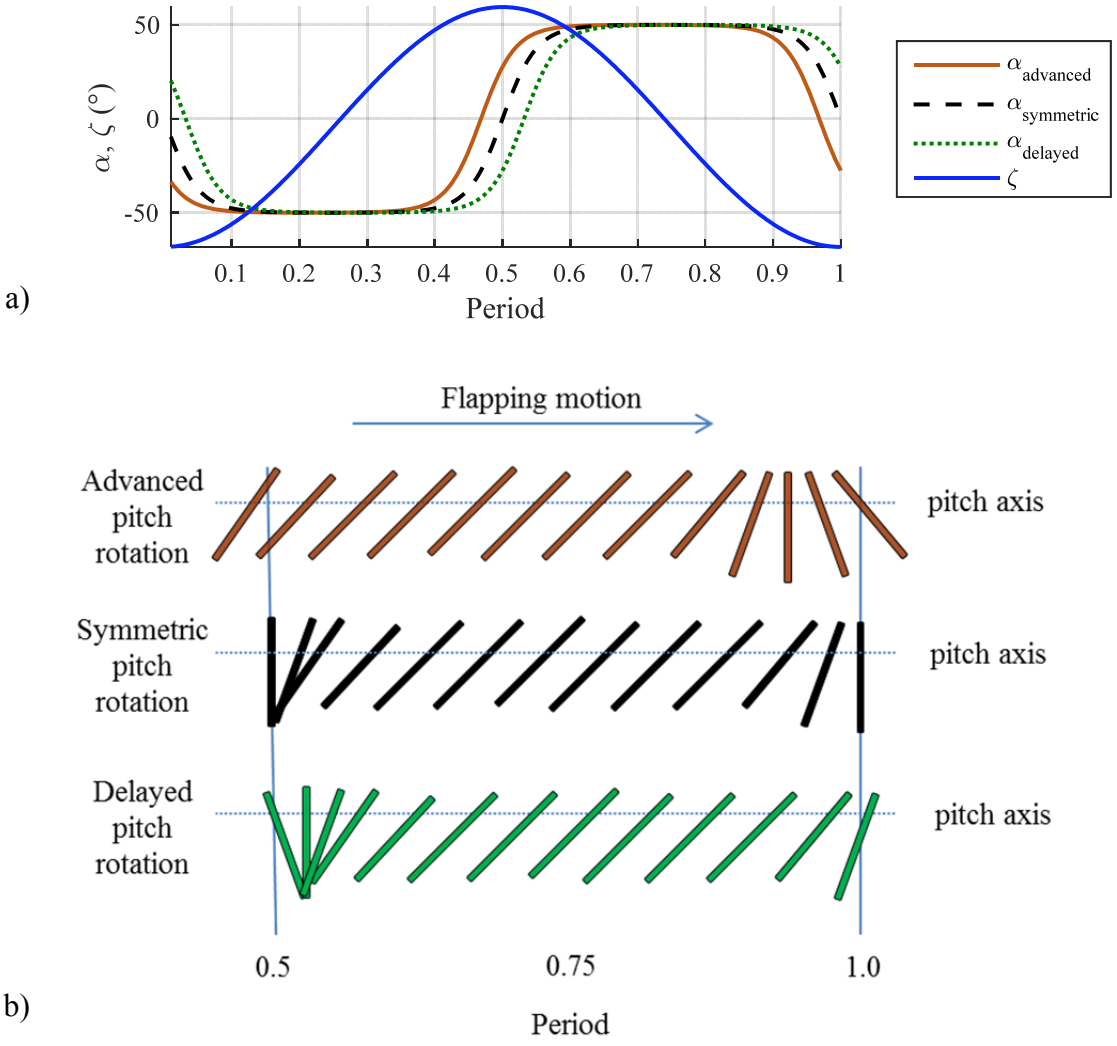

Figure 2.2. Time history (a) of pitch angles α for advanced (brown), symmetric (black), and delayed (green) with respect to sinusoidal flapping motion ζ (blue); position and orientation of the wings (b) at evenly spaced intervals illustrating the phasing of the pitch angle as advanced, symmetric or delayed.

Faruque and Humbert [9,41,42] used a similar formulation of the pitch angle in their stability and control studies. Finally, several computational studies on flapping wing aerodynamics were performed using first-order harmonic motion for both flapping and pitching motions [31,36]. However, none of the flight dynamics or control studies utilize these kinematics, so we do not consider them in this study.

All of the approaches mentioned thus far assume active pitching - that is, instantaneous pitch angles that are prescribed. In active pitching, the timing of the pitch motion relative to the flap motion plays an important role in the resulting aerodynamics [4,23,25]. The timing of the wing rotation is classified as advanced, symmetric, or delayed rotation. In advanced rotation, the pitch rotation starts before stroke reversal; in symmetric motion, half of the pitching occurs before stroke reversal, and in delayed motion, less than half the pitch rotation occurs before stroke reversal (Figure 2.2).

Finally, in addition to the work that has gone into studying the active rotation of flapping wings in both experiments and computational studies, several researchers have examined the possibility of wings achieving purely passive rotation, and the kinematics that are relevant to such an arrangement. Although insects possess the musculature to actively rotate their wings, it is not known if they rely on active or passive rotation in a typical stroke [43,44].

Bergou and Wang [37] demonstrate, based on their quasi-steady aerodynamics model, that purely passive pitching is possible in dragonfly wings by showing that the power required to pitch the wings in a manner representative of true dragonflies is purely negative. Additionally, Ennos argues that a signature of passive rotation is a torsion wave that deforms the wing from tip to root (vice root to tip) and these torsion waves are observed in several species [45]. Several researchers using robotic devices in air demonstrate the ability to fly using passive rotation. Whitney and Wood [43] describe how passive rotation is possible using an analytical model for passive pitch. They also compare the model against experimental results from a test stand that was used in the development of the Harvard RoboBees.

Additionally, Khan and Agrawal developed a robotic flapping mechanism [46] and found kinematics that could achieve passive pitch rotation [47]. Ishihara et al. developed a lumped torsional flexibility model to predict the passive wing pitch changes of a flapping wing, and showed that the resulting passive rotations could support the weight of a drone fly [48]. Other robotic devices rely on passive rotation or passive flexible deformation to achieve lift or thrust [49,50]. Thus, passive pitching of both rigid and flexible wings has been shown to produce meaningful amounts of lift while flapping in air. It is not clear what the stability or power implications of such concepts are relative to their actively rotated counterparts, particularly in free flight where their pitch response might be affected by the body dynamics.

2.4. The Flapping Wing Aerodynamics of Flexible Wings

Recently, several studies [1,2,12] have demonstrated the importance of considering wing flexibility in aerodynamic analysis and its significant impact on the aerodynamic force generation mechanisms [1], efficiency, and the timing of passive wing kinematics [13,51]. Flexible wings tend to require less power to flap because the passive deflection produces less drag and torque penalties [51]. Other studies have shown that the maximum efficiency of lift production in air occurs when the flapping frequency is below (approximately 50%) the first natural frequency of the wing due to its stiffness [12,13,52,53].

Wing flexibility might affect longitudinal stability as well for three reasons. The first is that the pitching is purely passive. It results from the dynamic balance of the wing's inertia, the fluid dynamic forces generated by the wing's motion, and the structural stiffness of the wing. This passive pitch results in time histories of lift and drag that are

different from rigid wings. Rigid wings in hover typically exhibit lift histories that have at least two noticeable lift peaks in each half stroke. The first peak results primarily from wing wake interaction. The second peak results either from delayed stall or from rotational lift, depending on the kinematics and the pitch axis location. Flexible wings typically have a single prominent lift peak more towards the center of each half stroke [1]. This single peak occurs because the wing flexibility delays flow separation and also affects the strength and location of shed vortices. Therefore the wing wake interaction (which typically causes the first peak in rigid wings) is significantly mitigated in flexible wing [1]. The influence of these different lift histories on the stability of the vehicle has not been investigated. Finally, the influence of wing wake interaction on the FWMAV stability is itself an open research question, and whether the flexibility of the wing further affects the stability due to different wing wake interaction has also not been previously investigated. The dynamics of the flyer itself might also influence the wing shape deformation and the resulting aerodynamics.

2.5. Power Required for Flapping Wing Flight

In addition to determining wing kinematics and aerodynamic forces, several studies have used various techniques to document the power required for various insects to fly, showing that the specific power required to fly consistently ranges between 18 W/kg of body mass for fruit flies and 86 W/kg for bumblebees across many insect types [32,54–58].

Power can be estimated by summing the induced, inertial, and profile power contributions of the whole insect on a stoke-averaged basis, which is the approached used

in several studies [32,55,56]. Alternatively, the power required can be directly calculated knowing the wing's motion and the forces it generates [4,38,59,60].

The power required takes on both positive and negative values in the course of a single stroke. One reason for this is that the wing's inertia is a significant contributor to required power. In the periodic motion of a flapping flyer, acceleration and deceleration of the wing makes positive and negative contributions to required power respectively. Negative power is treated in one of two ways in the literature with various justifications. First, the broad consensus in the literature is to neglect negative power [4,32,54–58,61]. This treatment assumes that aerodynamic damping assists with the deceleration and that the metabolic cost of performing negative work is much less than an equivalent amount of positive work [55,62]. It also assumes that energy cannot be stored in the system in an attempt to make a conservative estimation of power [32,55,58]. We will term this calculation of power as the positive required power, $P_{pos} = \text{mean}\left(\forall P(t) > 0\right)$, where $P(t)$ is the time history of power, which is the average of all positive power in a single wing stroke. Using this definition of power predictions for hovering insects in the literature are per Table 2.1.

Secondly, negative power can be included directly in the average, which assumes that energy can be stored in the system and used to offset positive power during other portions of the stroke. Several researchers also report this calculation of power because they reason that insects likely can store some strain energy in their muscle or exoskeletal cuticle fibers [32,55,56].

Based on Table 2.1, the estimated power based on stroke-averaged induced, profile and inertial power typically under predicts the total power, but they are on the same order as the more rigorous calculations of power.

Table 2.1. Summary of normalized power reported in the literature.

Study	Insect	P_{pos}, W/kg_{insect}	Calculation method
Ellington 1984 [54]	Drone fly	47.5 ± 1.5	Estimated based on the sum of induced, profile and inertial power based on observed kinematics and morphology
Ellington 1984 [54]	Bumblebee	37.5 ± 1.5	
Dudley & Ellington 1990 [55]	Bumblebee	55 ± 12	
Lehman & Dickinson 1997 [57]	Fruit fly	18 ± 1.8	
Willmott & Ellington 1997 [56]	Hawkmoth	24.3 ± 3.3	
Fry et. al 2005 [32]	Fruit fly	34.5 ± 9	
Wu & Sun 2003 [63]	Fruit fly	29	Directly calculated by 3D NS, using abstracted kinematics
Sun & Du 2003 [59]	Bumblebee	56	
Liu 2009 [64]	Hawkmoth	27	
Engels et al. 2016	Bumblebee	84.0	Directly calculated by 3D NS, biomimetic kinematics

2.6. Flight Dynamics of Flapping Wings

The study of flight mechanics typically includes both the stability and control of flight, particularly for conventional aircraft and helicopters. Typically, stability is studied first since it is concerned with the response of the system (in equilibrium) to external perturbations. Once the stability characteristics are established, a variety of control strategies are then applied. Although some work has been performed in the realm of controlling flapping wing flyers [65–72] most of the published studies focus on open loop stability, which has been well-summarized by Sun [7], Orlowski and Girard [10], and Taha, Hajj, and Nayfeh [6].

Studying the stability of insects is itself a daunting task. Like helicopters, most insects can hover and achieve forward flight. The stability characteristics of these flight regimes are often distinct [73]. Although stability studies of insects in forward flight are present in the literature, the majority of the work has been on the stability in hover. The instabilities present in most flapping wing designs are worse in hover, where the potential damping effects of body drag are small without the presence of a freestream. Also, hover is assumed to be a pre-requisite to successful flapping wing flight.

The following review, therefore, focuses on stability of insects and flapping wing micro air vehicles in hover, and only select references to studies forward flight or control strategies are provided.

2.6.1. Flight Stability of Live Insects

Several researchers have conducted experiments on live insects. Taylor and Thomas [74] published the first study on insect flight dynamics, focusing on longitudinal stability of the desert locust. They approximated the stability derivatives of live desert locusts in wind tunnel tests with live insects. Their analysis suggests that the desert locust possesses a stable "short period" mode (similar to aircraft), a stable oscillatory mode, and an unstable non-oscillatory mode. All three modes contain contributions from all degrees of freedom, but they showed that the moment sensitivity to horizontal speed, also known as the speed derivative M_u, is a primary source of this instability. In spite of this inherent instability, the desert locust can correct for pitch disturbances within a single wing beat Ristroph et al. [72] concentrated on the stabilization of fruit flies, and concluded that the insect was instable in hover due to the growth rate of the body pitch. However, balanced flight can be achieved via either sufficiently fast control inputs or

artificially augmenting the body drag. Both of these observational studies also concluded that inputs are likely made no more than once per cycle and that pitch damping is the largest source of stability. Pitch damping exists when a pitch rate automatically generates a moment that counters the pitching motion.

Cheng, Deng, and Hedrick [75] focused on the control of a hawk moth in hover. They used estimates of the stability derivatives and a simple linear flight dynamics model assuming a quasi-steady aerodynamics to also conclude that the hawkmoth was inherently unstable. They also showed that flapping wing motion produces significant damping about the yaw axis, which they termed flapping counter torque. This damping causes the directional modes of most insects and birds to be stable [76]. This finding further motivates us to focus our analysis on the longitudinal dynamics in the pitch plane.

All of these studies, however, demonstrate the difficulty of determining the true open loop stability of insect-inspired flapping wing flyers by observing live insects because their flight is inherently controlled. Due to these difficulties in applying the observation of live insects to the analysis of FWMAVs, there have been several efforts at numerical and computational modeling that are reviewed in the next sections.

2.6.2. Flapping Wing Stability based on Navier-Stokes Solutions

There are two general approaches to modeling the flight dynamic equations of motion. Most early studies ignored wing mass and average the forces over a single flapping cycle, resulting in the standard aircraft equations of motion [6,7,77]. Later, simulations included the effects of wing mass [14,17] and the influence of the wing inertia on the overall body response was included. However, for those insects that flap at

high flapping frequencies, the inclusion of wing mass did not substantially change the resulting dynamic response of the insect or FWMAV [17,77].

There are two general ways of modeling the aerodynamics. We can directly solve the Navier Stokes equations to determine the velocity and pressure throughout the flow, and then calculating the resulting forces and moments, which we discuss first. Alternatively, we can use a quasi-steady model, which we review in the next sub-section.

The majority of the flapping flight dynamics studies based on NS aerodynamics have come from Sun and coworkers [15–18,39,40,78–85]. Their work has examined the hovering and forward flight dynamics of multiple insects of interest to the research community. Sun and Xiong's work [15] considered small perturbations about an assumed equilibrium in the longitudinal plane for hovering bumblebees. Although this first study omitted wing mass and did not couple the NS solutions to the flight dynamics, they were the first to identify the three natural modes of motion that have subsequently been seen by most other researchers. These modes are typically expressed by plotting the open loop poles of the system on the complex plane which are provided in Figure 2.1

The poles are simply the eigenvalues of the system matrix in equilibrium. The poles with negative real parts are stable, and the magnitude of the response decays in time. The poles with positive real parts are unstable, and the magnitude of the response grows. If the imaginary component of the pole is nonzero then the response oscillates. The pair of complex poles in the right half of the imaginary plane represents an unstable oscillatory mode which consists primarily of the horizontal and pitch degrees of freedom based on eigenvector analysis per the results of Sun and Xiong [15]. The large negative real pole represents a fast subsidence mode which is highly damped and consists

primarily of horizontal and pitch rates that are out of phase [15]. The smaller negative real pole is a lightly damped mode consisting primarily of the vertical and horizontal rates and represents the stable heave-dynamics of the insect. These modes are well-understood, although there exists some discussion about the relative contribution of the various aerodynamic forces as well as the applicability of direct averaging [77].

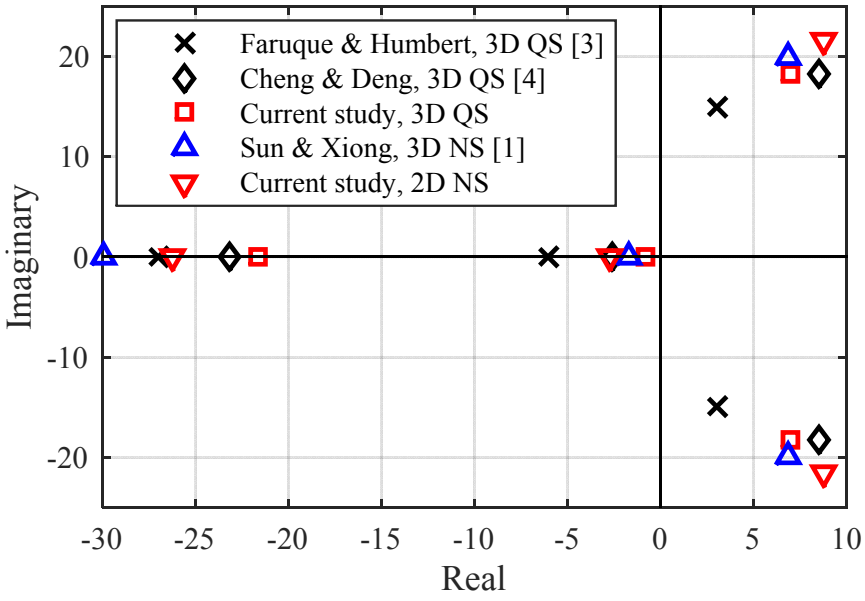

Figure 2.3. Open loop poles of insects and FWMAVs with rigid wings from the literature.

In a follow-on work, Sun and coworkers coupled the equations of motion to the flight dynamics and also include the inertial forces of the wing [17]. They also describe a numerical technique, "the shooting method," to determine the initial conditions for equilibrium [17]. Their previous work was trimmed by trial and error simply by balancing the forces (without considering body motion). Recognizing that even in hover, insects oscillate about an equilibrium point, Wu, Zhang, and Sun [17] demonstrated the

effects of those oscillations on the aerodynamic forces generated. They found that slightly higher angles of attack are required in the presence of such body motion, which translates into slightly higher power demands than previous analysis indicated.

Furthermore, Wu and Sun [81] utilized Floquet stability analysis to study the stability of insects about a periodic equilibrium, concluding that insects with larger wings develop body oscillations large enough to preclude the use of fixed-point stability and control techniques. This finding has significant implications in the field of developing FWMAVs with a proper wing-body mass ratio. Larger wing to body mass ratios appear to be more advantageous from the standpoint of offering the potential to glide and conserve energy as in butterfly flight [86]. However, larger wing mass introduces significantly more complicated flight path considerations and requires the adoption of nonlinear control methods [11].

Liang and Sun [18] have also demonstrated the ability to couple the full nonlinear equations of motion to a Navier-Stokes solver. They confirmed that insect flight in hover is inherently unstable, and that the pitching moment is the primary cause for the longitudinal instability. Gao et al. [34,64] performed flight dynamic analysis of all six degrees of freedom on a fruit fly and the NS solutions. However, they calculated their NS solutions offline, represented the forces by Fourier series, and coupled the results of this simulation to the flight dynamics. Although they did not calculate the system poles, they show via longitudinal simulations that the system eventually tends to diverge in the presence of a disturbance.

2.6.3. Flapping Wing Stability based on Quasi Steady Aerodynamics

Various quasi-steady models are used to model insect flight dynamics which all share a common shortcoming: they do not model wake effects and are therefore unable to model the influence of the wake on the dynamics. That said, because of their simplicity, these quasi steady models are widely used in studying flapping wing flight dynamics.

Faruque and Humbert [9,41] were the first to model the longitudinal and lateral stability of fruit flies around hover using a simple quasi-steady aerodynamic model, which considered only the translational lift prediction from Sane and Dickinson [27]. They analyzed the stability via frequency based system identification and concluded that the fruit fly possesses the same three natural modes in the longitudinal plane as Sun and Xiong [15].

Orlowski and Girard [11] used a quasi-steady model by Berman and Wang [4], and considered the mass of the wings in the equations of motion. They found that treating the mass of the wings as inconsequential could lead to erroneous results. They also demonstrated that full-cycle averaging of the aerodynamic forces can overly simplify the analysis. They observed that quarter-cycle averaging can produce much more reliable results, with only a small computational cost [14].

In a similar vein, Taha et al. [5,77] have produced several studies that analyze the averaging techniques that are commonly used FWMAV flight dynamics studies. In short, they show that direct averaging of the states and forces of relatively low frequency flappers (e.g. a hawkmoth) can lead to the potentially false conclusion that such a system is unstable at a fixed point, whereas Floquet theory and their high order averaging technique demonstrates that the system is stable, agreeing with their simulation of the

nonlinear flight dynamics [77]. They investigate other insects as well, and conclude that as the ratio of flapping frequency to body natural frequency ratio exceeds 100, direct averaging techniques are able to predict if a system will be stable at its fixed points. However, for a fruit fly, they show that direct averaging yields eigenvalues for the unstable mode that are 15% more than their higher order method predicts.

In another work, Taha et al. [5] demonstrate the stability implications of physical parameters such as the location of the wing root with respect to the body center-of-gravity (CG), and they show how changing flapping frequency and/or mean angle of attack affect each of the stability derivatives in different ways. These studies highlighted the sensitivity of the analysis to both physical and simulation parameters.

As such, we carefully construct our model using the wealth of data on the fruit fly in the literature. Additionally, we omit any averaging of the periodic forcing, and couple the aerodynamic, flight dynamics, and when applicable, structural dynamics at each time step. Enforcing this level of consistency is essential to ensuring that other factors do not veil the effect of wing flexibility on the stability of the system.

2.6.4. Summary of Flapping Wing Flight Dynamics

Most early studies made several large simplifying assumptions: they neglected wing mass, did not fully couple the flight dynamics and aerodynamics, or if they were coupled, the forces and moments were cycle-averaged and applied to the insect only once per cycle. Most computational studies since 2009 have included wing mass and coupled the equations of motion to the flight dynamics in both quasi-steady and Navier Stokes models. In the current study, the equations of motion are fully coupled to the

aerodynamics (both QS and NS models), and wing mass and inertial effects are included in all the simulations herein. Additionally, we include wing flexibility when desired.

Stability is determined in one of three methods: either via longitudinal response, via Floquet Stability, or via the stability of the linearized system matrix. The overwhelming majority of studies publish the stability of the system in terms of the open loop poles. However, there are several studies which simply present the long term system response over time Orlowski [11] Liang & Sun [18] Gao et al. [34], Wu Zhang and Sun [17]. We utilize both of these methods in the course of the current study. Presenting the system poles assumes that equilibrium has been achieved. Many studies use trial and error to adjust control inputs [15,16] to achieve lift balance. Other assumed that the horizontal and moment forces cycle-average to zero, and they only attempt to determine the stroke amplitude or pitch angles required for lift-weight balance [5,77]. Furthermore, there is only a single study [17] that describes a method to determine the equilibrium of a full-coupled system, but this method is only suitable for finding the initial conditions, and they do not directly address how the necessary control inputs are determined. In this dissertation, a more comprehensive method of finding both the control inputs and initial conditions is presented for all three aerodynamic models that are included.

In spite of the many studies in the area of flight dynamics, none of the literature has reported on the influence of wing flexibility on the open loop stability of the vehicle. This is highlighted in each of the three main review papers in the field:

- "As far as the present author knows, there is no formal quantitative study or even qualitative discussion about the effect of wing deformation on flight dynamics stability." [7]

- "There is a need for a rigorous aeroelastic-flight dynamic model. This model has to include a moderate fidelity unsteady aerodynamic representation, which can be run every time step to determine the instantaneous aerodynamic loads, which are in turn fed to a complete dynamic model without the ubiquitous assumptions of averaging the dynamics and neglecting the wing inertia forces." [6]

- "One major deficiency of the literature to date is that the wings are considered to be rigid wings and smooth without accounting for the intrinsic structural flexibility… Furthermore, intrinsic interactions between flexible wing structures, flight stability and associated aerodynamics are open issues awaiting further investigation." [87]

In this work, we specifically meet the requirement of Taha et al. [6]. First, the wing mass is included in the calculation of both power and the dynamics. Secondly, the flexible wing model allows for a fully coupled solution to the three-way balance between wing inertia, the elastic restoring force, and the fluid dynamic force to be determined at each time step. Finally, the flight dynamics are fully coupled to the fluid-structure interaction so that no averaging is necessary or performed—the simulation is in free flight and we do not simply balance the average forces on a static model.

CHAPTER 3

METHODOLOGY

Modeling the free flight performance of a bioinspired FWMAV requires accurately representing achievable wing kinematics, the flight dynamics, structural dynamics of the flexible wing, and aerodynamic forces and the power required to achieve flight. The present study considers the flight performance of a flapping wing flyer at the fruit fly scale at hover with an abstracted, bio-inspired wing motion using both rigid and flexible wings. Only the longitudinal modes of stability are considered since these modes have been shown to be unstable for most insects [7,77]. The wing mass, often neglected in prior studies in insect flight, is considered in both the dynamic equations of motion (EOMs) and in the calculation of wing power. The equations of motion are tightly coupled to the aerodynamic model such that the motion of the body is adjusted by the aerodynamic forcing at every time step of the simulation for both quasi steady (QS) and Navier Stokes (NS) models and aerodynamic forces and moments are affected by the motion of the flyer.

This chapter details the mathematical and computational models developed in order to analyze the flight performance and stability of a flapping wing micro air vehicle in hover. The chapter is organized as follows. The reference frames, coordinate vectors, kinematics and dynamics of flight are presented first. The wing kinematics and relevant

aerodynamic models are then described. Finally, the method of determining equilibrium and the stability about that equilibrium is shown last.

3.1. Flight Dynamics

3.1.1. Reference Frames and Key Locations

Although our analysis only considers longitudinal motion, we develop the full equations of motion for all six degrees of freedom of body motion in this section. Most studies utilize three main reference frames for the study of flapping wing flight dynamics [6]: the inertial frame, the body frame and the wing frame. The inertial frame is attached to the surface of the earth with *x*-*y*-*z* associated with north-east-down orientations. The body frame is located at the FWMAV center of gravity (CG) and is arrived at via 3-2-1 Euler Rotations from the inertial reference frame with the x_b axis aligned longitudinally in the manner defined in Ellington [88], y_b extends laterally to the right, and the z_b axis points down per Figure 3.1(a). The rotations between inertial and body frames are very common in the analysis of airplanes and helicopters and, therefore, we refer to Etkin [89] for the details.

Motivated by the control inputs used in Faruque and Humbert [9] as well as Liu et al. [90], we also assess the effect of orienting the stroke plane angle, which differs from body frame by angle β around y_b and y_{sp}. The subscripts *b* and *sp* refer to the body and stroke plane, respectively. The wing frame for the right wing (subscript *w*) differs from the stroke plane by the following sequence of rotations, depicted in Figure 3.1(b). The basis vectors are reoriented such that x_{usp} aligns with y_{sp} and y_{usp} aligns with $-z_{sp}$ where the subscript "*usp*" stands for upright stroke plane. This transformation allows the wing

angles to be readily compared to those of other researchers, particularly Sun and coworkers [15,17]. The flap angle ζ rotates about y_{usp}. The vertical deviation angle is not considered in this study, and the pitch angle α rotates about x_w. A more detailed presentation of the references frames used in this study is available in the Appendix.

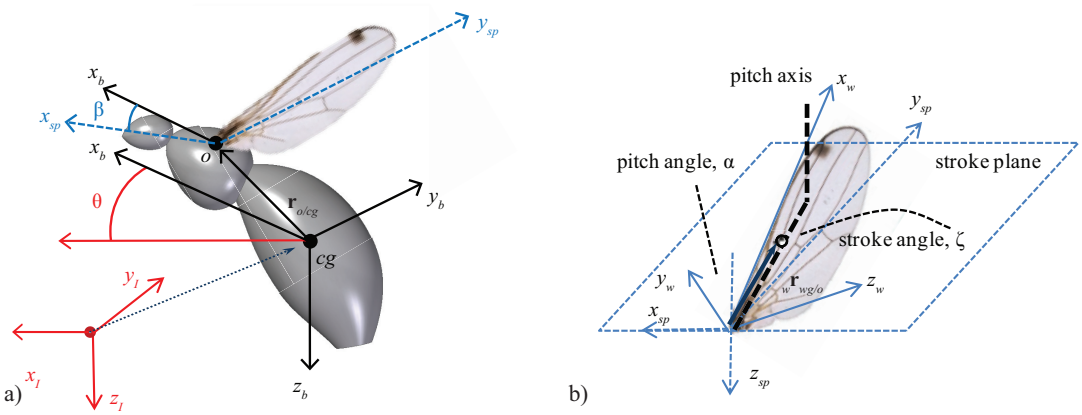

Figure 3.1. (a) Inertial, body, and stroke plane reference frames; (b) Stroke plane with Euler angles.

Several reference vectors are required to define the location of key coordinates. The location of the wing root with respect to the body CG is described by ${}_b\mathbf{r}_{o/cg}$ (see Figure 3.1(a)), which is expressed in the body frame. The wing root is denoted with a subscript *o*, and the subscript *cg* is for the body CG. If a vector has a left subscript, it indicates the reference frame in which it is defined, and in this case, the vector from the wing root to the body CG is defined in the body reference frame. Additionally, the location of the wing center of gravity is described by ${}_w\mathbf{r}_{wg/o}$ in the wing reference frame, where we use the subscript *wg* for the wing center of gravity. We assume the wing CG is

located at 35% span from the wing root and 25% chord from the leading edge in accordance with values reported by Ennos [45]. Additionally, in the study of rigid wings, the wing pitch axis is allowed to vary and the *x*-axis of the wing is always co-located with the pitch axis of the wing. Cases that consider wing flexibility utilize an imposed plunge motion at the leading-edge, so the *x*-axis of the wing is attached to the leading edge for flexible wings.

The Reynolds number for this study is $Re = Uc/\nu$, where c is the mean chord and ν is the kinematic viscosity of air (1.71×10^{-5} m^2/s). The maximum velocity of the wing's aerodynamic center is $U = 2\pi f r_2 Z$ where f is the flapping frequency, r_2 is the distance to center of the second moment of wing area, and Z is the flapping amplitude. For the current study, the Reynolds number is set to 1×10^2 for all cases. We nondimensionalize forces and moments by the standard convention of $C_L=L/(0.5\rho U^2 S)$ and $C_M=M/(0.5\rho U^2 Sc)$ where ρ is the density of air (1.23 kg/m^3) and S is the planform area of a single wing, $S = Rc$. Other parameters of interest are listed in Table 3.1, where the nondimensional distances in the spanwise and chordwise directions are normalized with the span R and the chord c, respectively (e.g. $\hat{r}_2 = r_2 / R$).

3.1.2. Body and Wing Kinematics

We assume that the body is rigid. The motion of a rigid body is described by tracking the position, velocity and acceleration of the body's center of gravity. It is convenient to track the body's motion in the body-fixed coordinate system, so the kinematics must account for the rotation of the body as well. Subscripts to the left of a vector quantity identify the reference frame in which the vector is expressed. In case

where it is not necessary to specify a reference frame for a vector equation, these are omitted. The velocity and acceleration of the body CG is given as

$$ {}_b\mathbf{v}_{cg} = \begin{bmatrix} u & v & w \end{bmatrix}^T \tag{3.1} $$

$$ {}_b\mathbf{a}_{cg} = \frac{d}{dt}\left(R_{b\to I}\, {}_b\mathbf{v}_{cg} \right) = {}_b\dot{\mathbf{v}}_{cg} + {}_b\boldsymbol{\omega}_{b/I} \times {}_b\mathbf{v}_{cg} \tag{3.2} $$

where the angular velocity of the body is ${}_b\boldsymbol{\omega}_{b/I} = [p\ q\ r]^T$ and $R_{b\to I}$ represents the matrix of direction cosines between the body and the inertial references frames (details are provided in the Appendix). The body rotation rates about x_b, y_b, and z_b are p, q, and r respectively.

Table 3.1. Morphological parameters for a fruit fly from [8,76].

symbol	description	value	unit	symbol	description	value	unit
m_b	mass of body	0.96	mg	m_w	mass of wing	3.26×10^{-3}	mg
L_b	body length	2.5	mm	c	mean chord	0.8	mm
f	stroke frequency	218	Hz	R	wing length	2.39	mm
L_1/L_b	distance between CG & wing root	20.4%		$I_{yy,b}$	body moment of inertia (pitch)	5.1×10^{-9}	kgm^2
$\hat{r}_2(S)$	% span to 2nd moment of area	55%		$I_{xx,w0}$		1.6×10^{-16}	kgm^2
$\hat{r}_1(m)$	% span to wing center of mass	35%		$I_{yy,w0}$	moment of inertia about wing root	3.6×10^{-15}	kgm^2
$\hat{c}_1(m)$	% chord to wing center of mass	25%		$I_{zz,w0}$		3.8×10^{-15}	kgm^2
				$I_{xy,w0}$	product of inertia about wing root	5.2×10^{-17}	kgm^2

The kinematics of the wing involve three points of interest: the wing root, the wing center of gravity, and the aerodynamic center (defined in Section 3.3.1), which is denoted with subscript *ac*. Referring to Figure 3.1(b), we can express the velocity vector of a point *p* on the wing as follows (where *p* can be substituted for the wing CG, or the wing aerodynamic center as needed).

$$\mathbf{v}_p = \mathbf{v}_o + \mathbf{v}_{p/o} + \boldsymbol{\omega}_w \times \mathbf{r}_{p/o} \tag{3.3}$$

$${}_w\mathbf{v}_p = R_{b\to w}\left({}_b\mathbf{v}_{cg} + {}_b\boldsymbol{\omega}_b \times {}_b\mathbf{r}_{o/cg}\right) + {}_w\mathbf{v}_{p/o} + {}_w\boldsymbol{\omega}_w \times {}_w\mathbf{r}_{p/o} \tag{3.4}$$

Equation (3.4) represents the velocity in the wing frame, which we use for determining aerodynamic forces. The ${}_w\mathbf{v}_{p/o}$ term is non-zero only in the case of wing deformation. The angular velocities in equations (3.3) and (3.4) are with respect to the inertial frame, unless the subscript indicates otherwise. For example, the angular velocity of the wing $\boldsymbol{\omega}_w$ represents the rotation rates of the wing reference frame with respect to the inertial reference frame. If we need to describe the wing rotation rates with respect to the body rotation rates, we use $\boldsymbol{\omega}_{w/b}$. Therefore wing's angular velocity $\boldsymbol{\omega}_w$ in equation (3.4) includes both the body rotation rates and the rotation of the wing with respect to the body. It is defined in equation (3.5) where $R_{b\to w}$ is the transformation matrix from the body to the wing (see the Appendix for details), and "s" and "c" denote the sine and cosine of the subscripted angle. The underlined matrix is the rate transformation matrix $R_{\omega\to w}$ that expresses the wing rotation rates in the wing frame.

$$ {}_w\boldsymbol{\omega}_w = R_{b\to w}\,{}_b\boldsymbol{\omega}_b + \begin{bmatrix} 1 & \mathrm{s}_\delta & 0 \\ 0 & \mathrm{c}_\delta\,\mathrm{c}_\alpha & \mathrm{s}_\alpha \\ 0 & -\mathrm{c}_\delta\,\mathrm{s}_\alpha & \mathrm{c}_\alpha \end{bmatrix} \begin{bmatrix} \dot{\alpha} \\ \dot{\zeta} \\ \dot{\delta} \end{bmatrix} \tag{3.5} $$

The acceleration of a point on the wing is obtained by taking the time derivative of the velocity with respect to the inertial reference frame, and applying the kinematic transport theorem for rotating reference frames as necessary. The final result appears in equation (3.6).

$$ \begin{aligned} {}_w\mathbf{a}_p = {} & R_{b\to w}\left({}_b\mathbf{a}_{cg} + {}_b\boldsymbol{\omega}_b \times {}_b\mathbf{v}_{cg} + {}_b\dot{\boldsymbol{\omega}}_b \times {}_b\mathbf{r}_{o/cg} + {}_b\boldsymbol{\omega}_b \times {}_b\boldsymbol{\omega}_b \times {}_b\mathbf{r}_{o/cg} \right) \\ & + {}_w\mathbf{a}_{p/o} + 2\,{}_w\boldsymbol{\omega}_w \times {}_w\mathbf{v}_{p/o} + {}_w\dot{\boldsymbol{\omega}}_w \times {}_w\mathbf{r}_{p/o} + {}_w\boldsymbol{\omega}_w \times {}_w\boldsymbol{\omega}_w \times {}_w\mathbf{r}_{p/o} \end{aligned} \tag{3.6} $$

The velocity and acceleration of point p with respect to the wing root, ${}_w\mathbf{v}_{p/o}$ and ${}_w\mathbf{a}_{p/o}$ arise only in the case of wing deformation. These terms can be calculated by determining the rotational acceleration and rate of the wing and applying it to equations (3.7) and (3.8) where $\dot{\alpha}$ and $\ddot{\alpha}$ are the passive pitch rate and acceleration due to deformation.

$$ {}_w\mathbf{v}_{p/o} = \dot{\alpha}\mathbf{i}_w \times {}_w\mathbf{r}_{wg/o} \tag{3.7} $$

$$ {}_w\mathbf{a}_{p/o} = \ddot{\alpha}\mathbf{i}_w \times {}_w\mathbf{r}_{wg/o} + \dot{\alpha}\mathbf{i}_w \times \dot{\alpha}\mathbf{i}_w \times {}_w\mathbf{r}_{wg/o} \tag{3.8} $$

Furthermore, the rotational acceleration of the wing is expressed as

$$ {}_w\dot{\boldsymbol{\omega}}_w = R_{b\to w}\begin{bmatrix} p \\ q \\ r \end{bmatrix} \times R_{\omega\to w}\begin{bmatrix} \dot{\alpha} \\ \dot{\zeta} \\ \dot{\delta} \end{bmatrix} + R_{b\to w}\begin{bmatrix} \dot{p} \\ \dot{q} \\ \underline{\dot{r}} \end{bmatrix} + \dot{R}_{\omega\to w}\begin{bmatrix} \dot{\alpha} \\ \dot{\zeta} \\ \dot{\delta} \end{bmatrix} + R_{\omega\to w}\begin{bmatrix} \ddot{\alpha} \\ \ddot{\zeta} \\ \ddot{\delta} \end{bmatrix} \tag{3.9} $$

The derivative of the wing rate transformation matrix $\dot{R}_{\omega\to w}$ is given in the Appendix. Fully expressing the wing's acceleration in this manner allows the higher derivative terms of the body (which are underlined in equation (3.9)) to be isolated, which is necessary in order to solve the equations of motion.

3.1.3. Wing Forces and Moments

The aerodynamic force and the gravitational force act on the wing, which depicted in Figure 3.2. Additionally, there is a reaction force and moment at the wing root. The force sum can be expressed as

$$ \sum \mathbf{F}_{wing} = \mathbf{F}_{Aero} + \mathbf{F}_{grav} + \mathbf{F}_{R_{BonW}} \tag{3.10} $$

The aerodynamic force calculations are described in Section 3.3. Their integrated effect is a resultant aerodynamic force that acts at the center of pressure of the wing. Rather than track the center of pressure, however, we calculate the moment about the pitch axis of the wing for convenience. From Newton's Third Law, the force of the body on the wing ${}_w\mathbf{F}_{R_{BonW}}$ is equal and opposite to the force of the wing on the body ${}_w\mathbf{F}_{R_{WonB}}$. Thus, the net force of the wing on the body is equal to the aerodynamic and gravitational forces minus the inertia that arises from the wing's motion per equation (3.11).

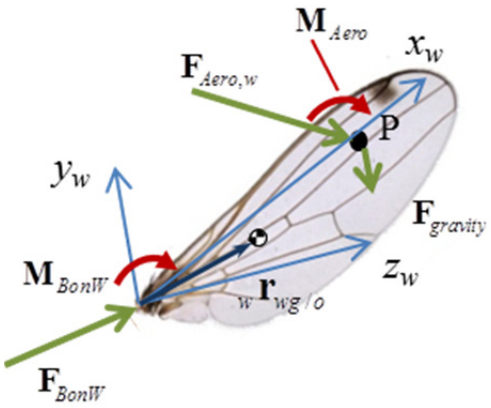

Figure 3.2. Forces, moments and geometric parameters for the fruit fly wing.

$$
\begin{aligned}
&{}_w\mathbf{F}_{R_{WonB}} = {}_w\mathbf{F}_{Aero} + m\,{}_w\mathbf{g} \\
&-m_w\left({}_w\mathbf{a}_{wg/o} + 2\,{}_w\boldsymbol{\omega}_w \times {}_w\mathbf{v}_{wg/o} + {}_w\dot{\boldsymbol{\omega}}_w \times {}_w\mathbf{r}_{wg/o}\,{}_w + {}_w\boldsymbol{\omega}_w \times {}_w\boldsymbol{\omega}_w \times {}_w\mathbf{r}_{wg/o}\right) \\
&-m_w R_{b\to w}\left({}_b\mathbf{a}_{cg} + {}_b\boldsymbol{\omega}_b \times {}_b\mathbf{v}_{cg} + {}_b\dot{\boldsymbol{\omega}}_b \times {}_b\mathbf{r}_{o/cg} + {}_b\boldsymbol{\omega}_b \times {}_b\boldsymbol{\omega}_b \times {}_b\mathbf{r}_{o/cg}\right)
\end{aligned}
\tag{3.11}
$$

Equation (3.12) details the various external moments that combine to change the angular momentum of the wing, where ${}_w\mathbf{W}_w$ is the weight of the wing expressed in the wing frame.

$$
\sum {}_w\mathbf{M}_o = {}_w\mathbf{M}_{Aero} + {}_w\mathbf{M}_{R_{BonW}} + {}_w\mathbf{r}_{wg/o} \times {}_w\mathbf{W}_w + {}_w\mathbf{r}_{ac/o} \times {}_w\mathbf{F}_{Aero} \tag{3.12}
$$

Therefore, the moment of the wing on the body is given in equation (3.13). It consists of the aerodynamic and gravitational moment minus the changes in angular momentum of the wing, where the inertia is determined about the wing root, ${}_wI_{wo}$ (vice the inertia about the wing CG).

$$
\begin{aligned}
{}_w\mathbf{M}_{R_{WonB}} &= {}_w\mathbf{M}_{Aero,w} + {}_w\mathbf{r}_{ac/o} \times {}_w\mathbf{F}_{Aero,w} + {}_w\mathbf{r}_{wg/o} \times m_w\, {}_w\mathbf{g} \\
&- \left({}_w\underline{I}_{wo}\, {}_w\dot{\boldsymbol{\omega}}_w + {}_w\boldsymbol{\omega}_w \times {}_w\underline{I}_{wo}\, {}_w\boldsymbol{\omega}_w + {}_w\mathbf{r}_{wg/o} \times m_w\, {}_w\mathbf{a}_o \right)
\end{aligned} \tag{3.13}
$$

3.1.4. Body Force and Moments

The weight of the body acts through the body CG, and since the moments are taken about the CG, the weight of the body does not contribute to the moment. Since the motion of the body in hover is considered slow relative to the velocities developed on the wing, we neglect the aerodynamic forces and moments developed on the body. The equations of motion are obtained by substituting the appropriate terms that have been derived above into equations (3.14) and (3.15).

$$
\sum \mathbf{F}_{body} = \mathbf{F}_{grav} + \mathbf{F}_{R_{WonB}} = m_b\, {}_b\mathbf{a}_{cg} \tag{3.14}
$$

$$
\sum {}_b\mathbf{M}_{cg} = {}_b\mathbf{M}_{R_{WonB}} + {}_w\mathbf{r}_{o/cg} \times {}_b\mathbf{F}_{Aero,w} = {}_bI_{b,cg}\, {}_b\dot{\boldsymbol{\omega}}_b + {}_b\boldsymbol{\omega}_b \times {}_bI_{b,cg}\, {}_b\boldsymbol{\omega}_b \tag{3.15}
$$

The expression for the linear force-acceleration balance is given in equation (3.16).

$$
{}_b\mathbf{F}_{Aero,body} + m_{body}\, {}_b\mathbf{g} + \sum_{i=1}^{\#wings} \left[R_{w,i\to b} \right] \left({}_w\mathbf{F}_{Aero,w,i} + m_{w,i}\, {}_w\mathbf{g} \right) = \tag{3.16a}
$$

$$
\left(m_{body} + \sum_{i=1}^{\#wings} m_{w,i} \right) \left({}_b\mathbf{a}_{cg} + {}_b\boldsymbol{\omega}_b \times {}_b\mathbf{v}_{cg} \right) + \tag{3.16b}
$$

$$
\sum_{i=1}^{\#wings} m_{w,i} \left({}_b\dot{\boldsymbol{\omega}}_b \times {}_b\mathbf{r}_{o/cg} + {}_b\boldsymbol{\omega}_b \times {}_b\boldsymbol{\omega}_b \times {}_b\mathbf{r}_{o/cg} \right) + \tag{3.16c}
$$

$$
\sum_{i=1}^{\#wings} m_{w,i} \left[R_{w,i\to b} \right] \left({}_w\mathbf{a}_{wg/o} + {}_w\dot{\boldsymbol{\omega}}_w \times {}_w\vec{r}_{wg/o} + {}_w\boldsymbol{\omega}_w \times {}_w\boldsymbol{\omega}_w \times {}_w\mathbf{r}_{wg/o} + 2\, {}_w\boldsymbol{\omega}_w \times {}_w\mathbf{v}_{wg/o} \right) \tag{3.16d}
$$

The physical significance of each term is as follows:

a. The aerodynamic force exerted on the body, the gravitational force exerted on the body, and the sum of the aerodynamic forces and gravitational forces on each wing.

b. The acceleration of the central body in the body frame.

c. The inertial contribution of the wings arising from the motion of the body (tangential and centripetal acceleration).

d. The inertial contributions of the wing arising from the wing motion and deformation. The wing deformation is accounted for by the acceleration of the wing's CG with respect to the wing root (when expressed in the wing reference frame, these components are nonzero only if the wing deforms such that its CG moves inside the wing reference frame), and the Coriolis term.

Additionally, the rotational force-acceleration balance is detailed in equation (3.17), with each term's significance detailed below. In short, this equation states that the sum of the external moments on the body due to aerodynamic and gravitational forces minus the rotational inertia of the wings causes changes of the angular momentum of the body. The rotational inertia of the wings results from both the flapping motion of the wings and the general motion and rotation of the FWMAV. Each term can be described as follows:

a. The aerodynamic moments about the fuselage CG arising from aerodynamic forces and couples on the fuselage.

b. The aerodynamic moment about the pitch axis produced by the motion of the wings and the moment on the wing root due to the weight of the wings.

$$ {}_b\mathbf{M}_{Aero,body} + {}_b\mathbf{r}_{ac,b/cg} \times {}_b\mathbf{F}_{Aero,body} \tag{3.17a} $$

$$ + \sum_{i=1}^{\#wings} \left[\underset{w,i\to b}{R} \right] \left({}_w\mathbf{M}_{Aero,w} + {}_w\mathbf{r}_{ac/o} \times {}_w\mathbf{F}_{Aero,w} + {}_w\mathbf{r}_{wg/o} \times m_{w\ w}\mathbf{g} \right)_i \tag{3.17b} $$

$$ + \sum_{i=1}^{\#wings} {}_b\mathbf{r}_{o/cg,i} \times \left[\underset{w,i\to b}{R} \right] \left({}_b\mathbf{F}_{Aero,wing} + m_{w\ w}\mathbf{g} \right)_i \tag{3.17c} $$

$$ - \sum_{i=1}^{\#wings} \left[\underset{w,i\to b}{R} \right] \left({}_wI_{w,o\ w}\dot{\boldsymbol{\omega}}_w + {}_w\boldsymbol{\omega}_w \times {}_wI_{w,o\ w}\boldsymbol{\omega}_w + {}_w\mathbf{r}_{wg/o} \times m_{w\ w}\mathbf{a}_o \right)_i \tag{3.17d} $$

$$ - \sum_{i=1}^{\#wings} m_{w,i\ b}\mathbf{r}_{o/cg,i} \times \left[\underset{w,i\to b}{R} \right] \left(\begin{array}{c} {}_w\dot{\boldsymbol{\omega}}_w \times {}_w\mathbf{r}_{wg/o} + {}_w\boldsymbol{\omega}_w \times {}_w\boldsymbol{\omega}_w \times {}_w\mathbf{r}_{wg/o} \\ + \underline{{}_w\mathbf{a}_{wg/o} + 2\,{}_w\boldsymbol{\omega}_w \times {}_w\mathbf{v}_{wg/o}} \end{array} \right)_i \tag{3.17e} $$

$$ - \sum_{i=1}^{\#wings} m_{w,i\ b}\mathbf{r}_{o/cg,i} \times \left({}_b\mathbf{a}_{cg/I} + {}_b\dot{\boldsymbol{\omega}}_b \times {}_b\mathbf{r}_{o/cg} + {}_b\boldsymbol{\omega}_b \times {}_b\mathbf{v}_{cg} + {}_b\boldsymbol{\omega}_b \times {}_b\boldsymbol{\omega}_b \times {}_b\mathbf{r}_{o/cg} \right)_i \tag{3.17f} $$

$$ = {}_bI_{b,cg\ b}\dot{\boldsymbol{\omega}}_b + {}_b\boldsymbol{\omega}_b \times {}_bI_{b,cg\ b}\boldsymbol{\omega}_b \tag{3.17g} $$

c. The moment about the body CG arising from applying aerodynamic and weight forces at the wing root, multiplied by its offset from the fuselage CG.

d. The term that describes the change in the rotational inertia of the wings with respect to the wing root as a result of wing flapping and body motion. The last term in this expression arises because of our desire to express the wing inertia about the wing root.

e. The inertial forces of the wing are also transmitted to the wing root. If there is an offset between the wing root and the CG of the fuselage, it produces an additional moment. The portions of this equation that are underlined are nonzero only if the wing CG is able to move relative to the wing root in the wing reference frame. This is only possible if the wing is free to deform, and these terms capture the effect of deformation on the inertia.

f. The inertial forces of the wings that arise from the motion of the body. If there is an offset between the wing root and the CG of the body, it produces an additional moment.

g. The time rate of change of angular momentum of the body.

3.1.5. Solving the Equations of Motion

The flight dynamic equations of motion of the body are nonlinear equations. All of the highest derivative terms, however, are linear. In equations (3.18) and (3.19), we have rearranged the full equations of motion such that only the highest derivatives are on the left hand sides.

$$\begin{aligned}
&\left(m_{body} + \sum_{i=1}^{\#wings} m_{w,i} \right) {}_b\dot{\mathbf{v}}_b - \sum_{i=1}^{\#wings} m_{w,i}\, {}_b\left(\tilde{\mathbf{r}}_{o/cg} \dot{\boldsymbol{\omega}}_b \right) - \sum_{i=1}^{\#wings} m_{w,i} \left(R_{w\to b}\, {}_w\tilde{\mathbf{r}}_{wg/o} R_{w\to b}^T \right) {}_b\dot{\boldsymbol{\omega}}_b \\
&= {}_b\mathbf{F}_{Aero,body} + m_{body}\, {}_b\mathbf{g} + \sum_{i=1}^{\#wings} \left({}_b\mathbf{F}_{Aero,w,i} + m_{w,i}\, {}_b\mathbf{g} \right) - m_{body}\, {}_b\tilde{\boldsymbol{\omega}}_{b\,b}\mathbf{v}_b \\
&\quad - \sum_{i=1}^{\#wings} m_{w,i} \left({}_b\tilde{\boldsymbol{\omega}}_{b\,b}\mathbf{v}_b + {}_b\tilde{\boldsymbol{\omega}}_{b\,b}\tilde{\boldsymbol{\omega}}_{b\,b}\mathbf{r}_{o/cg} \right) \\
&\quad - \sum_{i=1}^{\#wings} m_{w,i} R_{w\to b} \left({}_w\dot{\mathbf{v}}_{wg/o} + 2\, {}_w\tilde{\boldsymbol{\omega}}_{w\,w}\mathbf{v}_{wg/o} - {}_w\tilde{\mathbf{r}}_{wg/o} \left(\dot{\boldsymbol{\omega}}_w - \dot{\boldsymbol{\omega}}_b \right) + {}_w\tilde{\boldsymbol{\omega}}_{w\,w}\tilde{\boldsymbol{\omega}}_{w\,w}\mathbf{r}_{wg/o} \right)
\end{aligned} \tag{3.18}$$

The coupling of the highest derivative terms is through the mass and inertial terms. Using the matrix form of the cross product which we denote with the tilde over a vector (e.g. ${}_w\tilde{\boldsymbol{\omega}}_{w\,w}\tilde{\boldsymbol{\omega}}_{w\,w}\mathbf{r}_{wg/o}$), we combine these terms into an equivalent mass matrix, H which is positive definite. See the Appendix for the full details of the mass matrix.

$$
\begin{aligned}
&{}_bI_{b,cg}\,{}_b\dot{\boldsymbol{\omega}}_b + \sum_{i=1}^{\#wings} \underset{w,i\to b}{R}\left({}_wI_{w,o}\,\underset{b\to w,i}{R}\,{}_b\dot{\boldsymbol{\omega}}_b\right)_i + \sum_{i=1}^{\#wings}\left(\underset{w,i\to b}{R}\,{}_w\tilde{\mathbf{r}}_{wg/o}m_w\left({}_b\dot{\tilde{v}}_{cg} - \tilde{\mathbf{r}}_{o/cg}\,{}_b\dot{\boldsymbol{\omega}}_b\right)\right)_i \\
&\quad - \sum_{i=1}^{\#wings} m_{w,i}\,{}_b\tilde{\mathbf{r}}_{o/cg,i}\left(\underset{w,i\to b}{R}\,{}_w\tilde{\mathbf{r}}_{wg/o}\,\underset{b\to w,i}{R}\,{}_b\dot{\boldsymbol{\omega}}_b\right) + \sum_{i=1}^{\#wings} m_{w,i}\,{}_b\tilde{\mathbf{r}}_{o/cg,i}\left({}_b\dot{\mathbf{v}}_{cg/I} + {}_b\dot{\tilde{\boldsymbol{\omega}}}_b\,{}_b\mathbf{r}_{o/cg}\right)_i \\
&= \mathbf{M}_{Aero,body} + {}_b\tilde{\mathbf{r}}_{ac,b/cg}\,{}_b\mathbf{F}_{Aero,body} + \sum_{i=1}^{\#wings}\underset{w,i\to b}{R}\left({}_w\mathbf{M}_{Aero,w} + {}_w\tilde{\mathbf{r}}_{ac/o}\,{}_w\mathbf{F}_{Aero,w} + m_w\,{}_w\tilde{\mathbf{r}}_{wg/o}\,{}_w\mathbf{g}\right)_i \\
&\quad + \sum_{i=1}^{\#wings} {}_b\tilde{\mathbf{r}}_{o/cg,i}\,\underset{w,i\to b}{R}\left({}_w\mathbf{F}_{Aero,wing} + m_w\,{}_w\mathbf{g}\right)_i - {}_b\tilde{\boldsymbol{\omega}}_b\,{}_bI_{b,cg}\,{}_b\boldsymbol{\omega}_b \\
&\quad - \sum_{i=1}^{\#wings}\underset{w,i\to b}{R}\left({}_wI_{w,o}\,{}_w\left(\dot{\boldsymbol{\omega}}_w - \dot{\boldsymbol{\omega}}_b\right) + {}_w\tilde{\boldsymbol{\omega}}_w\,{}_wI_{wg}\,{}_w\boldsymbol{\omega}_w\right) \\
&\quad - \sum_{i=1}^{\#wings}\left(\underset{w,i\to b}{R}\,{}_w\tilde{\mathbf{r}}_{wg/o}m_w\left[{}_b\tilde{\boldsymbol{\omega}}_b\,{}_b\mathbf{v}_{cg} + {}_b\tilde{\boldsymbol{\omega}}_b\,{}_b\tilde{\boldsymbol{\omega}}_b\,{}_b\mathbf{r}_{o/cg}\right]\right) \\
&\quad - \sum_{i=1}^{\#wings} m_{w,i}\,{}_b\tilde{\mathbf{r}}_{o/cg,i}\,\underset{w,i\to b}{R}\left[\begin{array}{c} -{}_w\tilde{\mathbf{r}}_{wg/o}\,{}_w\left(\dot{\boldsymbol{\omega}}_w - \dot{\boldsymbol{\omega}}_b\right) + {}_w\tilde{\boldsymbol{\omega}}_w\,{}_w\tilde{\boldsymbol{\omega}}_w\,{}_w\mathbf{r}_{wg/o} \\ + {}_w\dot{\mathbf{v}}_{wg/o} + 2\,{}_w\tilde{\boldsymbol{\omega}}_w\,{}_w\mathbf{v}_{wg/o}\end{array}\right]_i \\
&\quad - \sum_{i=1}^{\#wings} m_{w,i}\,{}_b\tilde{\mathbf{r}}_{o/cg,i}\left({}_b\tilde{\boldsymbol{\omega}}_b\,{}_b\mathbf{v}_{cg} + {}_b\tilde{\boldsymbol{\omega}}_b\,{}_b\tilde{\boldsymbol{\omega}}_b\,{}_b\mathbf{r}_{o/cg}\right)_i
\end{aligned}
\tag{3.19}
$$

Furthermore, this system can be represented via a state vector, which is defined in equation (3.20) where *u*, *v*, and *w* represent the velocity components of the body, *p*, *q* and *r* represent the rotation rates of the body about the basis vectors in the body frame, x_{cg}, y_{cg}, and z_{cg} represent the displacement of the body in the inertial frame, and φ, θ, and ψ represent the orientation of the body.

$$
\mathbf{x} = \begin{bmatrix} u & v & w & p & q & r & {}_Ix_{cg} & {}_Iy_{cg} & {}_Iz_{cg} & \phi & \theta & \psi \end{bmatrix}^T \tag{3.20}
$$

Since we have isolated the state derivatives and also defined an invertible mass matrix, equations (3.18) and (3.19) can be rewritten as equation (3.21)

$$\dot{\mathbf{x}} = H^{-1} f(\mathbf{x}, \mathbf{u}) \tag{3.21}$$

where **u** represents a vector of control inputs, which are defined and discussed in Section 3.2. Equation (3.21) can be integrated numerically in time to determine the longitudinal response of the system.

3.2. Prescribed Wing Motion

The abstracted wing kinematics for rigid wing analysis are described using relations provided by Berman and Wang [4]. The flapping motion with respect to the wing root is described by equation (3.22), where ζ, Z and f are the instantaneous flapping angle, flapping amplitude, and flapping frequency, respectively. Additionally, as K varies from 1 to 0, the flapping waveform varies from a triangular wave to a sinusoidal wave. The flapping offset angle, ζ_φ biases the flapping toward the ventral ($+\zeta_\varphi$) or dorsal ($-\zeta_\varphi$) side of the wing root. In this study, we keep $K = 0.01$ so that the flapping motion is nearly sinusoidal. For flexible wing simulations, only the flapping amplitude is prescribed and the wing deforms in a manner described in Section 3.3.4.

$$\zeta(t) = \frac{Z}{\sin^{-1} K} \sin^{-1}\left(K \cos\left[2\pi f t\right]\right) + \zeta_\phi \tag{3.22}$$

Equation (3.23) describes the pitch angle α, which can vary from a sinusoidal wave to a square wave as C_α varies from 0 to ∞. The flapping amplitude A determines the magnitude of angular rotation from the initial, vertical orientation of the wing. In this work, we do not consider different upstroke and downstroke flapping angles (as is

considered by Sun and coworkers [15,17,81]) since varying the stroke plane angle allows us to re-orient the thrust vector. The timing of wing rotation is controlled by α_φ, which can be positive for advanced rotation, zero for symmetric rotation, and negative for delayed rotation. Vertical deviation angle out of the stroke plane is not considered. Other wing kinematic representations are available in the literature including those of Sun [15]. In order to facilitate comparison with their work, we calculate the necessary values of α_φ and C_α to match their duration and timing of pitch rotation, which is described in the Appendix. The variation in wave form of the pitch angle $\alpha(t)$ is demonstrated in Figure 3.3 for different values of C_α.

$$\alpha(t) = \frac{\mathrm{A}}{\tanh\left(C_\alpha\right)} \tanh\left[C_\alpha \sin\left(2\pi ft - \alpha_\phi\right)\right] \tag{3.23}$$

To obtain the velocities and accelerations of the wing, which determine the aerodynamic in the quasi-steady model and inertial forces, we take the appropriate number of derivatives of equations (3.22) and (3.23).

In this study, we vary the pitch axis location which is given in terms of the chord, x_p/c. We vary the pitch axis from the leading edge ($x_p/c = 0$) to the three-quarter chord, ($x_p/c = 0.75$). The x-axis of the wing is always co-located with the pitch axis. Varying x_p/c also changes the inertial properties of the wing, which are detailed in the Appendix.

Some of the wing kinematic parameters can also be chosen to be control inputs. Motivated by the work of Faruque and Humbert [9] and Badrya et al. [91], we select the stroke plane angle, β, flapping amplitude, Z, and the flapping offset angle, ζ_φ, as the three control inputs to actuate the three degree of freedom (3-DOF) system. Each control

primarily affects the horizontal, vertical, and angular degree of freedom respectively. For all simulations, we retain a constant value of the stroke frequency (f = 218 Hz) and vary flapping amplitude, based on the findings of Altshuler et al. [33] that insects modify their flapping amplitude vice the flapping frequency to increase thrust.

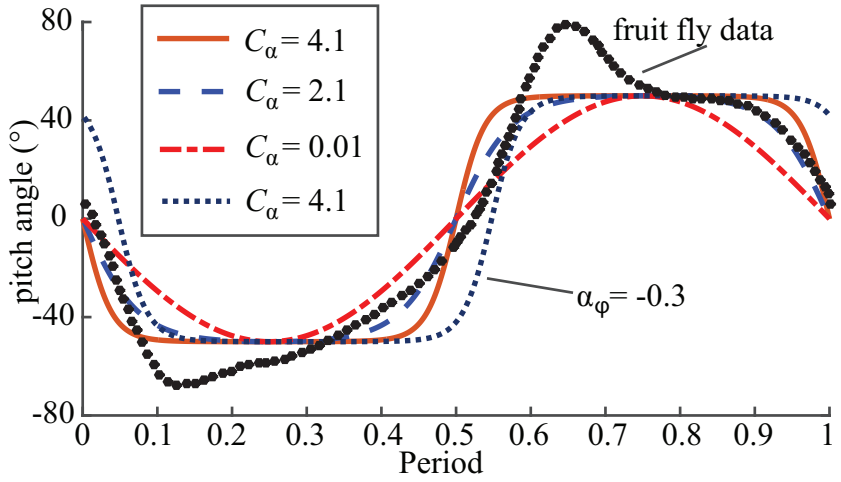

Figure 3.3. The pitching waveform produced by A = 50° and various values of C_α for symmetric (α_φ=0) pitching motion as well as a pitching motion with delayed rotation (α_φ=-0.3) are plotted with the pitching data from experiments on live fruit flies as reported in Fry et al. [32]**.**

3.3. Aerodynamic Model

The forces and moments generated by the flow of the air over the wings and body are the most significant source of forces, so care must be taken to model their effects accurately. The results in this study are based on three different models for the aerodynamic forces:

1. A quasi-steady model based on Sane and Dickinson [27].
2. A model that utilizes the direct numerical simulations of the Navier-Stokes (NS) equations.

3.A CFD-CSD solution of a flexible wing, solving for the Navier-Stokes equations and linear beam equations in a tightly coupled manner.

Because our analysis is restricted to hover, any aerodynamic forces generated by the body can be neglected. We only simulate a single wing, assuming left-right symmetry of the system confined to the 3-DOF pitch plane. We nondimensionalize all forces by the maximum translational velocity of the center of the second moment of wing area r_2, $U=2\pi f Z r_2$. Weis-Fogh [92] and Lua, Lim, and Yeo [93] determined that the lift and drag forces on the wing are proportional to the speed of the center of the second moment of wing area, such that this location serves as the spanwise location of interest for this study.

3.3.1. Quasi-steady Aerodynamic Model: Forces

The Sane and Dickinson model [27] has been used extensively in the past by others, and it will be incorporated into this study as well. Their model attempts to capture the quasi-steady contributions of translational lift, F_{trans}, rotational lift from circulation, F_{rot}, and added mass force, F_{am}, per equation (3.24). Although Sane and Dickinson [27] identify that additional forces are generated via wake capture, this highly nonlinear phenomena is not amenable to an algebraic representation, and it is omitted from the model. They represented the translational force in terms of the components that are normal (lift) and tangential (drag) to the flapping motion, because in their experiments the flapping motion defined the relative wind. The translational lift and drag coefficients they published were obtained by fitting an expression to their experimental results for a range of angles of attack AoA = -10° to 90°, resulting in equations (3.25) and (3.26).

$$F_{w,Aero} = F_{am} + F_{trans} + F_{rot} \tag{3.24}$$

$$F_{trans} = \left\| \begin{matrix} L_{trans} \\ D_{trans} \end{matrix} \right\| = \frac{1}{2}\rho U^2 Rc \left\| \begin{matrix} C_L \\ C_D \end{matrix} \right\| \tag{3.25}$$

$$\begin{aligned} C_L &= 0.225 + 1.58\sin(2.13AoA - 7.2) \\ C_D &= 1.92 - 1.55\cos(2.04AoA - 9.82) \end{aligned} \tag{3.26}$$

The quasi-steady model requires the motion to be expressed in the wing frame. The angle of attack is determined by equation (3.27), where ${}_w\mathbf{v}_{ac}$ is the velocity vector of the quarter chord of the airfoil and includes contributions from the body motion and $\hat{\mathbf{j}}_w$ is the unit vector aligned with the chord of the wing.

$$AoA = \tan^{-1}\left(\frac{\left\| {}_w\mathbf{v}_{ac} \times \hat{\mathbf{j}}_w \right\|}{{}_w\mathbf{v}_{ac} \cdot \hat{\mathbf{j}}_w} \right) \tag{3.27}$$

The rotational force arises from the wing's rotation imparting additional circulation to the flow. Sane and Dickinson [27] demonstrated that the rotational force coefficient can vary significantly from the theoretically reported value of $C_{rot} = \pi(0.75 - x_p/c)$ because it also depends on the nondimensional rotational velocity $\hat{\omega}$. Ellington [94] defines $\hat{\omega} = \omega c/U_{tip}$, where ω is the absolute angular velocity of the wing about is pitch axis, c is the mean chord, and U_{tip} is the reference velocity at the wing tip. Thus, the rotational force coefficient is dependent on both the axis of pitch rotation and the rotation rate. We utilize this dependence on $\hat{\omega}$ in determining the rotational lift. Because Sane and Dickinson's [27] experiments lie well below the $\hat{\omega}$ generated by insect wings, we

further modify the rotational force coefficient using NS solutions of cases that better represent the nondimensional rotational frequency of insects (more information is provided in the Appendix). The rotational force becomes equation (3.28) where the wing shape parameters for *Diptera* reported in [88] of $\hat{r}_1(\hat{v})$=0.52 and $\hat{v}$=1.1 are used.

$$F_{rot,z} = -C_{Rot}\rho|U|\dot{\alpha}c^2R\hat{v}\hat{r}_1(v), \tag{3.28}$$

Added mass forces arise due to the accelerations produced by both the flapping and pitching motion of the wing. We modify Sane and Dickinson's [27] equation to account for differing pitch axes per the expressions given in Leishman [95] and Babinsky et al. [96] to arrive at equation (3.29). The rotational and added mass forces arise strictly from the pressure distribution, so they are assumed to act perpendicular to the chord, in the z_w direction.

$$F_{am,z} = \pi\rho Rc^2\left[\frac{r_2}{4}\left(\ddot{\zeta}\sin AoA + \dot{\zeta}\dot{\alpha}\cos AoA\right)\hat{v}\hat{r}_1(v) - \ddot{\alpha}\frac{c}{8}\left(\frac{x_p}{c} - \frac{1}{2}\right)\hat{v}\right] \tag{3.29}$$

3.3.2. Quasi-Steady Aerodynamic Model: Moments

The location of the center of pressure can be difficult to determine analytically. It is more convenient to calculate the equivalent moments about the quarter-chord. Additionally, some wing motions can produce no net force, but still yield a moment. In the course of this discussion the intersection of the quarterchord and the radius of the second moment of wing area, r_2, is termed the aerodynamic center because it is the point

where the circulatory aerodynamic forces are assumed to act, although strictly speaking it is not the location where $dC_M/d\alpha = 0$. Once the moment about the quarter chord is known, the moment about any axis (such as the pitch axis) can be calculated using equation (3.30).

$$\mathbf{M}(\mathbf{r}) = (\mathbf{r} - \mathbf{r}_{ac/o}) \times \mathbf{F}_{circ} + (\mathbf{r} - \mathbf{r}_{mc/o}) \times \mathbf{F}_{am} + \mathbf{M}_{am} + \mathbf{M}_{circ} \tag{3.30}$$

The circulatory components of the aerodynamic force that arise due to translation and rotation are assumed to act at the quarter-chord based on the work of Theordorsen [3] and presented in Bisplinghoff et al. [97] and Fung [98]. Additionally, the added mass force is assumed to act at the mid chord. Although several researchers in flapping wing aerodynamics have provided analytical expressions for the circulatory forces [24,99], few provide expressions or data on the moments.

1.Berman and Wang [4] provide expressions for both normal and tangential force as well as aerodynamic torques that result from both added mass and viscous forces. However, they do not address moments that arise from circulation around a moving flat plate.

2.Orlowski and Girard [11] calculate aerodynamic pitching moments by applying both added mass and circulatory lift and drag to the center of pressure of the airfoil, which is calculated based on the chosen geometry of the hawkmoth wings. However, they do not present a method for determining the numbers that they use, nor do they present moment relations independent of lift and drag forces.

3.Deng, Schenato, Wu and Sastry [100] also calculate the aerodynamic forces using Dickinson's model [27] and then apply those forces at the center of pressure of the wing, which they estimate to be in the range of 0.6-0.7R and 0.25c.

4.Motivated by the lack of center of pressure data in the literature, Zhao, Huang, and Deng [101] conducted experiments of a translating insect wing using materials of varying stiffness immersed in mineral oil. They were the first to publish detailed center of pressure data, however, their results are of limited utility in flapping wing analysis because their wing kinematics were limited to translation from 1 to 180°, with a constant angle of attack. Therefore, the many of the unsteady mechanisms such as the terms involving $\dot{\alpha}$, $\ddot{\alpha}$ are not included even though these rates are high for insect wings. In spite of these limitations, Zhao et al. [101] demonstrate that the center of pressure varies between 52% - 62% span, so using $r_2 = 0.55R$ results in a good approximation of the center of pressure for the wing

5.Faruque and Humbert [9] utilize Sane and Dickinson's QS model [27] for wing force production, but do not present any moment relations. It is assumed that they apply their forces at center of pressure, but an expression for calculating the center of pressure location is not given.

6.Sane and Dickinson [27] and Wang, Birch, and Dickinson [36] present analytical expressions for translational, rotational, and added mass forces and compare them against experimental data, but their experimental apparatus was not able to measure the pitching moments generated by the wing motion in their experiments.

7.Khan and Agrawal [47] conducted an experiment and recorded the moment data. However, their moment predictions are a result only of the circulatory lift contributions taken at the center of pressure of the wings.

8.Truong et al. [102] present a method of determining the pitching moment produced by the wing, based on quasi-steady analysis by positing that the translational forces act at the quarterchord and the rotational and noncirculatory forces act at the midchord. Again, no pure moment relations are provided.

9.Doman et al. [67,103] use the translational force expressions provided by Dickinson and apply them at the center of pressure of the wing. No other forces or moments are considered.

10.Usherwood and Ellington [104,105] conducted experiments on model hawkmoth wings and describe the means by which they measured moments, but they did not publish the moment results.

11.Those researchers using solutions to the Navier-Stokes equations including Liu et al. [28,90], Sun and coworkers [15,17,18,29,106], and Bush and Baeder [107] are able to return both aerodynamic forces and pitching moment information directly. Meng, Xu and Sun [35] published high fidelity simulations in order to analyze the effect of wing venation and corrugation on the aerodynamic forces and moments. They produced detailed time histories of the moments for various kinematic patterns, vein patters, and aspect ratios, and their data was used in validating the moment histories of the current study. However, they do not describe the aerodynamic sources of these moments or attempt to provide a surrogate model to calculate them. Many other researchers have utilized similar computational methods to investigate the aerodynamics of both rigid and

flexible wings and wing sections, and the lift production mechanisms have been described in length [12,13,29,31], but none of those referenced here consider the moment or the center of pressure as a variable of interest.

In spite of the relative silence within the literature on the topic, classical unsteady aerodynamic theory that considers airfoils pitching $\left(\dot{\alpha},\ddot{\alpha}\right)$ and plunging $\left(\dot{h},\ddot{h}\right)$ while subject to a freestream velocity predicts that additional moments are generated by such airfoil motion. Since these classical theories were developed for two-dimensional airfoils, they predict the moment per unit span, *M'*. Additionally, these theories typically utilize the semichord, $b = c/2$, and they track the pitch axis location via $a = 2x_p/c\text{-}1$, which ranges from -1 to 1 as the pitch axis is moved from the leading edge to the trailing edge.

Bisplinghoff [97] shows that pure plunging motion $\dot{h}$ develops a pressure distribution around the airfoil that that produces no net lift but produces a destabilizing moment per equation (3.31). Fung [98] demonstrates that a nose down couple is generated by $\ddot{\alpha}$ given by equation (3.32).

$$M'_{am1} = \pi\rho b^2 U(t)\dot{h} \tag{3.31}$$

$$M'_{am2} = -\frac{\pi\rho b^4}{8}\ddot{\alpha} \tag{3.32}$$

Additionally, Leishman [95] shows that a pitching velocity $\dot{\alpha}$ creates an opposing moment about the quarterchord per equation (3.33).

$$M'_{circ} = -\frac{\pi}{2}\rho b^3 U(t)\dot{\alpha} \tag{3.33}$$

Since these relations were developed for airfoils subject to a freestream velocity, each term needs to be further identified within the context of a flapping wing. The pitching terms, $(\dot{\alpha}, \ddot{\alpha})$ directly translate to the pitching motion of the wing. The plunging velocity $\dot{h}$ can arise when the wing is flapping out of plane. Since this study is restricted to considering only hover, this term becomes $\dot{h} = r_2\dot{\delta}$, where δ is the out of plane deviation angle. If no body motion is considered, the instantaneous translational velocity of the aerodynamic center is $U(t) = \dot{\zeta}(t)r_2$. However, in the present study, body motion can also modify *U*, so we retain this term. Making the appropriate substitutions and multiplying by the wing length yields equation (3.34).

$$M_{am} + M_{circ} = \pi\rho b^2 R\left[r_2 U(t)\dot{\delta} - U(t)\frac{b}{2}\dot{\alpha} - \frac{b^2}{8}\ddot{\alpha} \right] \tag{3.34}$$

We further modify equations (3.31) through (3.34) to accommodate body rotations. In equation (3.33), the pitching velocity becomes the component of total wing velocity in the $\mathbf{i}_w$ direction. In equation (3.34), the $\dot{\delta}$ term drops out since angular deviation is not considered. Combining all of these terms results in equation (3.35).

$$M_{am} + M_{circ} = \pi\rho b^3 R\left[-U(t)\frac{b}{2}\left({}_w\boldsymbol{\omega}_{w/I} \cdot \mathbf{i}_w \right) - \frac{b}{8}\ddot{\alpha} \right] \tag{3.35}$$

The equations of motion that were presented in Section 3.1.3 assumes that the lift force is applied at the quarterchord. Thus, the residual moment that acts at the quarterchord must be determined. Equation (3.30) can therefore be re-written as

$$\mathbf{M}_{ac} = \left(\mathbf{r}_{ac/o} - \mathbf{r}_{ac/o}\right) \times \mathbf{F}_{circ} + \left(\mathbf{r}_{ac/o} - \mathbf{r}_{mc/o}\right) \times \mathbf{F}_{am} + \mathbf{M}_{am} + \mathbf{M}_{circ} \tag{3.36}$$

As can be seen, the first term drops out. Since the added mass force acts at the midchord, it contributes to a moment about the quarter chord, and the pure couples that are described above also contribute. The added mass forces that exist on a pitching and plunging airfoil in a freestream already appear in the F_{am} expression, so we can simply take the vector cross product $\left(\mathbf{r}_{ac/o} - \mathbf{r}_{midchord/o}\right) \times \mathbf{F}_{am}$ to determine their contribution. Since the aerodynamic center and midchord only differ in the y_w direction, we can substitute $0.25c\mathbf{j}_w$. As such, the moment about the aerodynamic center is calculated using equation (3.37).

$${}_w\mathbf{M}_{ac} = 0.25c\mathbf{j}_w \times {}_w\mathbf{F}_{am} - \pi\rho b^2 R\left[\frac{b}{2}U(t)\left({}_w\boldsymbol{\omega}_{w/I} \cdot \mathbf{i}_w\right) + \frac{b^2}{8}\ddot{\alpha}\right]\mathbf{i}_w \tag{3.37}$$

3.3.3. High Fidelity Aerodynamic Model for Rigid Wings

In order to provide a point of comparison against the coupled CFD-CSD solver that will be discussed below, the rigid wing is also modeled using a well-validated Navier-Stokes solver. The case setup requires the kinematics of the wing as described in

Section 3.2 to be imposed on a quiescent fluid. The fluid response and resulting viscous stress and pressure distributions on the body are described by the unsteady, incompressible Navier-Stokes equations given in equation (3.38) where the asterisk (*) indicates variables that have been nondimensionalized.

$$\nabla^* \cdot \mathbf{V}^* = 0$$
$$\frac{k}{\pi}\frac{\partial \mathbf{V}^*}{\partial t^*} + (\mathbf{V}^* \cdot \nabla^*)\mathbf{V}^* = -\nabla^* p^* + \frac{1}{Re}\Delta^* \mathbf{V}^* \tag{3.38}$$

The velocity field **V** is normalized with the reference velocity U, or $\mathbf{V}^* = \mathbf{V}/U$. Time is normalized by the flapping period ($1/f$), $t = ft$. Lengths are normalized by the mean wing chord c, and pressure is normalized per $p^* = p/\rho U^2$. The reduced frequency k in hover reduces to a geometric relationship that is governed by the stroke amplitude: $k = \pi fc/U = c/(2\hat{Zr}_2)$. The reduced frequency for all simulations based on the flapping amplitude required to hover is k = 0.20 to 0.252, which is the same reduced frequency range of fruit flies and other insects [12]. At this reduced frequency, the flow is fully unsteady, further suggesting that only the unsteady Navier Stokes equations can resolve the true nature of the fluid mechanics.

The Reynolds number is defined as $Re = Uc/\nu$. For simulations using fruit fly morphological parameters in the NS framework, Re = 100. In this Reynolds number regime, the fluid flow can be considered as laminar and the computational accuracy of the Navier-Stokes equation solver employed in this study is satisfactory [31]. These equations are solved in two dimensions using a well-validated structured, finite-volume, pressure-based incompressible Navier-Stokes equation solver used extensively in

flapping wing studies by Shyy and coworkers [21,30]. The two dimensional solutions to this problem have been previously shown to be a good approximation of the three dimensional aerodynamics at $Re=O(10^2)$ [31]. The effects of spanwise flow that seem to stabilize the LEVs [108] or LEV-tip-vortex interaction [109] on the overall aerodynamics are less important than at higher Reynolds numbers [110,111]. Also, the characteristics of the LEVs in two-dimensions for plunging motions are representative of three-dimensional flapping wings as long as the stroke-to-chord ratio is within the range of typical insects, i.e. around 4 to 5 [36], which we consider in this study. The pressure and shear stress distributions are integrated to yield the forces and moments of the wing about the wing's pitch axis at each time step. Any use of the term CFD in this paper refers to this model. The further descriptions of the grid, time step, and numerical setup are provided in the Appendix.

3.3.4. Fluid Structure Interaction for Flexible Wings

The case setup for the coupled Navier-Stokes and Euler-Bernoulli elastic beam solver follows the work of Kang et al. [12], Kang and Shyy [1], and Sridhar and Kang [13], and is summarized briefly here. A key feature of the flexible wing simulations is that the pitch angle of the wing is not prescribed. Rather, it results from the dynamic balance between the wing's inertia, the wing's stiffness, and the resulting fluid forces. For our purposes, it is sufficient to address only the chordwise flexibility and represent the flexible wing as a homogeneous elastic beam [19,20] [24]. The interplay of the fluid flow with the shape compliance and transient response is nonlinear and intriguing even at Re=100, which is addressed in Kang and Shyy [112].

This relationship can be modeled by the nondimensional Euler-Bernoulli beam equation given in [12] that describes the transverse deflection of the beam, v, as a function of space and time. In equation (3.39) the force, F^*, is the transverse component of the aerodynamic forces per unit length. This force is determined from the pressure distribution based on the solutions to the NS equations and is nondimensionalized using $F^*=F/(c\rho_f U^2)$. The effective inertia is the inertia of the wing normalized by the fluid dynamic forces. It is given by $\Pi_0=\rho^* h_s^* (k/\pi)^2$ [12] where ρ^* is the ratio of wing density to the density of air, $h_s^*=h_s/c$ is the thickness to chord ratio, and k is the reduced frequency, which was defined in Section 3.3.3. The wing thickness-chord ratio, h_s^*, is taken to be 1.5×10^{-3} based on the observations of Lehman et al. [113] and Lehman and Dickinson [57]. The effective stiffness normalizes the wing stiffness by the fluid dynamic variables and is given by $\Pi_1=Eh_s^*/(12\rho_f U^2)$ [12] where E is Young's Modulus and the other variables have already been defined.

$$\Pi_0 \frac{\partial^2 v^*}{\partial t^{*2}} + \Pi_1 \Delta^{*2} v^* = F^* \tag{3.39}$$

To determine the influence of wing flexibility on the flight performance and stability of the FWMAV, we adjust the stiffness of the wing to see if there is an optimal range of wing flexibility from the standpoint of either power or stability. This variation is reflected in the resulting frequency ratios per equation (3.40). The coefficient k_1 is based on the first natural frequency in the chordwise direction, and is set to 1.875 for all of the cases in this study [12].

$$\frac{f}{f_1} = \frac{2\pi c f}{k_1^2 h_s}\sqrt{\frac{12\rho_w}{E}} \tag{3.40}$$

We hold several variables in equation (3.40) constant in the course of this study. The frequency is fixed at $f = 218$ Hz based on the observations of fruit flies given in [75]. The density of the wing is taken to be $\rho_w = 1\times10^3$, based on Kang et al. [12]. Therefore the frequency ratio is a function of Young's Modulus E and the flapping amplitude, which is included in the reduced frequency k. Sunada et al. [114] report that dragonfly wings have frequency ratios in from 0.3 to 0.45, and this range of values is used in this study as well. Based on all of the other fruit fly parameters listed above, we vary E from 5.15×10^8 to 8.5×10^8 N/m^2.

The beam is modeled with 51 nodes equally distributed over two dimensional beam with flat edges [1]. As the flat plate follows the imposed horizontal motion, equation (3.22), at the leading edge, the resulting fluid dynamic force dynamically balances with the wing inertia and the elastic bending forces which yields a time varying solution of the wing's deformation. The resulting wing deformations $w=v-h$ can also be approximated as a pitch rotation $\alpha_{flex}(t) = \tan^{-1}(w(t))$, the angle between the trailing-edge (TE) and LE [1]. In general, this passive pitch response is not a simple sinusoidal function. The passive pitch angle creates an angle of attack (AoA) that is approximately $AoA = \pi - \alpha_{flex}$. In the flexible wing simulations, the passive pitch angle is not used directly to calculate the aerodynamic forces. Rather, they are determined by integrating the shear and pressure distributions around the wing at each time step. However, the time history of the passive pitch angle is recorded, and when needed, it can be replayed in both rigid NS solutions and quasi-steady solutions.

We use the same structured, pressure-based finite volume solver to solve equation (3.38) that was discussed in the previous section [21,30]. We solve equation (3.39) using an in-house finite element representation of an Euler-Bernoulli beam model. Any use of the term CSD in this paper refers to this model. Equations (3.38) and (3.39) are solved independently, and coupling is achieved via a time-domain partitioned process. At each time step the fluid and structural solutions are iterated until sufficient convergence is reached. Details of the fluid-structure interaction and careful validation studies against well-documented experimental results are shown in previous studies [12,115–117]. The computational grid is re-meshed whenever the wing moves or deforms using the radial basis function interpolation scheme [12,118].

3.3.5. Power Required

Once the aerodynamic forces are determined using either a quasi-steady or Navier-Stokes model, the power is calculated from the time histories of the wing's motion and the forces it generates. Alternatively wing power can be estimated by summing the induced, inertial, and profile power contributions of the whole insect on a stoke-averaged basis [54,55,57]. In this study, we adopt the first approach as it has been shown to be more accurate [32,106]. Since the wing is restricted to purely angular flapping and pitching motions, the power required to actuate the wing is the product of the instantaneous moment required and angular velocity in the proper frame. The moment required is the difference between the change in angular inertia of the wing about the wing root and the aerodynamic moment as in equation (3.41).

$$\begin{aligned}\mathbf{M}_{req} = &\left({}_{w}I_{wo}\,{}_{w}\dot{\boldsymbol{\omega}}_{w} + {}_{w}\boldsymbol{\omega}_{w} \times {}_{w}I_{wo}\,{}_{w}\boldsymbol{\omega}_{w} + m_{w}\,{}_{w}\mathbf{r}_{wg/o} \times {}_{w}\mathbf{a}_{o} \right) \\ &- \left({}_{w}\mathbf{M}_{Aero,w} + {}_{w}\mathbf{r}_{ac/o} \times {}_{w}\mathbf{F}_{Aero,w} \right)\end{aligned} \tag{3.41}$$

Most researchers that directly calculate wing power based on the motion only consider the first two inertial terms. When fully decomposed, these first two terms match the expressions used in Whitney and Wood [43] and Bergou and Wang [37] for the calculation of the moment required to pitch the wing, although neither of these studies calculates the power to do so. The third term, $m_{w}\,{}_{w}\mathbf{r}_{wg/o} \times {}_{w}\mathbf{a}_{o}$, arises when the wing root is allowed to move relative to the inertial frame, which is the case in our simulations, although it is a small contributor to the sum. Secondly the inertia tensor about the wing root ${}_{w}\underline{I}_{wo}$ is an important entity. Proper accounting of each term of this tensor is essential in calculating passive wing pitch for certain kinematical patterns, especially as the axis of pitch rotation x_p/c is adjusted. The details of the inertia calculation are provided in the Appendix.

The angular velocity and acceleration of the wing have been previously derived, but they are reproduced in equation (3.42) for convenience.

$$\begin{aligned}{}_{w}\boldsymbol{\omega}_{w/I} &= R_{b\to w}\,{}_{b}\boldsymbol{\omega}_{b/I} + R_{\omega\to w}\begin{bmatrix}\dot{\alpha}\\ \dot{\zeta}\\ \dot{\delta}\end{bmatrix} \\ {}_{w}\dot{\boldsymbol{\omega}}_{w/I} &= R_{b\to w}\begin{bmatrix}p\\ q\\ r\end{bmatrix} \times R_{\omega\to w}\begin{bmatrix}\dot{\alpha}\\ \dot{\zeta}\\ \dot{\delta}\end{bmatrix} + R_{b\to w}\begin{bmatrix}\dot{p}\\ \dot{q}\\ \dot{r}\end{bmatrix} + \dot{R}_{\omega\to w}\begin{bmatrix}\dot{\alpha}\\ \dot{\zeta}\\ \dot{\delta}\end{bmatrix} + R_{\omega\to w}\begin{bmatrix}\ddot{\alpha}\\ \ddot{\zeta}\\ \ddot{\delta}\end{bmatrix}\end{aligned} \tag{3.42}$$

Because the angular velocity components of the wing contain body rates, the body motion affects the required wing power. At each time step, the components of the moment are multiplied by the corresponding components of the angular velocity of the wing with respect to the body per equation (3.43), which is an equivalent expression to that derived by Bergou and Wang [37]. Each rotation occurs its own reference frame so converting both the required moment and the angular velocity to the proper reference frame is important.

$$\begin{aligned} P_{pitch} &= {}_{w}M_{req,x}\,{}_{w}\omega_{w/b,x} \\ P_{flap} &= {}_{usp}M_{req,y}\,{}_{usp}\omega_{w/b,y} \end{aligned} \tag{3.43}$$

Equation (3.43) results in a time-history of power required, which returns both positive and negative values. When P_{pitch} or P_{flap} is positive, power is required in order to achieve desired wing motion. Positive power typically occurs in portions of the stroke where the wing must be accelerated. Negative power typically occurs in the portions of the stroke where the wing must be decelerated. Many researchers simply neglect negative power in their calculations [4,55,60]. In so doing, they assume that this power cannot be stored and re-used, but they also assume that power is not expended during these portions of the stroke. We use the term positive power P_{pos}=mean($\forall P(t)>0$) to refer to this definition, and this is the power in view throughout this paper, which facilitates comparisons to those values reported in other studies.

3.4. Flight Simulations of the Coupled Model

The method for solving the flight dynamics equations as a time evolution of the states was provided in Section 3.1.5. The aerodynamic forces and moments are calculated directly by the CFD or CFD-CSD solvers by integrating the pressure and shear forces on the wing. The moments are summed about the pitch axis that was selected during case set-up. They are nondimensionalized and provided to the equations of motion along with the current state vector. The equations of motion utilize dimensionalized forms of the forces based on the insect-specific parameters, and are solved to yield the body accelerations for each time step. The body accelerations are integrated in time using a second-order Adams Bashforth scheme to yield the body velocities and displacements. The displacements with respect to the inertial frame are then transformed back into the computational frame and provided to the Navier-Stokes solver. The body motion is combined with the change in position and angle due to the prescribed wing motion at each step time step, and the computational grid is re-meshed at each time step. Thus, the solution is a tight three-way coupling of the governing equations, depicted in Figure 3. This tight coupling is selected for several reasons instead of cycle-averaging the forces and moments. First, Orlowski and Girard [14] as well as Taha, et al. [77] describe the various ways that averaging the forces before applying them to the flight dynamics can bias the solution. Secondly, averaging the forces or accelerations introduced unacceptable oscillations in the simulation that are addressed in the Appendix. This integrated framework of aerodynamics, structural dynamics, and flight dynamics constitutes a free flight simulator of the FWMAV with flexible wings.

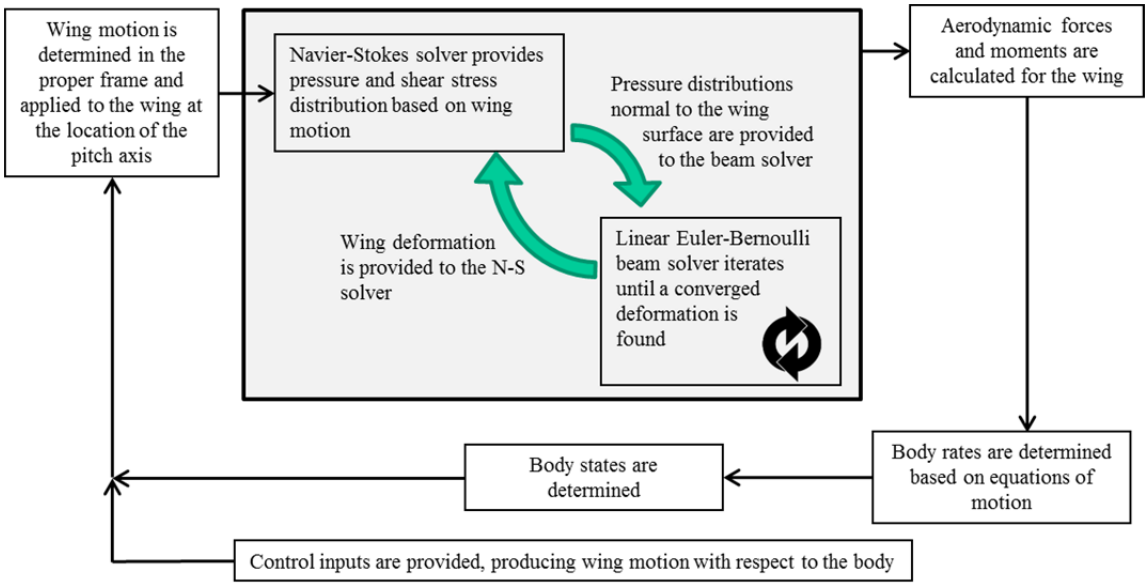

Figure 3.4. Schematic of three-way coupled CFD-CSD-EOM solver.

3.5. Determining Equilibrium and the System Poles

A primary goal of this study is to determine the stability characteristics of a FWMAV in different configurations with rigid or flexible wings. The primary means of determining the stability of the flyer is by evaluating its response to perturbations about an equilibrium condition. This process is detailed in Section 3.5.3, but finding equilibrium is an important prerequisite. As discussed in Chapter 2, many researchers do not tightly couple the equations of motion to the aerodynamic model, and therefore have no need to determine equilibrium. They simply assume equilibrium by balancing forces in the averaged sense. The current study, however, considers free flight, so both initial conditions and required control inputs need to be determined that places the system in equilibrium.

In this study, we restrict our analysis to the longitudinal degrees of freedom in the pitch plane, and we consider only the hovering state. Therefore, the state vector is redefined by equation (3.44)

$$\mathbf{x} = \begin{bmatrix} u & w & q & {}_I x_{cg} & {}_I z_{cg} & \theta \end{bmatrix}^T \tag{3.44}$$

In order to find the trimmed state at hover, we can express equation (3.21) as equation (3.45), which expresses the rates $\dot{\mathbf{x}}$ in terms of the states $\mathbf{x}$, the system matrix A, the vector of controls $\mathbf{u}$, and the control matrix B. As discussed in Section 3.2, we utilize the flap amplitude, stroke plane angle, and flapping offset angle as controls: $\mathbf{u} = [Z\ \beta\ \zeta_\varphi]^T$.

$$\dot{\mathbf{x}} = A\mathbf{x} + B\mathbf{u} \tag{3.45}$$

When placed in the form of equation (3.45), equilibrium can be determined numerically by any minimization procedure that drives the rate vector $\dot{\mathbf{x}}$ to zero. We construct the A matrix numerically by perturbing each degree of freedom and using a central difference approximation to compare the average system response across one full cycle with and without a perturbation. The control matrix B is obtained by perturbing each control in a similar fashion and determining its effect on the average system response. The system matrix represents a first order, linear time invariant representation of the nonlinear system.

In order to achieve hovering trim, we require the cycle-averaged acceleration and the cycle-average velocity to be zero. That is, $\dot{\mathbf{x}}_{\text{ave}} = \text{mean}([\dot{u}\ \dot{w}\ \dot{q}\ u\ w\ q]^{\text{T}} = \mathbf{0}$. Using

successive linear approximations of the full nonlinear system, a multi-degree of freedom Newton-Raphson scheme is used to find the necessary control inputs, Z, ζ_φ , and β, and initial conditions, u_0, w_0, q_0, and θ_0 that place the system in equilibrium. The initial positions of the body ${}_Bx_{cg}$ and ${}_Bz_{cg}$ are inconsequential from the standpoint of generating aerodynamic forces, and they are set to the origin. Convergence is set such that $\left\|\dot{\mathbf{x}}\right\| < 1\times10^{-2}$ where the rate vector contains both accelerations (m/s^2) and velocities (m/s).

3.5.1. Determining Equilibrium of the Coupled NS-EOM System

In the QS simulations, where the forces and moments depend on the velocities and accelerations, the disturbance in each degree of freedom can be directly input for a full flapping cycle. The approach described in the previous section is applied directly to the system to determine equilibrium of the QS model.

Determining the equilibrium of the NS model is more complicated for two primary reasons. First, the velocity perturbations cannot simply be applied to the NS model. Secondly, the process of finding equilibrium using the Newton-Raphson scheme requires multiple function calls to the flight simulator. Construction of the *A* and *B* matrices requires at least fifteen function calls. A typical trim procedure that take between 5 and 15 steps will make between 100 and 300 function calls to the flight simulator. Completing this procedure with the NS model would be computationally inefficient and costly.

Therefore, in order to find equilibrium of the NS model, we utilize the method presented by Badrya et al. [91]. This method is an iterative scheme which applies the difference between the QS and NS-predicted forces to each successive trim solution until

the resulting accelerations are the same. Once this is enforced, the trim routine has successfully trimmed the fully coupled NS-flight dynamics system (to less than 3% gravitational acceleration). It is worth noting that this CFD-coupled trim method was not effective unless we used all of the components of the QS model available (translational, rotational, and added mass contributions).

The steps in this process are as follows [91]:

1. Select control inputs $\mathbf{u}_0 = [\zeta_0 \; \beta_0 \; \zeta_{\varphi,0}]^T$ and initial conditions $\mathbf{x}_0 = [u_0 \; w_0 \; q_0 \; \theta_0]^T$.

2. Use the Newton-Raphson scheme to determine trim control inputs $\mathbf{u}_{t,i}$ and initial conditions $\mathbf{x}_{0t,i}$ based on the QS-EOM model. Here, the subscripts *t* and *i* refer to the trimmed condition and the *i*th iteration, respectively.

3. Using $\mathbf{u}_{t,i}$ and $\mathbf{x}_{0t,i}$, determine the accelerations of the body using the NS-EOM model. The forces and moments are also stored.

4. Determine the time-history of the differences between the forces from the NS model and those from the QS mode, i.e. $\Delta\mathbf{F}(t) = \mathbf{F}_{NS}(t) - \mathbf{F}_{QS}(t)$.

5. Use the Newton-Raphson scheme to determine trim control inputs $\mathbf{u}_{t,i+1}$ and initial conditions $\mathbf{x}_{0t,i+1}$ where the forces used in the trim routine are the sum of the QS forces (which can change within the Newton-Raphson trimmer) and the $\Delta\mathbf{F}(t)$ determined in step 4.

6. If convergence is reached, the final $\mathbf{u}_{t,i+1}$ and $\mathbf{x}_{0t,i+1}$ are the trim inputs needed to achieve equilibrium in the NS-EOM model. If convergence is not reached, repeat steps 3 through 5.

Trimming the CFD-driven system was of critical importance in determining the system's stability. Without achieving free-flight equilibrium, the eigenvalues of the

system matrix do not reflect the system poles, which are only defined for an equilibrium state.

3.5.2. Determining Equilibrium for NS Solution for Flexible Wings

In order to determine the equilibrium for the couples FSI-EOM model, we modify the above procedure to account for wing flexibility. No QS-FSI model is currently available to permit a rapid trim procedure without running the NS-FSI solver. Therefore, we developed a trim procedure for the flexible wing, which has not previously reported. The steps are as follows:

1.Assume initial control inputs $\mathbf{u}_0 = [\zeta_0\ \beta_0\ \zeta_{\varphi,0}]^T$ and initial conditions $\mathbf{x}_0 = [u_0\ w_0\ q_0\ \theta_0]^T$.

2.Run a flexible NS case in order to determine the passive pitching schedule for α_{flex}. As we discuss in Section 5.2, the simulation is run until the sixth period with prescribed body motion, but no free body motion. During the seventh cycle, the passive pitch response of the wing changes slightly over the course of the stroke in the presence of the body motion. Therefore, the eighth cycle, which is more representative of later cycles, is averaged in order to determine the average acceleration. The pitch schedule, force histories and moment histories are all stored.

3.Determine a Fourier representation of α_{flex} based on the eighth cycle.

4.Simulate the insect using the QS aerodynamic model (without trim) using the Fourier representation of α_{flex} with the same $\mathbf{u}$ and $\mathbf{x}_0$ as the NS-FSI simulation to determine $\Delta\mathbf{F}(t) = \mathbf{F}_{NS\text{-}FSI}(t) - \mathbf{F}_{QS}(t)$.

5.Run the QS trimmer with α_{flex} schedule and the $\Delta\mathbf{F}(t)$ to determine a new set of inputs $\mathbf{u}_{t,i+1}$ and $\mathbf{x}_{0t,i+1}$.

6.Run a new flexible NS case using in the same manner described in step 2 but using $\mathbf{u}_{t,i+1}$ and $\mathbf{x}_{0t,i+1}$. The pitch schedule, force histories and moment histories are all stored.

7.If convergence is not achieved, repeat steps 3 through 6.

3.5.3. Determining the System Poles

As discussed in Chapter 2, the primary method used to determine the stability of the system is to analyze the open loop poles of the linearized system matrix A in equation (3.45), while in equilibrium. The system poles are the eigenvalues of the linearized system matrix, $\lambda_n = \sigma_n \pm \omega_n i$, for $n = 1$ to N, where N is the number of degrees of freedom. The real part of the pole, σ_n, corresponds to the rate of growth or decay of the response, and the imaginary part, ω_n, corresponds to the natural frequency of any oscillatory motion. A pole is unstable when $\sigma_n > 0$, it is considered neutrally stable when $\sigma_n = 0$, and it is stable if $\sigma_n < 0$. In order for a system to be stable, all of the poles must be stable; a single unstable pole causes the entire system to diverge [74]. The growth or decay rate of any pole can be conveniently converted to doubling time or half-life, $t_{double,n}$ or $t_{half,n} = \ln(2)/|\sigma_n|$, and the natural frequency can be used to determine the period of oscillation per $\tau_n = 2\pi/\omega_n$.

Even though the system matrix for the system confined to the pitch plane is a 6x6 matrix, the forces and moments do not depend on the x_{cg} or z_{cg}. Therefore, the rows and columns associated with these degrees of freedom are identically zero, and the system matrix reduces to a 4x4 matrix per equation (3.46). The stability derivatives X_u/m, X_w/m, W_q/m, Z_u/m, M_u/I_{yy}, etc. are defined in the manner of equation (3.47) and (3.48), where

the overbar indicates a cycle average of the acceleration in each degree of freedom and δ represents the perturbation in the appropriate degree of freedom (e.g. δu is a perturbation of the horizontal velocity in the body frame).

$$A = \begin{bmatrix} \frac{1}{m}X_u & \frac{1}{m}X_w & \frac{1}{m}X_q & g \\ \frac{1}{m}Z_u & \frac{1}{m}Z_w & \frac{1}{m}Z_q & 0 \\ \frac{1}{I_{yy}}M_u & \frac{1}{I_{yy}}M_w & \frac{1}{I_{yy}}M_q & 0 \\ 0 & 0 & 1 & 0 \end{bmatrix} \tag{3.46}$$

$$\frac{1}{m}X_u = \frac{{}_b\bar{\dot{u}}_{cg,x}(u_0 + \delta u, w_0, q_0, \theta_0) - {}_b\bar{\dot{u}}_{cg,x}(u_0, w_0, q_0, \theta_0)}{\delta u} \tag{3.47}$$

$$\frac{1}{I_{yy}}M_u = \frac{{}_b\bar{\dot{q}}_{cg}(u_0 + \delta u, w_0, q_0, \theta_0) - {}_b\bar{\dot{q}}_{cg}(u_0, w_0, q_0, \theta_0)}{\delta u} \tag{3.48}$$

For the QS model, once the system is in equilibrium, we take the eigenvalues of the most recent system matrix that was used to find equilibrium. This is not possible with the NS system. The previous section described how the system and control matrix used to find the equilibrium condition by approximating the NS solution using the QS solution and a correction factor. When evaluating the system poles of the NS-driven system, however, we must evaluate the system matrix in the full NS framework, and not simply the QS-corrected system matrix.

To construct the A matrix using the NS model, we start with the equilibrium initial conditions and control inputs. We then set up and run separate simulations for the hover condition (no perturbation) as well as for perturbations in the four relevant degrees

of freedom (δu, δw, δq, and $\delta\theta$). We then evaluate the derivatives using a forward difference approximation to compare the system response with and without a perturbation. A perturbation convergence study was performed in order to ensure that reducing the perturbation size did not change the system poles. In previous studies, Sun and Xiong [15] and Wu et al. [17] used perturbations of $\delta u = 0.05U$, $\delta w = 0.05U$, $\delta q =$ 0.07 rad/period). We found that convergence was met only for perturbations less than 1%U for the NS aerodynamics. In the flexible wing model, a smaller step size of only 0.25%U was required before perturbation convergence yielded only negligible changes in the system poles.

In the NS model, each disturbance is modeled by moving the wing root with a prescribed motion that corresponds to the desired disturbance for three flapping cycles. During this time, the fluid's response to both the prescribed motion and flapping motion is computed and the surrounded wake is allowed to develop fully. During the fourth and final flapping cycle, the prescribed perturbed motion ceases, the equations of motion are calculated, and the resulting free flight motion is applied at the wing root. To simulate a horizontal or vertical velocity perturbation, the wing root is given a prescribed, steady velocity in the positive x_b or z_b direction. To simulate a rotational velocity, the body CG is rotated, which imparts both translation and rotation at the wing root due to the offset between the body CG and the wing root. Finally, if an initial body angle is required along with an initial rotational velocity, the body angle at the beginning of the NS simulation is set so that the angle is the desired initial angle for the free flight simulation at the end of the third flapping cycle. Figure 3.5 demonstrates how these motions are combined to produce the wing orientation during half of a flapping cycle. The B matrix is obtained by

perturbing each control in a similar fashion and determining its effect on the average system response.

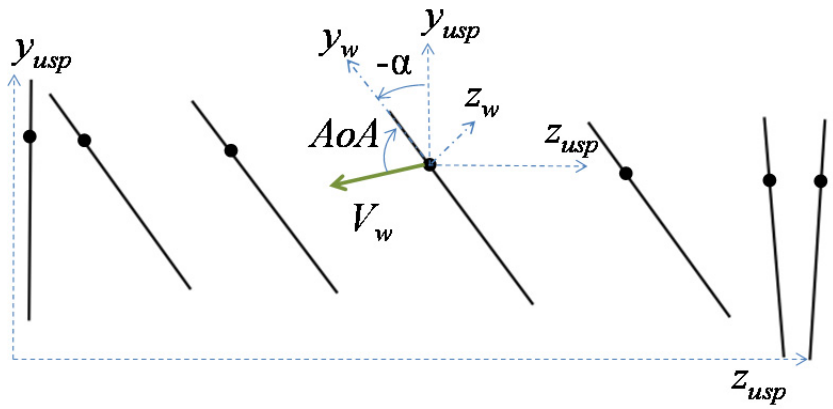

Figure 3.5. Snapshots of wing motion every 1/12th of a period for non-zero initial conditions. The small angular and vertical differences in the wing orientation between start and end of the stroke arise from the body initial conditions *u*, *w*, *q*, and θ, and the stroke plane angle β. The small black dot represents the axis of pitch rotation.

3.6. Modeling Summary

In this chapter, we describe the mathematical and computation model to predict the system dynamics of a FWMAV as well as the tools we use to assess its stability and power requirements. In this model, we address many of the shortcomings identified in previous research, i.e. the averaging of forces, neglecting the wing mass, and not coupling the equations of motion to the aerodynamics, and wing flexibility. Our modeling tightly couples the aerodynamics and the flight dynamics at each time step, we include inertial effects of the wing in our equations of motion and in the calculation of required power, and we do not average the forces across a flapping cycle.

Since this study focuses on longitudinal motion, we assume left-right symmetry and only consider a single wing. The aerodynamic forces are modeled using a two-

dimensional wing section located at 55% span based on the work of Dudley and Ellington [44]. In our multi-fidelity approach, we developed a quasi-steady aerodynamic model based on Sane and Dickinson [27], a rigid wing model based on the incompressible two dimensional NS equations, and a flexible wing model that tightly couples the two dimensional NS equations of fluid motion and Euler Bernoulli beam equations [1]. Since we restrict our analysis to hover, the aerodynamic forces on the body are negligible and are ignored. We directly calculate the wing power based on the time history of the wing motion and the moments required to actuate the wing. All power and stability calculations are made after the FWMAV has achieved trim to ensure that stability results are truly valid and that the flight is achievable.

CHAPTER 4

THE EFFECT OF WING ROTATION AND PITCH AXIS ON THE FLIGHT PERFORMANCE AND STABILITY OF A FWMAV

We first undertake a study of the longitudinal flight dynamics and power requirements for a FWMAV with a rigid wing for several reasons. First, studying rigid wings permits a validation of our model, particularly from the standpoint of longitudinal stability and power. Most studies investigating the stability and power of flapping wing flyers assume rigid wings. Secondly, rigid wing analysis unveils the impact of two unique features of flapping wing flight that directly impact stability and power requirements: wing rotation and wing wake interaction. Finally, rigid wing results serve as a point of comparison for the flexible results that appear in Chapter 5.

There are several ways that the stability and power characteristics of rigid wings can be analyzed. In this chapter, we select a set of kinematic parameters, i.e. the mid-stroke pitch angle, and the timing and duration of wing rotation while keeping other parameters fixed. We then systematically vary the pitch axis of the wing and determine its effect on the required control inputs, forces, power, and stability. Changing the pitch axis is one of the most direct methods of investigating the influence of the wing rotation, permitting an exploration of the physical principles that most affect the power and

stability. We emphasize the importance of conducting all comparisons for a configuration that is in trim to enable equitable comparisons of the required power. Moreover the stability of the system must be analyzed from the equilibrium points.

4.1. Validation of Power and Stability Results

As discussed in Section 2.5, when the power is calculated directly from the wing motion and the resulting moments, the power required takes on both positive and negative values in the course of a single stroke. Virtually all studies neglect negative power [4,32,55,56,58,61,94], although some researchers directly include the negative power in the average (which significantly lowers the mean power). No published studies that report flapping wing power include the negative power as an additive contribution to the required power. Neglecting the negative power assumes that aerodynamic damping assists with the deceleration and that the metabolic cost of performing negative work is much less than an equivalent amount of positive work. It also assumes that energy cannot be stored in the system [55,62]. We term this calculation of power as the positive required power P_{pos}=mean($\forall P(t)>0$), which is the average of all positive power in a single wing stroke. Using this definition, power predictions for fruit flies in the literature are per Table 4.1 along with our prediction based on fruit fly wing kinematics reported in Fry et al. [32]. The power prediction of the present study compares favorably with Sun and Wu [63] (the difference is less than 2%).

We also compare our results with the open loop longitudinal poles reported by both researchers who used QS models [5,8,9] as well as against those who used NS models [15,16,39]. For the quasi-steady studies, the kinematics are matched as closely as possible given the information available in the literature. In all three studies in Figure 4.1

the pitch angle is chosen to be 45°, the duration of pitch rotation is $C_\alpha = 2.1$, and the pitch axis is at the leading edge of the wing. The frequency and flapping amplitude are slightly different in each case, but they are representative of the values needed for a fruit fly to sustain flight. The qualitative response of each simulation is the same and is fully described below. In the NS simulations, we obtain similar qualitative results, although the unstable poles are slightly larger. We plot the fruit fly results alongside the closest insect we could find in the literature, the drone fly, which was studied in two separate studies using an NS solver [25,49]. Since there is no direct comparison of an NS-based stability study in the literature for a fruit fly, we also plot our results for a bumblebee simulation that was performed given the same set up as Sun and Xiong [15]. As in the QS model stability, the open loop poles of the current study compare favorably with those in the literature.

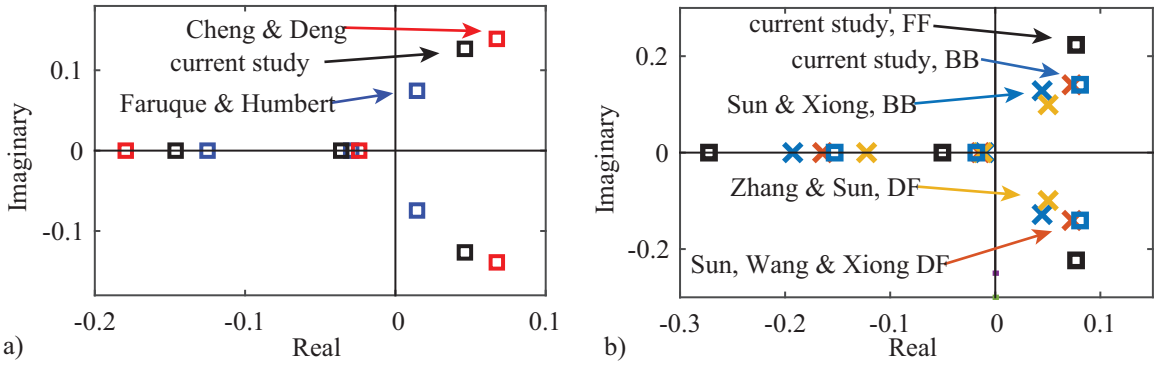

Figure 4.1. Nondimensional open loop poles for the longitudinal dynamics of a fruit fly using the quasi-steady (a) and Navier Stokes (b) aerodynamic models, compared to the values reported in the literature [25,26,29,49]. For (b), the fruit fly (FF) case is designed to mimic the drone fly (DF) set up where $C_\alpha = 2.1$, A = 60° ($AoA \approx 30°$), and $x_p/c = 0.3$ [25,49]; the bumblebee (BB) case set up is identical to that used in Sun and Xiong [15]**.**

Table 4.1. Summary of normalized power of fruit flies reported in the literature.

Study	Insect	P_{pos}, W/kg$_{insect}$	Calculation method
Lehmann & Dickinson 1997 [57]	Fruit fly	18±6	Sum of induced, profile and inertial power
Fry et. al 2005 [32]	Fruit fly	34.5±9	
Wu & Sun 2003 [63]	Fruit fly	29	Directly calculated by 3D NS
Current study	Fruit fly	28.7	Directly calculated by 2D NS

4.2. The Influence of the Pitch Axis Location, x_p/c

Before presenting the results of varying the pitch axis, we discuss the other kinematic parameters that we selected for the rigid wing study. First, we chose a pitching amplitude of A = 50°. This pitch angle results in an angle of attack of approximately 40° during the translational phases of the stroke, and the maximum lift predicted by Sane and Dickinson based on their experiments was between 40° and 50° [26]. Finally, a parametric study of our own indicated that $\alpha = 50°$ provided one of the lowest values of required power across a range of other kinematic parameters. We also chose a square wave smoothing parameter of $C_\alpha = 4.1$. This results in a relatively sharp square wave, with the pitch rotation occuring in approximately 10% of the stroke**.** Similar kinematics are used in several studies by Sun and coworkers [15,17,18]. Additiontally, higher rotation rates yield higher rotational forces, so using a brief duration of wing rotation helps to highlight the role of wing rotation. Finally, we selected advanced rotation with $\alpha_\varphi = 0.3$. We chose advanced rotation for this study specifically because Dickinson and coworkers showed that advanced rotation yields more lift for rigid wings than symmetric or delayed rotation. The time course of flapping and pitch angles are per Figure 4.2, with the flapping angles resulting from the requirement to establish free-flight equilibrium.

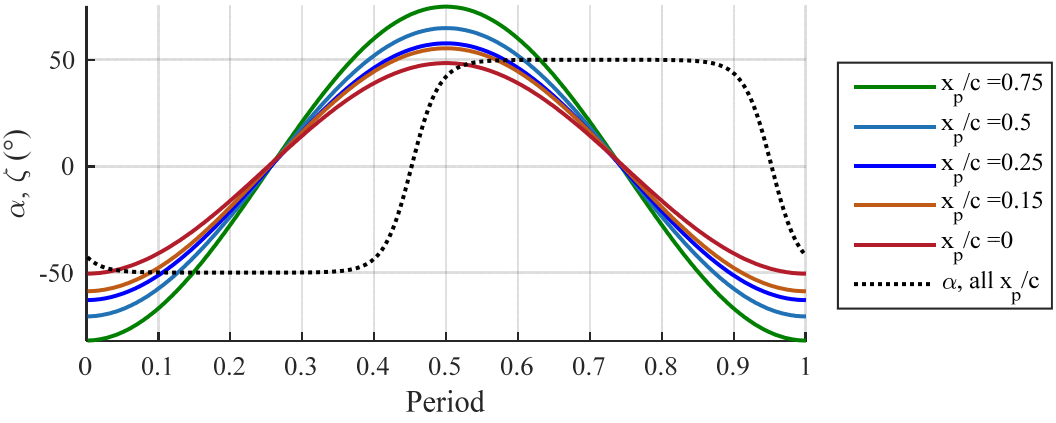

Figure 4.2. Wing flap angles (solid) and pitch angles (dotted) for various values of x_p/c with A = 50°, α_φ = 0.3, C_α = 4.1.

In spite of the many insect morphological parameters reported in the literature, the pitch axis location of insects is under reported, in part because it is difficult to determine [27]. That said, Ennos [50] reports that the torsional axis for *Diptera* that he studied is located at 15% chord, which is also used by Bergou and Wang [37] in their study based on dragonfly wings. Sun and Du [51] utilize 30% chord in their analysis of fruit flies. Bush and Bader vary their pitch axis from 20% to 45% chord [52]. Taha et al. [5] vary their hinge axis from 0.1 to 0.9 chords.

4.3. Control Inputs, Kinematics, and Aerodynamic Forces

We vary the pitch axis location x_p/c from the leading edge to 75% of the chord length and determine its influence on the required wing kinematics to achieve trim and the resulting forces, power, and stability consequences. From Section 3.3.1, changing the axis of rotation directly affects the amount of rotational lift and drag that is produced as well as having an influence on the added mass force. Thus, QS-based studies that do not

include these terms [5,8,9,77] will be less sensitive to these aspects of changing axis of pitch location. Further, from the parallel axis theorem, changing the pitch axis also changes the wing pitch inertia, and the wing product of inertia, I_{xy}. Studies that omit wing inertia will also be less sensitive to these effects. Since this study uses a QS model that includes the rotational lift, added mass, and wing inertia, the pitch axis location has a significant effect on required control inputs for hovering and associated power, as well as a smaller effect on stability. We also adjust the vertical offset as we change the axis of pitch rotation to maintain a constant distance between the body CG and the quarterchord of the wing.

Although changing the pitch axis does not directly manipulate the wing kinematics, it significantly affects the required flapping amplitude needed for trim, which must vary from 99° to 157° as seen in Figure 4.3. Its effect on the stroke plane angle and flapping offset angle is smaller, but noticeable. The reason for the large difference in flapping angles for the NS prediction as x_p/c is changed as can be seen in Figure 4.4, where the horizontal and vertical force histories are plotted. First, the large force spikes associated with advanced rotation are noticeable near $\tau = 0.4$ to 0.5 and 0.9 to 1.0. This small region with a large increase in lift and drag results from the rotational forces discussed in Section 3.3.1. In advanced rotation, the forces generated during wing rotation are enhanced by the fact that the wing's flapping velocity and rotational motion combine to produce a higher velocity at the aerodynamic center near stroke reversal. Both the QS and NS models predict this rotational lift. The modified rotational force coefficient (detailed in the Appendix) that we utilize in the QS model allows the QS model to predict this region of lift more accurately than the theoretical lift coefficient.

Additionally, the large force spikes immediately following course reversal are present due to the effects of added mass and wing wake interaction. As the wing accelerates into the next half-stroke, added mass forces are generated. They can be seen in the plot of the QS model's force prediction in Figure 4.4 near $\tau = 0.5$. At the same moment, the wing experiences wing wake interaction, which the QS model cannot predict. From Figure 4.4, the magnitude of the forces from wing wake interaction are much larger than from added mass.

Immediately following course reversal ($\tau = 0$ and 0.5) there is a large increase in the vertical force as the wing interacts with the leading edge vortex shed in the previous stroke. This interaction results in both upwash and momentum transfer from the fluid to the wing. However, the wing wake interaction also causes a "wake valley" near $\tau = 0.1$ (and 0.6). The vortices shed in the previous strokes form a vortex street, inducing a downwash. As the wing travels through the downwash, the effective angle of attack is reduced, lowering the instantaneous lift [31]. The translational lift associated with delayed stall develops in the interval between the wake valley and the rotational lift spike at the end of the half stroke. This unsteady lift enhancing mechanism results from the formation of an attached leading edge vortex through a significant portion of the stroke while the pitch angle is held constant [22].

The size of the force spikes from both rotational lift and wing wake interaction is directly related to the pitch axis location. When the axis of rotation is at or near the leading edge, these effects are large; when the axis of rotation is at or behind the mid-chord, these effects are small and even reversed. In order to achieve trim, the flapping amplitude is adjusted accordingly. This change in flapping amplitude is also reflected in

Figure 4.4(b), where the amount of translational lift from $\tau = 0.15$ to 0.35 and from $\tau =$ 0.65 to 0.85 is much larger for pitch axes located at or behind the quarterchord.

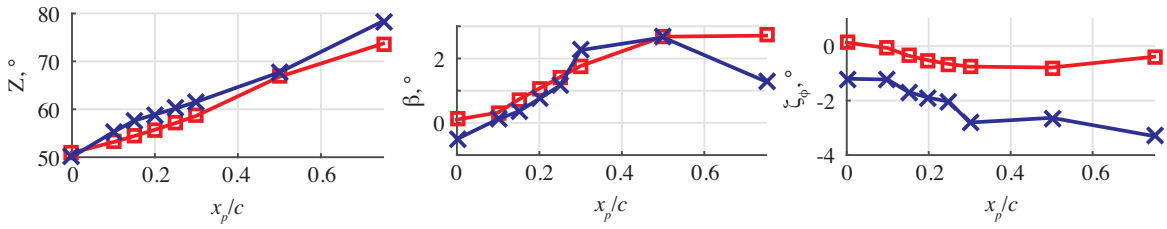

Figure 4.3. Required control inputs to achieve trimmed hovering flight for various values of x_p/c with A = 50°, α_φ = 0.3, C_a = 4.1 for both QS (□) and NS (×) aerodynamic models.

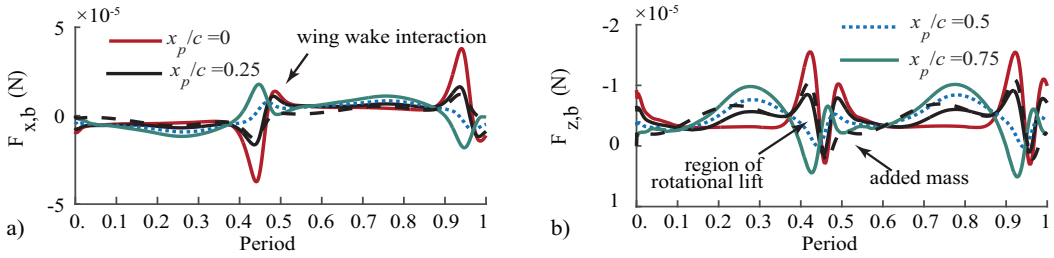

Figure 4.4. Horizontal (a) and vertical (b) force histories for various values of pitch axis location. The solid and dotted lines are from the NS solution; the dashed line is from the QS solution with x_p/c = 0.25. Case set up is the same as Figure 4.3. Negative values of $F_{z,b}$ correspond to positive lift.

Although the rotational force can add significant lift, it also increases the drag (Figure 4.4), and its overall effects on the power required and stability of the vehicle are not clear. The rotational lift coefficient is directly changed by changing the pitch axis, while maintaining the same timing and duration, and magnitude of the pitch angle during wing translation. Alternatively, the rotational lift can be varied by changing the duration of wing rotation or the pitch amplitude. However, both of these have an even larger effect on the translational lift because they either change the amount of time that a given pitch

angle is held or they directly change the pitch angle during the translational phase, which obscures the effects of rotational lift. Because the rotational lift significantly affects the force histories as shown in Figure 4.4, its contribution has a direct influence on the power required and the stability of the vehicle, primarily due to the large changes in the required control inputs that are realized when rotational lift is considered.

4.4. Power Impacts Due to Variation in Pitch Axis, x_p/c

Figure 4.5 shows the variation in positive flapping, pitching, and total power with respect to x_p/c. There is a tradeoff between pitch and flap power that is explored in more detail in Section 4.1. The pitching power decreases as the pitch axis moves toward the quarter chord and takes a minimum value at x_p/c =0.3. The flapping power shows less sensitivity to pitch axis for x_p/c forward of the quarter chord. Thus, the minimum overall power for this setup (with advanced rotation) occurs at x_p/c = 0.3 where the total power required is 16.9 W/kg. In spite of the significant pitch power contribution that arises, using wing motion with advanced rotation required less overall power than the validation cases that use symmetric or biological kinematics. A primary reason is that the flapping power is significantly larger than the pitch power for all $x_p/c \geq 0.1$.

To illustrate the power tradeoffs associated with changing the pitch axis and by extension the influence of rotational lift, we plot the time histories of power in Figure 4.6 based on the NS solution. The flapping power profiles change dramatically as x_p/c is moved toward the trailing edge. For flapping power, the initial peak that occurs during the first half of each half stroke (i.e. from τ = 0 to 0.25 and 0.5 to 0.75) is the power associated with overcoming the wing inertia and fluid forces in order to attain a sinusoidal flapping profile. As flapping amplitude increases, so does this peak due to both

inertial and aerodynamic contributions. The secondary peak in each half-stroke is notable because this peak can be positive or negative.

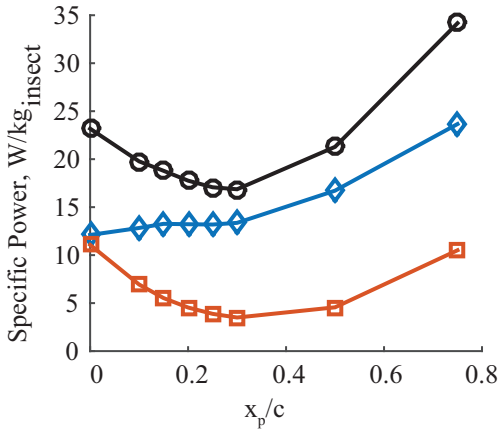

Figure 4.5. Positive total (○), flap (◊), and pitch (□) power required to achieve hover for different values of x_p/c, assuming A = 50°, α_φ = 0.3, C_α = 4.1.

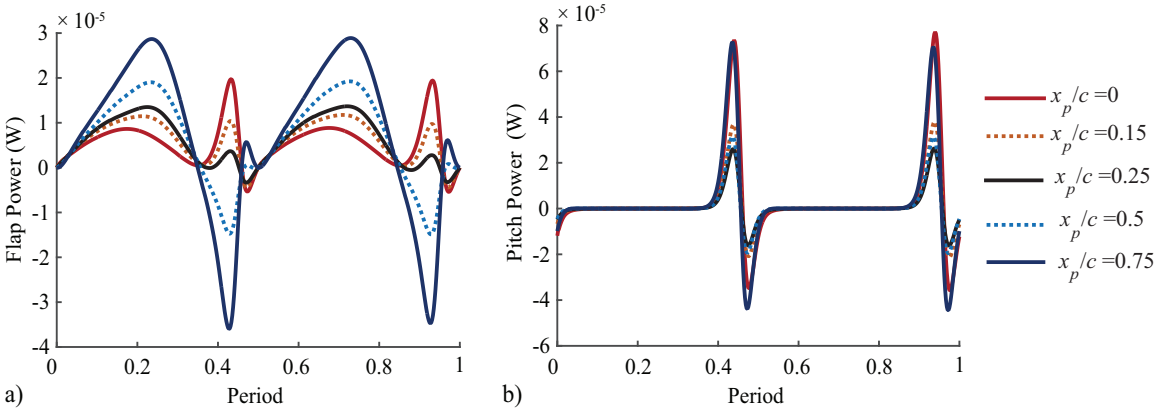

Figure 4.6. Time histories of (a) flapping power and (b) pitching power based on the NS equations for various values of x_p/c with A = 50°, α_φ = 0.3, C_α = 4.1.

To investigate the source of this secondary peak, we show the QS and NS prediction of the flapping power for two pitch axes in Figure 4.7: $x_p/c = 0.1$ for Figure 4.7(a) and $x_p/c = 0.3$ for Figure 4.7(b). For advanced rotation with $x_p/c = 0.1$, both the inertial and aerodynamic forces cause a spike in the power during the advanced rotational

phase. In order to achieve advanced rotation, the rotation causes a forward velocity on the part of the wing below the pitch axis location, which adds to the translational velocity. The increased magnitude of the freestream seen by the wing yields a higher power requirement. However, the inertial contributions are also significant, particularly since the nature of the inertial contributions (positive vs. negative) during advanced rotation depends on the pitch axis location.

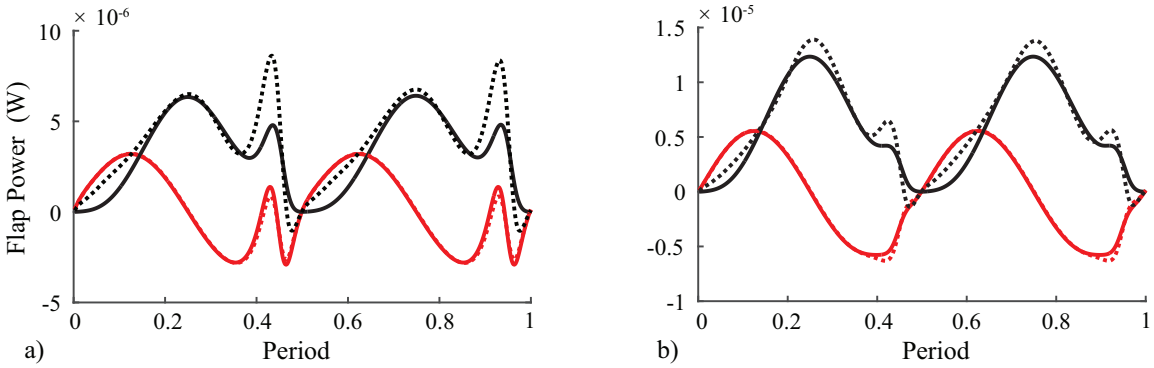

Figure 4.7. Comparison of the relative contribution of the aerodynamic (black) and inertial (red) forces to the flapping power for (a) x_p/c = 0.15 and (b) x_p/c = 0.3 from both the NS (dotted) and QS (solid) aerodynamic models. Other details are per Figure 4.5.

The inertial contribution itself consists of three parts. The first term in equation (3.41) contains two components that affect the flapping power $({}_w\underline{I}_{wo}\,{}_w\boldsymbol{\omega}_w)\cdot\mathbf{k}_{sp} = I_{yy}\ddot{\zeta} + I_{xy}\ddot{\alpha}$ Even though the value of I_{xy} is an order of magnitude smaller than I_{yy}, it increases when the pitch axis is far away from the chordwise location of the wing center of mass, i.e. the quarterchord. Additionally, for rapid advanced rotations, the angular acceleration $\ddot{\alpha}$ about the pitch axis can be quite large, such that the product of inertia term (I_{xy}) affects the flapping power due to the required pitch accelerations. As pointed out by Whitney and Wood [43], this product of inertia is the term that can cause passive wing

pitch rotation under the right kinematics, but when advanced rotation is required, it increases the flapping power required. The third contributor in the inertial power is from the second term of equation (3.41), ${}_w\boldsymbol{\omega}_w \times {}_w\underline{I}_{wo}\, {}_w\boldsymbol{\omega}_w$, which though small, is also additive when $x_p/c = 0$ to 0.3. The values for the key elements of the inertia matrix relative to this discussion are provided in Table 4.2. Note that when the pitch axis changes from its nominal value at the quarterchord to 0.1, the flapping inertia (I_{yy}) remains the same, but the product of inertia (I_{xy}) increases by a factor of 7.5.

Table 4.2. Changes in the moment of inertia due to different pitch axis locations.

	$x_p/c = 0.10$	$x_p/c = 0.25$	$x_p/c = 0.3$
I_{xx}	2.05×10^{-16}	1.57×10^{-16}	1.63×10^{-16}
I_{xy}	3.94×10^{-16}	5.24×10^{-17}	-6.13×10^{-17}
I_{yy}	3.61×10^{-15}	3.61×10^{-15}	3.61×10^{-15}

The situation is quite different in the case of $x_p/c = 0.3$. Here the product of inertia starts to become negative as the wing center of mass is now in front of the pitch axis. The effect of this change can be seen in Figure 4.7(b) as a small deviation in the inertial power from a sinusoidal waveform. Furthermore, when $x_p/c = 0.3$, the speed of quarterchord is now reduced due to advanced rotation because of its relative position in front of the pitch axis. This also accounts for the similarity between the QS and NS predictions for $x_p/c = 0.3$.

The secondary power peak in Figure 4.7(a) during wing deceleration also explains why flapping power grows at a different rate from flapping amplitude. When the pitch axis varies from the leading edge to the quarter chord, the required flapping amplitude grows by 20%, but the flapping power only grows by 12%, because there is a positive

power contribution for $x_p/c \leq 0.3$. In contrast, when the pitch axis varies from the quarter chord to the midchord, the flapping power grows at a faster rate than the flapping amplitude because the secondary power peak is negative.

4.5. Stability Impacts Due to Variation in Pitch Axis, x_p/c

In addition to affecting the power, the pitch axis location can also affect the stability and the speed of the response to external perturbations. Figure 4.8 illustrates the changes in the open loop poles with respect to x_p/c for both the QS and NS model. The unstable poles of the QS solution show little variation until $x_p/c > 0.3$, where they become more stable for reasons outlined in Taha et al. [5]. In short, at these more extreme pitch axes, the stabilizing effect of the pitch rate damping dominates the pole, although in our simulations, its effects are ameliorated by the large growth in flapping amplitude. The NS solver predicts the reverse trend, however, for reasons that are detailed in Section 4.5.1.

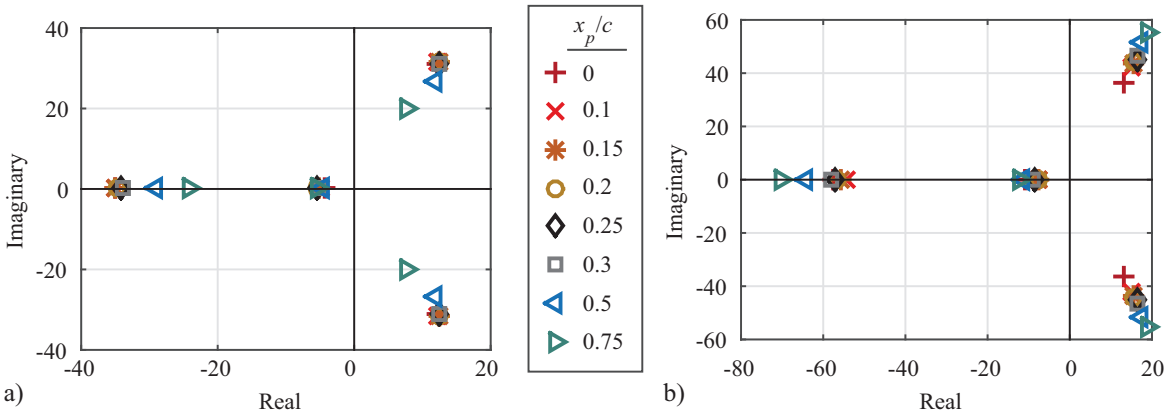

Figure 4.8. The variation in longitudinal open loop poles with respect to x_p/c based on the QS (a) and the NS (b) solutions. The units of both axes are 1/seconds.

An expanded treatment of analyzing the stability via open loop poles is provided in Chapter 2, but we include a short summary here as well. The system poles are the

eigenvalues, $\lambda_n = \sigma_n \pm \omega_n i$, $n = 1\ldots4$, of the linearized system matrix, where the real part of the pole, σ_n, corresponds to the rate of growth or decay of the response, and the imaginary part, ω_n, corresponds to the natural frequency of any oscillatory motion. The rate of growth of the unstable poles can be converted to doubling time, $t_{double}=\ln(2)/\sigma_n$, and the natural frequency can be used to determine the period of oscillation per $T_n = 2\pi/\omega$. A pole is unstable when $\sigma_n > 0$.

Table 4.3. Unstable eigenvalues, double times and ratio of the period of motion for QS and NS solutions about trimmed equilibrium.

	$\lambda_{1,2}$ in 1/seconds		t_{double}/T_{flap}		T_{body}/T_{flap}	
x_p/c	QS	NS	QS	NS	QS	NS
0	11.12 ± 26.23i	13.99 ± 36.37i	13.59	10.80	123.15	97.91
0.1	10.98 ± 26.55i	14.97 ± 42.06i	13.76	10.09	124.71	91.50
0.15	10.93 ± 26.57i	15.76 ± 43.26i	13.82	9.59	125.28	86.91
0.2	10.81 ± 26.54i	15.89 ± 44.46i	13.98	9.51	126.75	86.19
0.25	10.66 ± 26.46i	16.55 ± 45.50i	14.18	9.13	128.52	82.76
0.3	10.51 ± 26.33i	16.52 ± 46.57i	14.38	9.15	130.33	82.90
0.5	9.80 ± 24.82i	17.42 ± 51.25i	15.42	8.67	139.77	78.63
0.75	7.46 ± 19.50i	18.85 ± 55.59i	20.25	8.02	183.56	72.66

Table 4.3 lists the unstable eigenvalue pairs, doubling times, and the period of oscillation in terms of the flapping period for the NS and QS solutions. The doubling times for the QS model are generally higher than their NS counterparts, suggesting that the system driven by the NS solution is more unstable. The comparison of the period of motion shows that the ratio of the period of body motion to the wing flapping frequency is $O(10^2)$, which is due in part to the high flapping frequency of the fruit fly. An

important implication of this ratio being high is that it permits the first order averaging to accurately represent the dynamics of the system per the findings of Taha et al. [77].

4.5.1. Stability Derivatives and Their Physical Underpinnings

In order to assess the reasons for the change in the poles with respect to the changes in x_p/c, we analyze the effect of x_p/c on the stability derivatives themselves (Figure 4.9), which capture the net acceleration due to a perturbation in each degree of freedom. For example, X_u is the net acceleration in the x_{body} direction with respect to a velocity perturbation u. The first observation is that Z_u, X_w, X_q, and Z_q are very small and are also insensitive to changes in the pitch axis. This is a common finding in the literature [15,39], and furthermore several researchers neglect these derivatives altogether for analytical reasons [5,8]. Additionally, given the structure of the system matrix, even large changes in M_w do not affect the poles of the system. The vertical damping is governed by Z_w which governs the heave dynamics associated with the small negative pole. This mode is stable.

The remaining three stability derivatives of interest, X_u, M_u and M_q, are coupled and lead to the unstable oscillatory mode, which we analyze in the following sections. Both the QS and NS solutions predict a negative X_u, indicating there is velocity damping in that degree of freedom, but it is insensitive to x_p/c. Therefore the changes in stability seen in Figure 4.9 must arise from changes to M_u and M_q.

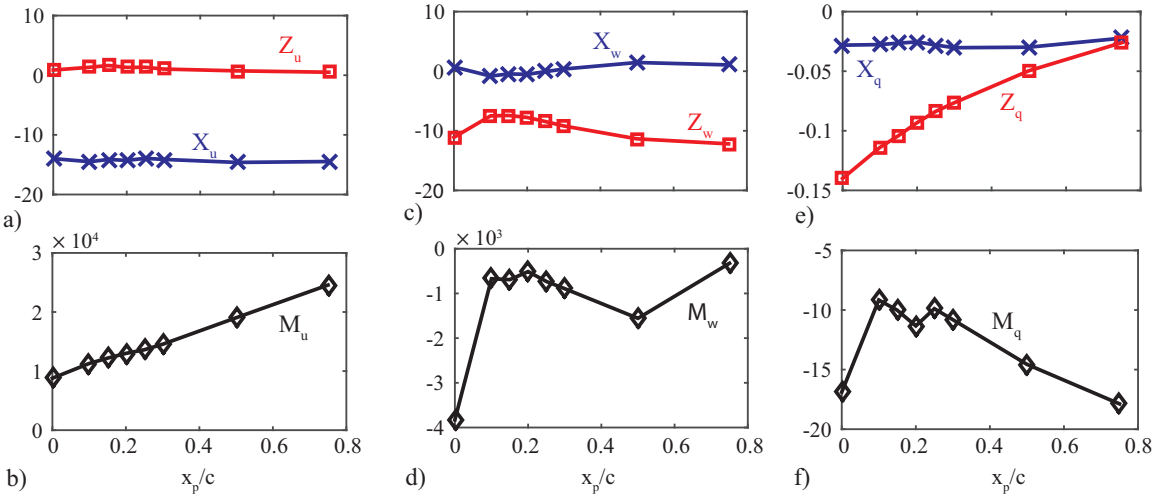

Figure 4.9. Stability derivatives vs. variation in x_p/c based on the NS solution to the aerodynamics. The units associated with X_u, Z_u, X_w, Z_w, and M_q are 1/s; the units of M_u and M_w are 1/(m-s); the units of W_q and Z_q are m/s.

4.5.2. The Speed Derivative, M_u, and the Effect of Wing Wake Interaction.

There are three sources of speed derivative M_u, which produces a nose up moment in the presence of a horizontal velocity perturbation. These sources can be explained by referring to the force histories in Figure 4.10. The changes in drag due to a horizontal perturbation acting above the body CG causes a pitch up moment because there is more drag during the ventral stroke and less drag in the dorsal stroke causing a net nose up moment [15] as seen in Figure 4.10(a) at B and F. The rotational force magnitudes in the oncoming flow (at C) are higher than for the hover case, and they are lower than the hover case in the opposite half stroke (at G), consistent with the results by Cheng and Deng [8].

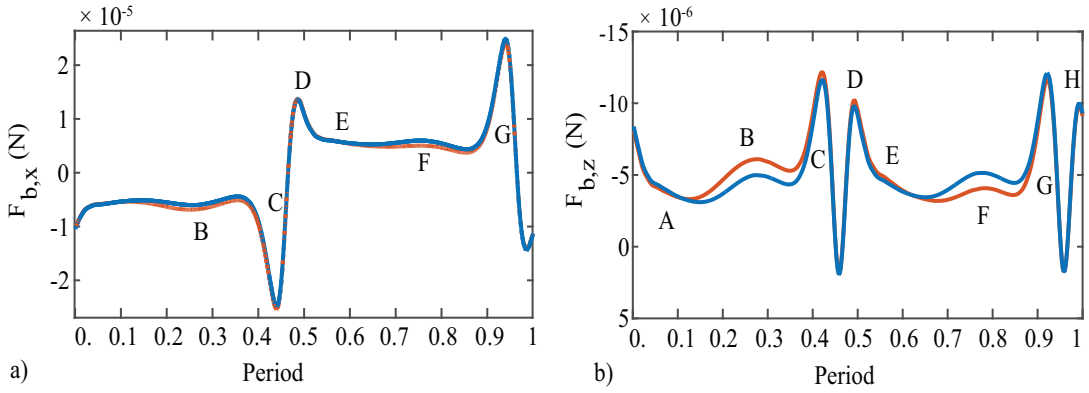

Figure 4.10. Horizontal (a) and vertical (b) force histories for x_p/c = 0.15 at hover (blue) and under a longitudinal velocity perturbation (red) of $u = 0.032U$.

However, wing wake interaction also affects the speed derivative due to changes in force production at A, D, E, and H in Figure 4.10. In particular, the larger lift that is seen due to the increased oncoming flow between $\tau = 0.2$ and 0.38 (B) generates a stronger leading edge vortex (LEV) than in hover (where the relative fluid velocity is lower). This vortex then interacts with the wing from $\tau = 0.5$ to 0.65 (D-E), enhancing lift relative to the hover case. In the other half stroke, the opposite effect is seen. The lower fluid velocity in the dorsal stroke creates a weaker LEV and therefore less lift from $\tau = 0.65$ to 0.88 (F). This weaker LEV then interacts with the wing from $\tau = 0$ to 0.15 (H, A), but its lift enhancing effects are lower than the hover case (without a gust).

Figure 4.11 shows how the body motion changes the LEV strength and the associated downwash for $\tau = 1.0$ and $\tau = 0.08$. As the wing translates from right to left, it encounters these vortices and the associated upwash and downwash. In particular, Figure 4.11(a,c) shows the wing wake interaction at $\tau = 1.0$ which produces the prominent force peak that is seen at H in Figure 4.10(b). The vortices also impart an upwash on the wing at this portion of the stroke, but it is clear that the benefits of the upwash (specifically

momentum transfer to the wing and enhanced effective angle of attack) are stronger in the hovering case (left) than in the perturbation case (right).

Figure 4.11(b,d) demonstrates how these changes continue through the first part of the ventral stroke. The size and position of the vortices in Figure 4.11(b) can be seen, and the corresponding changes in the upwash and downwash in the flow are also evident in Figure 4.11(d) for hovering and the perturbation case. Once again, these differences in the wake account for the force differences seen in A and E of Figure 4.10, which cause the magnitude of the speed derivative M_u to increase.

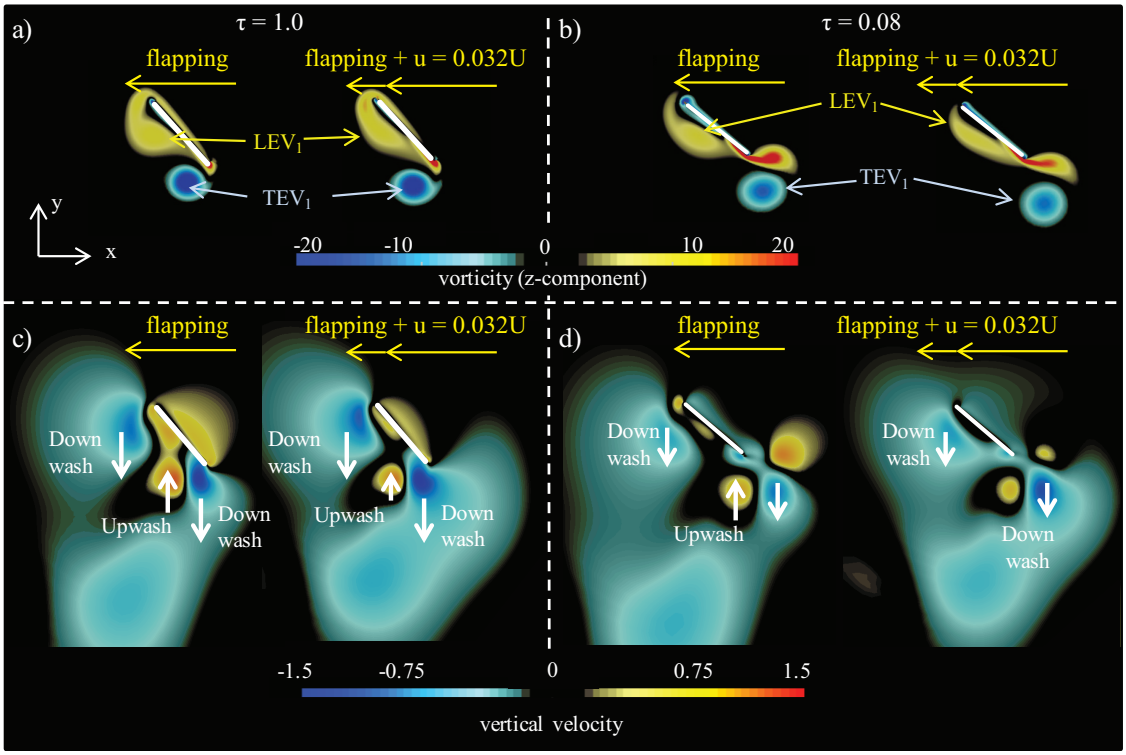

Figure 4.11. Plots of (a,b) vorticity and (c,d) vertical velocity for the flapping wing for τ = 1.0 at course reversal from the dorsal to ventral stroke for the case at (a,c) hovering and for τ = 0.08 (b,d). Each subplot shows relative velocity due to flapping on the left and due to flapping with a velocity perturbation in the *x*-direction, $u = 0.032U$, on the right. LEV_1 and TEV_1 depict the leading edge and trailing edge vortices shed during the previous stroke. Vorticity is nondimensionalized by U/c; vertical velocity is in chords/period.

Previous studies acknowledged that the lift in the ventral stroke would be enhanced by an oncoming gust and in the dorsal stroke, lift would be reduced. They either assumed or attempted to show that these changes in lift produced negligible moment or change in average lift. Because these changes in vortex dynamics occur in opposing quarter strokes (i.e. the 1st and 3rd quarters), they reinforce each other vice cancel out, as depicted in Figure 4.12.

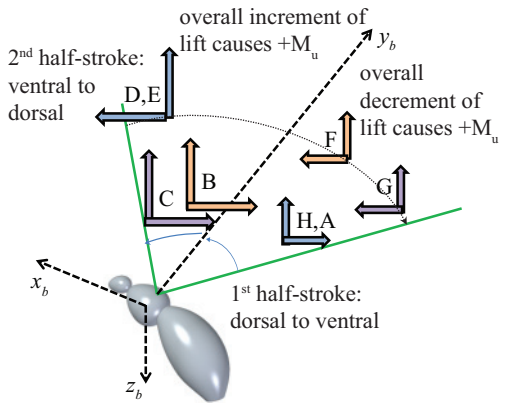

Figure 4.12. The location and relative magnitude of lift and drag forces due to translational forces (orange arrows at B and F), rotational forces (violet arrows at C and G), and wing wake interaction (blue arrows at D, E, H, A).

4.5.3. The Effect of x_p/c on M_u

Thus far, we have explained why the NS stability derivatives are larger than the QS, and in so doing, we have identified a previously unreported source of instability arising from the effects of wing wake interaction. Now we turn to assess the influence of changing the pitch axis location on the stability derivatives, particularly M_u and M_q.

The primary mechanism for the changes in the stability derivatives and open loop poles is the change in the flapping amplitude and its effect on the increment or decrement

to the translational lift. As shall be demonstrated, this directly affects the horizontal velocity damping X_u, the speed derivative M_u, and the pitch rate damping M_q.

The effect on M_u, is the most significant contributor to the stability. Figure 4.13 shows the horizontal and vertical force histories and (total) moment histories for two values of x_p/c: 0.15 and 0.5 with and without a gust. Large moments about the body CG are generated during wing rotation for both values of x_p/c. The change in moment due to a horizontal perturbation M_u for $x_p/c = 0.5$ is approximately five times the magnitude as $x_p/c = 0.15$. Additionally, the change in the moment during wing rotation is a very small contributor to the total. The main reason is that the lift generated by the wing rotation is a function of U, whereas the translational lift is a function of U^2. Additionally, the component of a horizontal gust that affects U is a function of $\cos(\zeta)$. Since rotational forces are generated at stroke reversal when ζ is large, the relative magnitude of the gust is significantly diminished. For both reasons, horizontal velocity perturbations increase the translational force more than the rotational force. Therefore, the primary reason for the increase in M_u with respect to increasing x_p/c is the corresponding increase in flapping amplitude, and its effect of amplifying the moment produced due to a horizontal gust.

4.5.4. The Effect of x_p/c on M_q.

The next important stability derivative is the pitch-rate damping, M_q. The pitch rate affects a number of aerodynamic features on the wing. Due to the vertical offset above the CG, a pitch rate imparts a linear velocity to the wing that is additive in the dorsal stroke and subtracts slightly from the translational velocity in the ventral stroke.

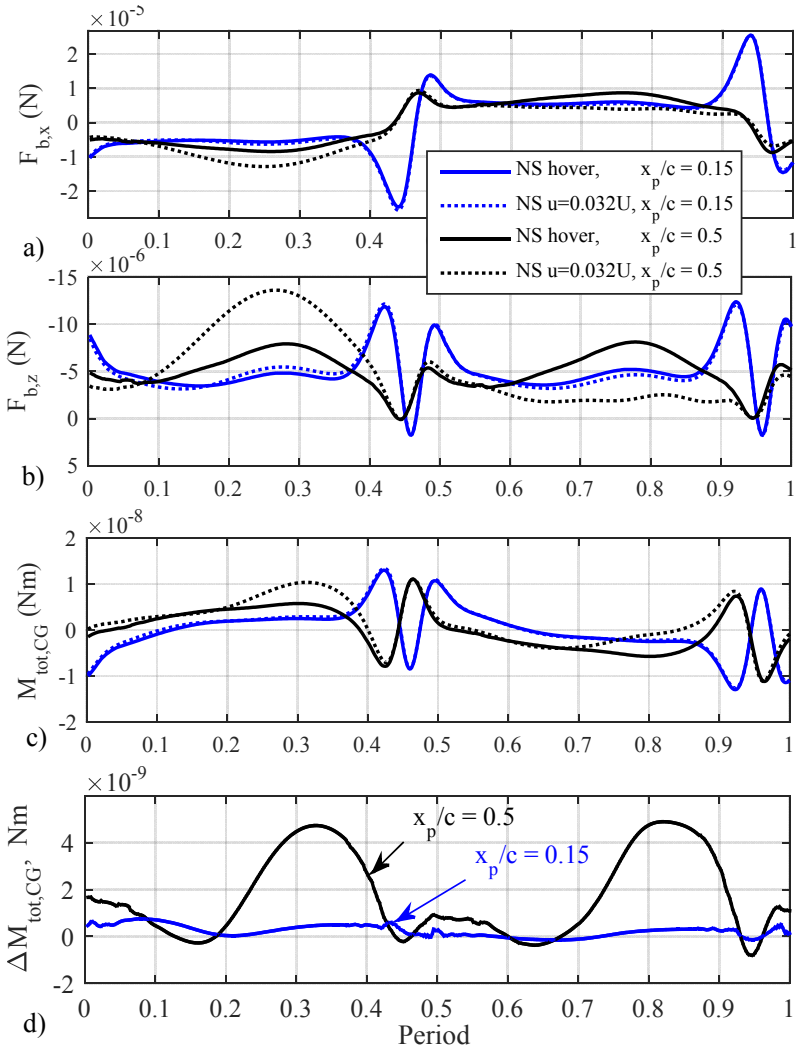

Figure 4.13. The horizontal (a) and vertical (b) force histories, the moment history (c), and the change in total moment (d) for x_p/c = 0.15 (blue) and 0.5 (black) with (dotted) and without a gust (solid). Other details remain the same as Figure 4.10.

Additionally, the vertical component of velocity changes the effective angle of attack. In the first and third quarters of the stroke motion, the effective angle of attack is slightly higher than at the mid stroke, and in the second and fourth quarters, the angle is slightly lower. Finally, the constant pitch rate itself creates lift in the ventral stroke and subtracts from lift in the dorsal stroke. Although each of these effects is small when considered individually, their combined effects result in significant moment changes

from the hover case alone, as is depicted in Figure 4.14. As x_p/c increases, the flapping amplitude also increases, which amplifies the effects of the pitch rate and causes an increased moment-sensitivity to the pitch rate.

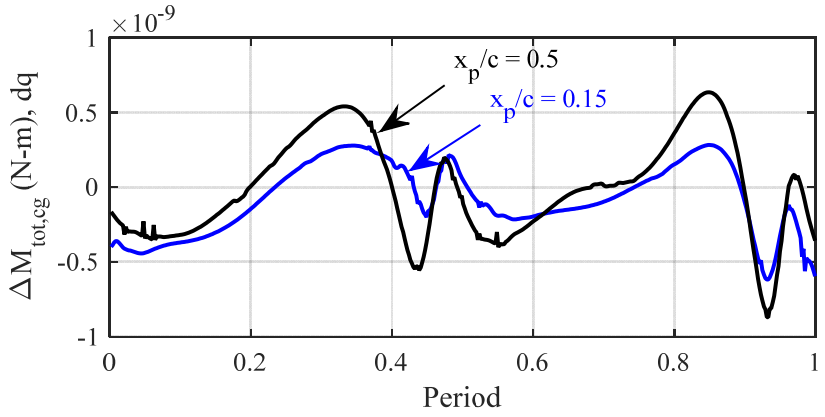

Figure 4.14. The change in total moment about the CG when under a pitch rate perturbation of q = 0.07 radians/period for two values of x_p/c. Other details remain the same as Figure 4.5.

As M_q increases, it stabilizes both the short period mode as well as the unstable oscillatory mode. However, M_q only grows by approximately 60% throughout the range of x_p/c whereas the M_u grows by a factor of 2.5 across the range of x_p/c, so the changes in M_u dominate the behavior of the poles in Figure 4.8.

4.6. Rigid Wing Summary

The rigid wing analysis permitted the validation of our QS model and the validation of the power and stability predictions of the coupled NS-flight simulator of the equations of motion. By changing the pitch axis of the wing, we highlighted the large effect that wing rotation has on the trim inputs, forces, and power requirements of a FWMAV. Moving the pitch axis toward the leading edge increases the magnitude of the

rotational force, which contributes significantly to the total lift. Increasing the contribution of the rotational forces simultaneously decreases the flapping amplitude and required flapping power and increases the required pitching power, although flapping power dominates the pitch power for all pitch axis locations aft of the leading edge. The tradeoff between pitch power and flapping power results in a minimum power of 16.9 W/kg that occurs when the pitch axis was between $x_p/c = 0.25$ and 0.3, which is the same pitch axis used in analysis of insects by [15,59]. Accurately modeling wing rotation also affects the stability predictions. Including wing rotational effects results in smaller required flapping amplitudes, which yield a smaller speed derivative M_u and more stable poles. This is because smaller flapping amplitudes require less translational lift, and the translational forces contribute more to destabilizing the FWMAV by increasing M_u than the rotational lift. These findings cast doubt on those flight dynamics and power optimization studies [5,8,9,119] which explicitly neglect wing rotation and rotational lift effects.

Finally, the rigid wing analysis demonstrated that wing wake interaction also significantly affects the power and stability of the FWMAV. Wing wake interaction modifies the lift and drag history of the FWMAV by creating lift peaks and valleys that are not modeled in the QS framework. Including wing wake interaction in the model predicts a net decrement of lift, and therefore requires larger flapping amplitudes, which directly impacts the power and stability. Furthermore, we show that wing wake interaction increases the speed derivative, M_u, which increases the instability relative the QS model and those studies who do not model wake effects [5,8,9,11,77]. Properly

modeling the aerodynamics therefore, is critical in accurately predicting the flight performance and stability of insects and FWMAVs.

CHAPTER 5

THE EFFECT OF FLEXIBILITY ON THE PERFORMANCE AND STABILITY OF A FWMAV

In the course of studying the effect of various kinematic and design parameters on the stability and power requirements for rigid wings, we have learned several important lessons as discussed in Chapter 4. The contribution of rotational lift plays a large role in determining the power and stability characteristics of an insect or FWMAV. Ignoring the rotational lift contribution can lead to an inaccurate assessment - usually an under prediction - of the lift produced and, therefore, inaccurate control inputs and force histories. The contribution of wing wake interaction also plays a large role in determining the power and stability characteristics. Wing wake interaction can increase the growth rate of the unstable response, destabilizing insects and FWMAVs with rigid wings.

Insects are known to have flexible wings [19,20,45,120,121]. It is desirable, therefore, to establish what advantages or disadvantages wing flexibility might confer on insect locomotion and flight performance of FWMAVs. From the standpoint of design, it is also important to establish the impact of varying wing stiffness on the stability and power consumption. It is more difficult to make a rigid flapping wing at this small scale.

Furthermore, if passive pitching can be achieved through wing flexibility that still permits hovering flight, active pitch actuation mechanisms can be eliminated from the design, saving weight and reducing complexity. Finally, review papers published in the last five years [6,7,10,87] all point to the lack of any published work on wing flexibility as a significant shortcoming in the state of knowledge concerning insect and FWMAV flight performance and flight dynamics.

5.1. Variation in Wing Flexibility

We model the wing as a linear beam with a constant thickness and constant material properties (i.e. density and stiffness) along its chord length. The wing section is taken at the spanwise location of the center of the second moment of wing area, which is the wing station whose lift and drag production are representative of the aerodynamic forces generated by the entire wing. This two-dimensional assumption means that no spanwise variation in wing deformation is considered.

As described in Section 3.3.4, the dynamics of the fluid structure interaction (FSI) of flexible wings moving rapidly in a fluid can be characterized by several additional important nondimensional parameters [12]. These parameters are themselves functions of the thickness ratio, the density ratio, and the frequency ratio. We maintain the same thickness ratio that we utilized for rigid wing studies of $h_s^* = h_s/c = 1.5\times10^{-3}$ based on fruit fly wings given in Lehmann and Dickinson [57]. The density ratio $\rho^* = \rho_w/\rho$ is the ratio of the wing material density to the fluid density. Since this study focuses on insect wings moving in air, we maintain a constant density ratio of $\rho^* = 1000$, based on the measured values of live insects reported in [20,121]. The frequency ratio f/f_1 is the ratio of the flapping frequency to the first natural frequency of the wing based on its size and

material properties. If the flapping frequency is held constant, as it is in the present study (f = 218 Hz for fruit fly analysis), lower frequency ratios correspond to stiffer wings. All known insect wings have frequency ratios $f/f_1 \leq 0.8$ [121], indicating that insects flap their wings below their first natural resonant frequency. Sunada et al. [114] report that dragonfly wings operate at frequency ratios of $f/f_1 = 0.3$ to 0.45. The frequency ratios investigated in this study range from $f/f_1 = 0.288$ to 0.461, with intermediate values and associated stiffness listed in Table 5.1. This range was set by the computational model and our ability to determine equilibrium. For very flexible wings with $f/f_1 > 0.46$, the wing flexibility was too large for the linear beam model employed in our FSI solver. For very stiff wings ($f/f_1 < 0.35$), we were not able to find control inputs that allowed the vehicle to reach equilibrium in hover without unacceptably high residual accelerations on the order of 10% gravitational acceleration. The main reason is that we do not impose any active pitch. Although this might appear to be a narrow range of testing the wing flexibility, this range includes both the f/f_1 of live insects as well as the f/f_1 found to be the most efficient for lift production as reported in Sridhar and Kang [13].

The same control inputs used with the rigid wings in Chapter 4 are used here: the flapping amplitude Z, the stroke plane angle β, and the flapping offset angle, ζ_φ. The fact these inputs can be used for flexible wing configurations motivated their use vice the control inputs used by Sun and coworkers [15,40] to balance their forces. As in rigid cases, the flapping amplitude is used primarily to balance the weight and vertical force. The stroke plane angle and flapping offset angle are both used in tandem to balance horizontal forces and the pitching moment. Using the trim algorithm presented in Section 3.5.2, we determined the control inputs for the flexible wing depicted in Figure 5.1.

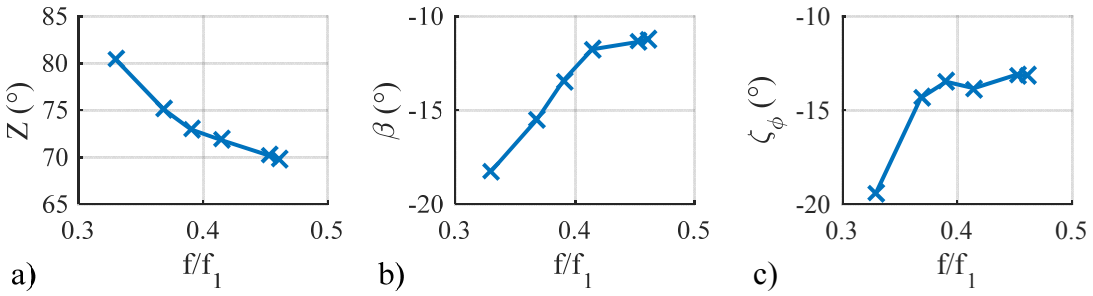

Figure 5.1. Required control inputs, u = [Z, β, ζ_φ], to achieve hover equilibrium in free flight for a range of frequency ratios used in this study.

Table 5.1. The range of stiffness and select nondimensional parameters used in the current study. We directly vary Young's Modulus and therefore the frequency ratio. The trim algorithm returns the required flapping amplitude Z to hover. The reduced frequency *k* is determined from the flapping amplitude.

prescribed parameters		obtained from the trim algorithm	
Young's Modulus (N/m^2)	f/f_1	Z (degrees)	k
8.5×10^8	0.288	87	0.202
8.0×10^8	0.304	85	0.207
7.5×10^8	0.329	81	0.217
7.0×10^8	0.368	75	0.235
6.5×10^8	0.390	73.5	0.239
6.0×10^8	0.414	72	0.244
5.5×10^8	0.441	71.5	0.249
5.3×10^8	0.452	70.7	0.250
5.25×10^8	0.455	70.1	0.251
5.15×10^8	0.461	69.8	0.252

Increasing the frequency ratio decreases the flap amplitude required to hover. The flap amplitudes for the fully converged cases ranged from a high of Z = 80.5° for f/f_1 = 0.33 to a low of 69.8° for the most flexible case (f/f_1 = 0.461). This range of flap amplitudes and stroke plane angles is larger than those of rigid wings in Section 4.3, but they agree well with the amplitudes used by live fruit flies reported in the literature. Hedrick et al. [76] report a stroke amplitude of 70°, and Fry et al. [32] observed six different fruit flies that utilized a range of flapping amplitudes from 60° to 73.5°.

Lehmann and Dickinson [57] report that the average value of flap amplitude that corresponds to the lift balancing the weight is 76°. Furthermore, Fry et al. [32] measured the stroke plane angle of a hovering fruit fly to be 12° forward, which agrees well with the range of stroke plane angles determined by our trim algorithm (β = -11° to -13.4°) for the more flexible wings (f/f_1 = 0.46 to 0.39). The time histories of acceleration, velocity and position of each degree of freedom are plotted for a single cycle in Figure 5.2. Although the acceleration can briefly reach a maximum exceeding two "G's," the average value is less than 3%G, per the convergence tolerance of our trim procedure. Furthermore, the velocity in each degree of freedom only varies by a tenth of a chord per period or less, and the maximum displacements within a cycle are an order of magnitude lower.

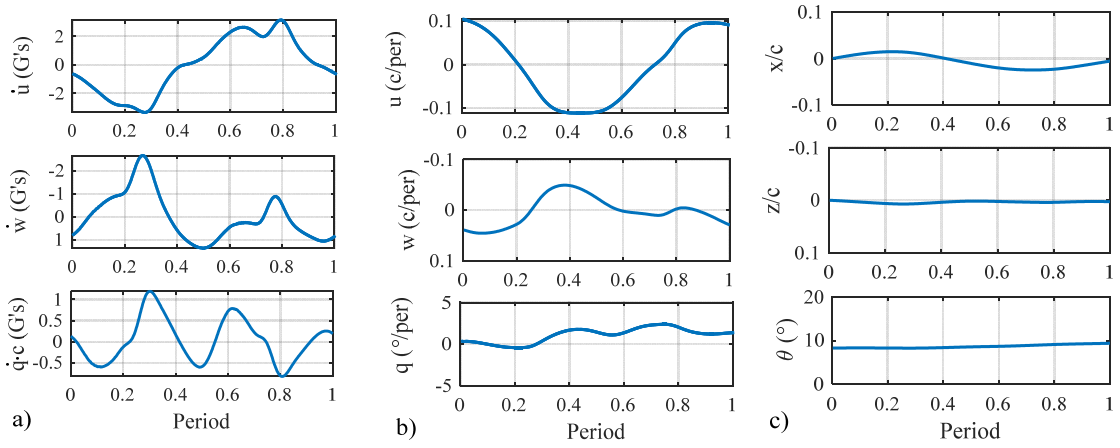

Figure 5.2. The accelerations (a), velocities (b) and positions (c) of the FWMAV with flexible flapping wings during the first cycle after the equations of motion are coupled to the aerodynamics from the FSI solution for f/f_1 = 0.41.

5.2. Flexible Wing Kinematics

In order to model flexible wing kinematics, we impose a sinusoidal flapping motion to the wing's leading edge. The wing's passive pitching motion then evolves in time resulting from the interaction of the fluid forces, wing inertia, and wing stiffness. The resulting deformed wing shape represents both aggregate pitch rotation as well as significant wing camber. Therefore, we approximate the wing motion by defining a passive pitch angle α_{flex} that describes the angle between the chord line and the vertical orientation in the wing reference frame, similar to the pitch angle used in the rigid wing portion of this study. This is helpful in describing and comparing the passive wing motion as well as providing a history of wing motion to the quasi-steady aerodynamic model, which is used in the process of finding equilibrium per Section 3.5.2. Figure 5.3 shows the flexible wing response to the imposed flapping motion along with the passive pitch that would correspond to rigid wing rotation depicted in black. The angle of attack in degrees is approximately $AoA = 90 - \alpha_{flex}$, although the actual forces and moments are calculated directly from the solutions to the Navier-Stokes equations and do not depend explicitly on AoA. Since the NS equations are coupled to the flexible beam equations, the aerodynamic forces include contributions from passive pitch angle, camber, wing rotation rates, added mass and both near-and far-wake effects. From Figure 5.3, the deformation of the wing also causes elongation of the wing since the linear beam solver results in only transverse displacement. Therefore, we nondimensionalize by the instantaneous elongated chord length prior to applying the forces and moments to the equations of motion for the FWMAV.

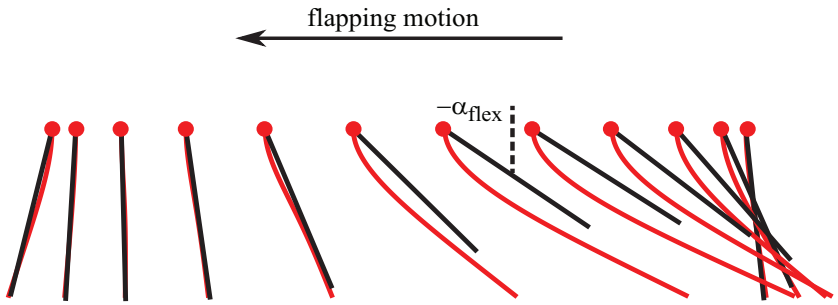

Figure 5.3. Flexible wing deformation (red) and rigid wing motion (black) using the same resultant wing pitch as the flexible case is shown for twelve equal intervals of time in the dorsal to ventral stroke. Z = 127°, k = 0.124, f/f_1 = 0.4. Flapping motion is imposed from right to left on the leading edge, indicated by the red circle.

As in the rigid wing simulations, initial startup transients were observed; however, these transients lasted twice as long in the flexible wing simulations. Therefore, we simulate the flapping motion for six cycles before adding in vehicle response to the aerodynamic forces from the equations of motion. A time history of the resulting passive pitch motion is provided in Figure 5.4(a) for both hover and for a horizontal velocity perturbation of $u = 0.0064U$, resulting in a response that was not seen in the case of the rigid wings. The wing shape itself (vice simply the body) responds to the perturbation. As we discuss in more detail in Section 5.5, this feature of flexible wings impacts the stability of the FWMAV.

Figure 5.4(b) demonstrates the effect of the startup transients on the flexible response of the wing more clearly. After six periods, the wing's response becomes consistent cycle to cycle, absent any body motion. Once body motion is introduced at the

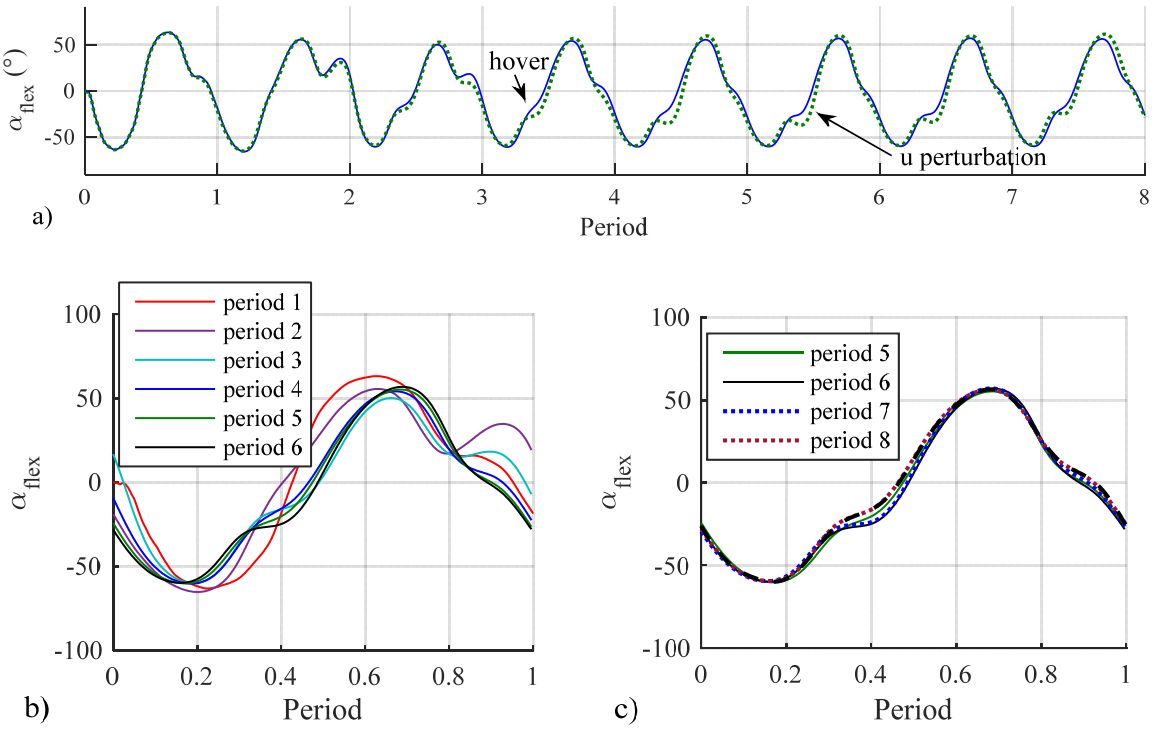

Figure 5.4. Time history of passive pitch angle, α_{flex}, resulting from the dynamic balance of aerodynamic forces, wing stiffness, and wing inertia (a) for f/f_1 = 0.41. Passive pitch angles with the first six periods superimposed (b) to highlight the differences and the convergence to the sixth period. Pasive pitch angles (c) for two periods before (solid) and two periods after (dotted) the FWMAV is allowed to freely respond to aerodynamic forcing. The sixth order Fourier series representation of the eighth period (dashed) is included for reference.

beginning of the seventh period, the wing response changes slightly although it is still close to the wing motion before the fully coupled response. By the eighth cycle, however, the wing motion is noticeably different from the wing response when the body motion was prescribed. The body motion is now coupled with the wing motion, which is a better approximation of the long term response of the system at hover. We store the Fourier series representation of this wing response so that the results can be compared to rigid wing simulations using the same pitch angles as the periodic solution of the flexible wing. The flexible wing angles in Figure 5.4 are obtained from the equilibrium initial

conditions. The body motion that affects the wing's response is primarily its oscillation about equilibrium. Therefore, even though the average acceleration across a cycle is nearly zero, within a cycle, the FWMAV experiences peak accelerations of over two G's (units of gravitational acceleration) in the x_b and z_b directions. The velocities and the displacements within the cycle, however, are very small (see Figure 5.2). This suggests that intra-cycle accelerations that the FWMAV experiences have an effect on the flexible response of the wing, which is an effect that has not been previously observed in the flapping wing literature.

The passive pitch angles depicted in Figure 5.4 are for a single wing stiffness. However, all of the flexible wing configurations that we studied exhibited a similar transition period between the wing response to prescribed versus free body motion at the seventh cycle. The passive pitch angles and pitch rates for several frequency ratios are provided in Figure 5.5. As expected, the lower stiffness experience greater deformation and the max deformation occurs closer to the center of each half stroke (i.e. $\tau = 0.25$ and 0.75). The higher the frequency ratio (lower the stiffness), the smoother the wing response becomes. Indeed, for stiffer wings ($f/f_1 < 0.40$), the pitch angle takes on two separate local maxima in the first half stroke, whereas the wing response only has one peak for $f/f_1 > 0.40$.

Looking at the pitch rates, another clear trend emerges. For $f/f_1 > 0.3$, the more flexible wings reach higher pitch rates. The maximum pitch rate is shifted to later in the cycle. Figure 5.5(c) also demonstrates that the increased deformation for the high frequency ratios occurs in spite of a lower hover flapping amplitude, which yields lower inertial and aerodynamic forces. Recall that flapping frequency is kept fixed. Once

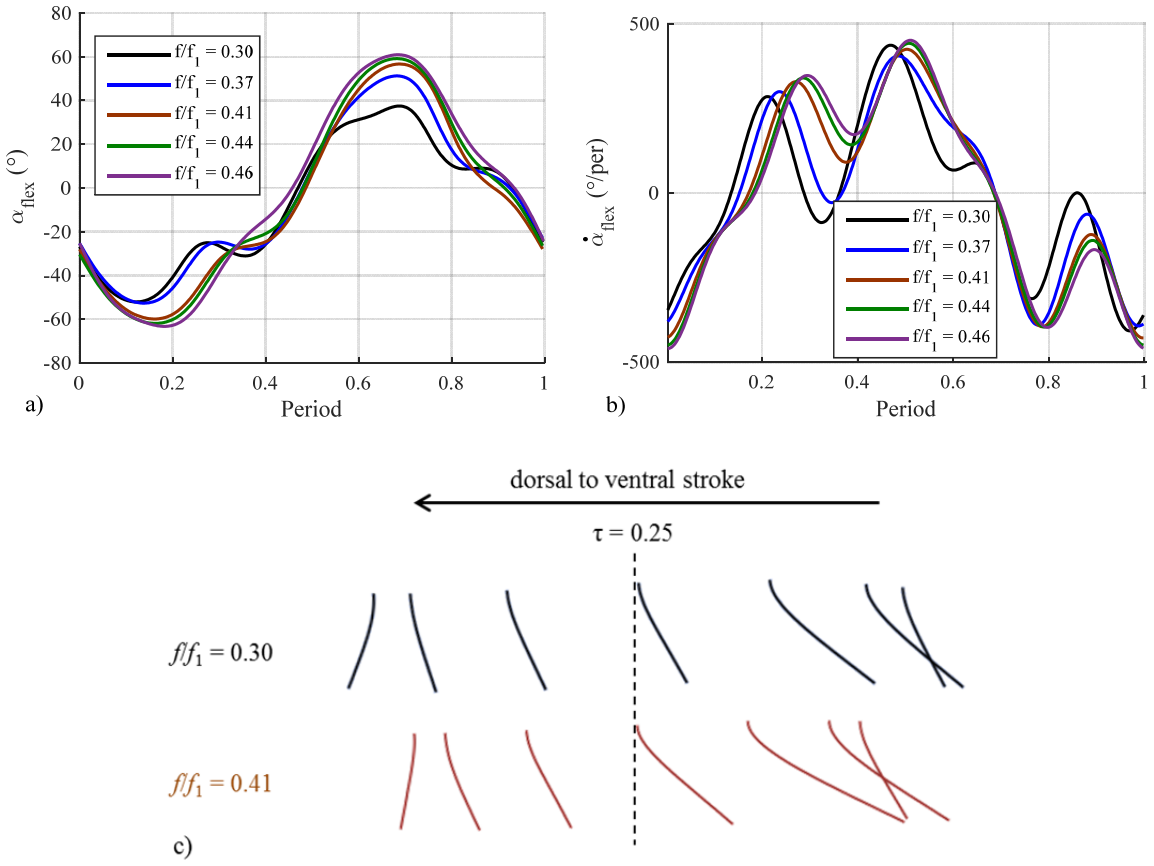

Figure 5.5. Passive pitch angles (a) and pitch rates (b) for five frequency ratios that span the range of stiffness considered in the current study. Wing deformation for two frequency ratios (c) during the dorsal ventral to stroke, centered at τ = 0.25 (the more flexible wing utilizes a smaller flapping amplitude).

again, we see the intriguing three-way coupled nature of the problem. The aerodynamic and inertial forces produce a given force distribution on the flexible wing, which yields an instantaneous wing shape. That wing shape results in an integrated force that itself must be balanced by the appropriate control inputs. But changing the control inputs (i.e. flapping amplitude) also changes the passive pitch. And finally, intra-cycle body accelerations also affect the wing response. The constraint of operating at hover in free flight adds two additional influences (changing stroke amplitude and body oscillations) that make finding a converged solution to the hovering trim problem a challenge.

5.3. Aerodynamic Forces and Moments

Since the kinematics of passive wing deformation are significantly different than the abstracted kinematics that were chosen in Section 4.3, it is logical that the time histories of the aerodynamic forces will also be different, as previously discussed in Kang and Shyy [1] and Sridhar and Kang [13]. That said, the four primary sources of aerodynamic forces still contribute to lift and drag production. Figure 5.6(a) depicts the lift predicted by the FSI solver for a flapping amplitude of 140° and $f/f_1 = 0.41$. The predictions of the QS model, which is based on the Fourier representation of the passive pitch, are included as well. Figure 5.6(b) displays the same breakout of forces for the abstracted wing kinematics used in Chapter 4 for comparison. The QS components indicate that with the flexible wing, the rotational lift and added mass continue to contribute to the total lift even though the timing of the rotational lift is now toward the middle of each half stroke rather than being confined to the ends of the stroke as was the case with the prescribed kinematics. It is also interesting to note that the flexible wing kinematics yield advanced rotation for all of the frequency ratios considered in this study, which was also observed in Sridhar and Kang [13]. However, based on the force plots, the advanced rotation of the flexible wing does not yield the significant increase in forces at the end of the stroke that rigid wings using abstracted kinematics provides (Figure 5.6(b)), primarily because the rotation rates during stroke reversal are so much lower in the flexible case (Figure 5.6(c)).

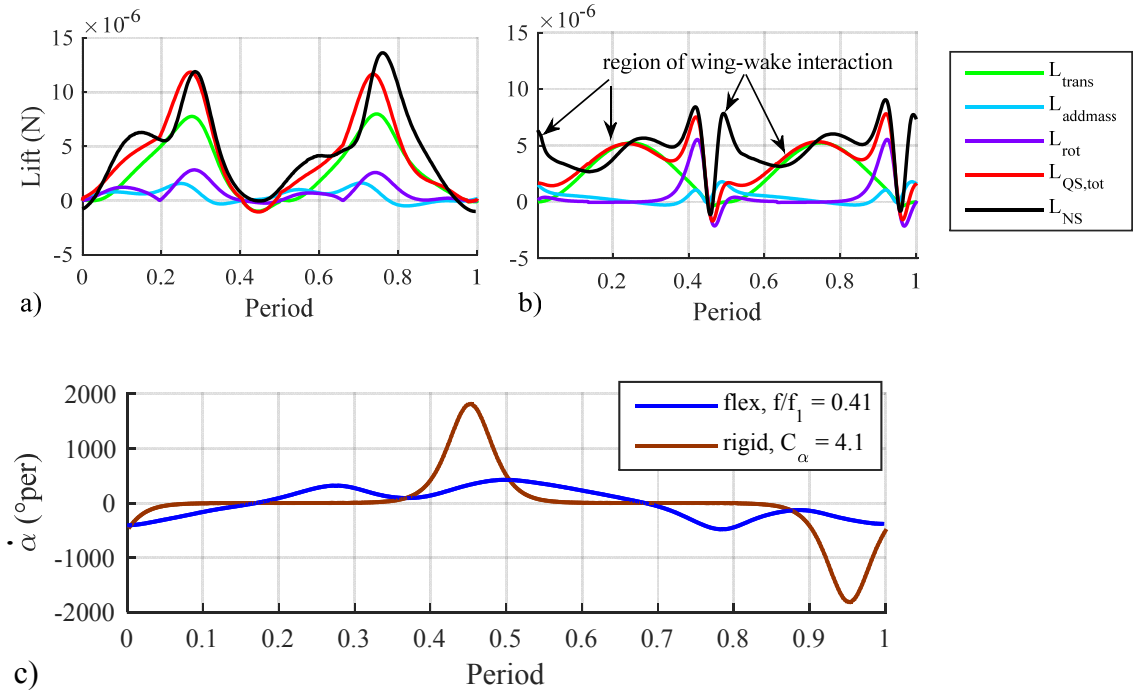

Figure 5.6. The lift produced by a representative flexible wing (a) with f/f_1 = 0.41 per the FSI solution (black). The quasi-steady predictions (colors) based on rigid rotation of a wing using the passive pitch angles help to identify where each form of lift production occurs. The lift history for the abstracted kinematics with rigid wings (b) is also plotted showing the NS solution (black) vs. the QS predictions (colors). The abstracted kinematics utilize x_p/c = 0.25, A = 50°, C_α = 4.1, and advanced pitch rotation (α_φ = 0.3). The pitch rates (c) are provided for comparison as well.

Additionally, the QS model represents the flexible wing aerodynamic forces remarkably well—better than it was able to represent the rigid wing forces. The phenomena not captured in the QS model are wing wake interaction and the effects of wing deformation for flexible wings. Previously we discussed that the primary weakness of the QS model is that it cannot predict wing wake interaction. This gives rise to the main differences between the QS and NS predictions apparent in Figure 5.6(b). The rigid wing experiences a significant increase in lift at $\tau = 0$ (and 0.5) and then a wake valley from $\tau = 0.05$ to 0.2 (0.55 to 0.7). The flexible wing experiences significantly less wing wake interaction.

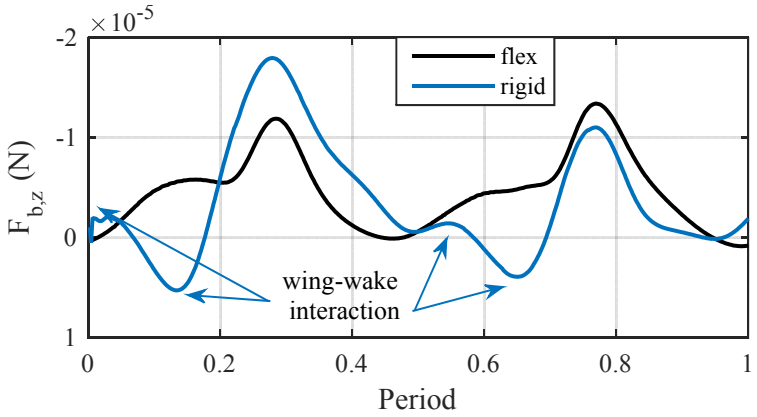

Figure 5.7. The vertical force histories for a flexible wing (black) with $f/f_1 = 0.41$ and a rigid wing (blue) with the instantaneous pitch angle equal to the passive pitch angle. The rigid case depicted here is not re-trimmed for equilibrium; the control inputs are exactly the same as for the flexible case.

Figure 5.7 allows us to test if the flexible pitching schedule alone can mitigate the wing wake interaction, where the lift histories of the flexible wing are plotted alongside the rigid wings using the passive pitch angles (and the same stroke amplitude). Clearly, the rigid wing still experiences significant wing wake interaction. Both a lift peak and the wake valley are present with the rigid wing simulation. During the wake valleys, the passive pitch angle on the rigid wing even produces a downward force. However, from τ = 0.2 to 0.4 and 0.7 to 0.9, which correspond to the best *AoA*s as well as the regions of highest pitch rotation, more lift is produced from the rigid wing than the flexible wing. The associated increased vorticity resulting from the rigid wing can be seen in Figure 5.8, where the flow field during and immediately following stroke reversal is plotted. The vorticity in the flow field is more intense and lasts longer for the rigid wing, leading to both the enhancing and detracting effects of wing wake interaction. From Figure 5.7, however, the lift-reducing wake valleys have a larger effect than the brief lift increment.

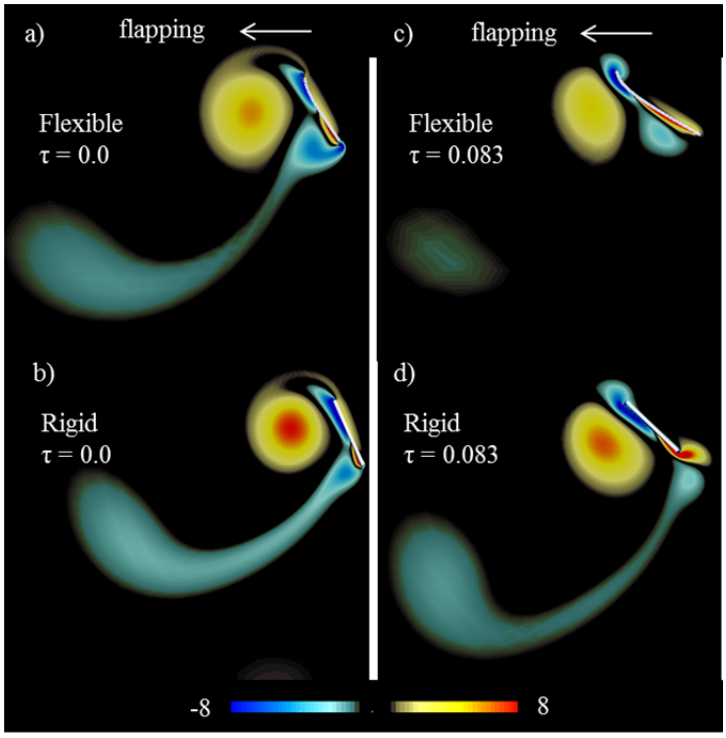

Figure 5.8. Plot of *z*-vorticity in the flow field at stroke reversal (a,b) and shortly after stroke reversal (c,d) for flexible (a,c) and rigid wings (b,d). Vorticity is nondimensionalized by *U*/*c*.

The time histories of the lift and drag coefficients as well as the horizontal and vertical forces for selected values of f/f_1 are provided in Figure 5.9. The lift and drag coefficients represents the nondimensional forces that act normal to the stroke plane (i.e. lift) and opposite wing motion (drag is always positive in this sense). The body forces are required to determine the motion in the body frame as determined via our state vector defines in equation (3.20). The primary difference in these forces is due to the stroke plane angle β, as well as the fact that $-F_{z,b}$ is directed upward in the vertical plane. These plots demonstrate the effect of the different passive pitch angles on the lift and drag as well as body forces. The simulation is re-trimmed for each frequency ratio, which gives rise to some of the interesting comparisons between the plots. For example, the average

vertical force for each of the simulations is the same because it must balance the same weight.

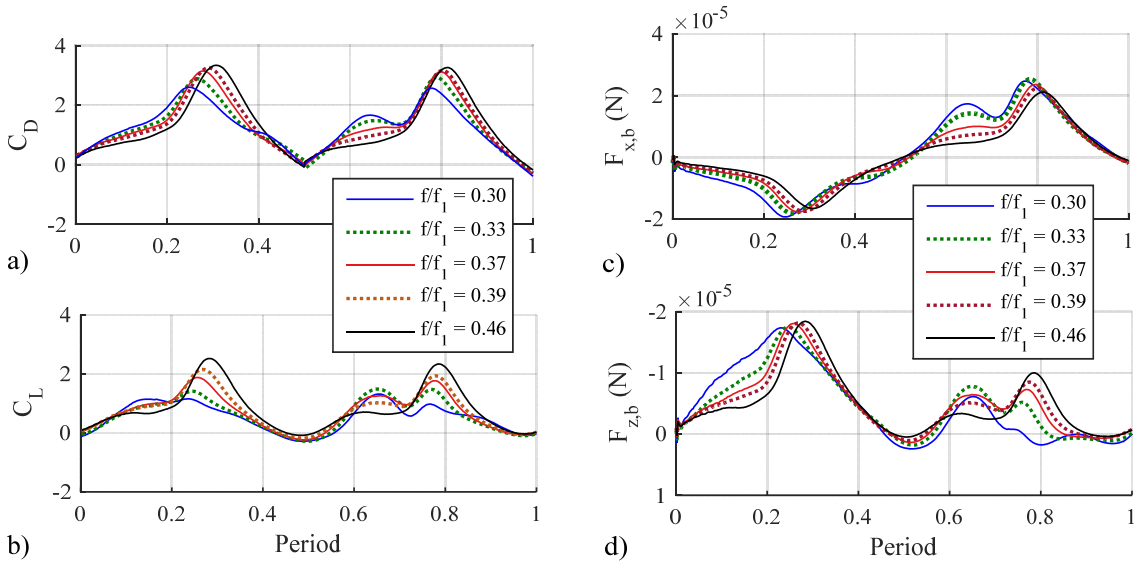

Figure 5.9. Time histories of drag (a) and lift coefficient (b) as well as horizontal (c) and vertical (d) forces in the body frame for various frequency ratios. The axis of the vertical force plots is inverted because -$F_{z,b}$ is oriented up in the vertical plane.

However, there is a clear trend in Figure 5.9(b) that demonstrates that the stiffer wings have lower values of lift coefficient. These lower values of lift coefficient are due to two factors. First, the lower wing deformation of the stiffer wings (see Figure 5.9(a)) leads to *AoA*s above 50°, which is beyond the optimal range of lift at this Reynolds number [27]. The stiffer wings, therefore, must utilize larger flapping amplitudes. But these larger flapping amplitudes further depress the value of the lift coefficient because larger flapping amplitudes lead to a larger reference velocity which is used to non-dimensionalize C_L. This is one reason why we avoid reporting aerodynamic coefficients in this study and prefer dimensional values.

The effect is repeated in the case of drag. Stiffer wings have lower peak drag coefficients, however, they have higher peak drag (and also higher average drag) because the flapping amplitude is larger. Also, the more flexible wings realize force peaks later in each cycle because they achieve higher wing deformation and rotation rates later in each half cycle.

The other differences between the profile of the aerodynamic coefficients and the force histories in the body frame exist because of the body orientation θ and stroke plane angle β. Stiffer wings require larger stroke plane angles to reorient the resulting thrust force vector and flapping offset angles. All considered cases have larger enough stroke plane angles to generate significant differences in the two sets of plots in Figure 5.9. For example, the stroke plane angle for $f/f_1 = 0.33$ is $\beta = -18.3°$. By contract, the stroke plane angle for rigid wings with prescribed kinematics rarely exceeds ±8° because the prescribed kinematics are half-cycle symmetric, while the flexible passive pitch angles are not. This leads to an imbalance in forces between the two half-cycles which must be offset by reorienting the stroke plane. In equilibrium, the FWMAV also requires an initial body pitch angle of $\theta_0 = 16.4°$. Therefore, the actual flapping plane relative to the horizon is almost level. However, expressing the forces in the body frame causes drag in the first half stroke to add to the vertical force in the body frame. Drag in the second half stroke reduces the vertical force in the body frame, which is reflected in the comparison between Figure 5.9(b) and Figure 5.9(d).

5.4. Aerodynamic Power Required

A FWMAV must expend power to generate the forces detailed in the previous section. In Figure 5.10 we plot the time history of flapping power for various values of

frequency ratio next to that of the rigid wing with abstracted kinematics for selected values of pitch axis. The power required to flap from the flexible wing derives primarily from the aerodynamic forces and therefore has a similar shape as the force profiles in Section 5.3. Additionally, the flapping power required has much larger peak amplitudes for flexible wings. This higher power is yet another feature of the larger flapping amplitudes required with the flexible wing. The flexible wing flapping amplitudes range from 70° to 85°, whereas the rigid wing only requires flapping amplitudes of 50° to 70°. Another key difference is that the flapping power for the flexible wing is not directly affected by the (active) pitch rotation of the flexible wing that is evident near $\tau = 0.4$ and 0.9 in the rigid wing (Figure 5.10(b)).

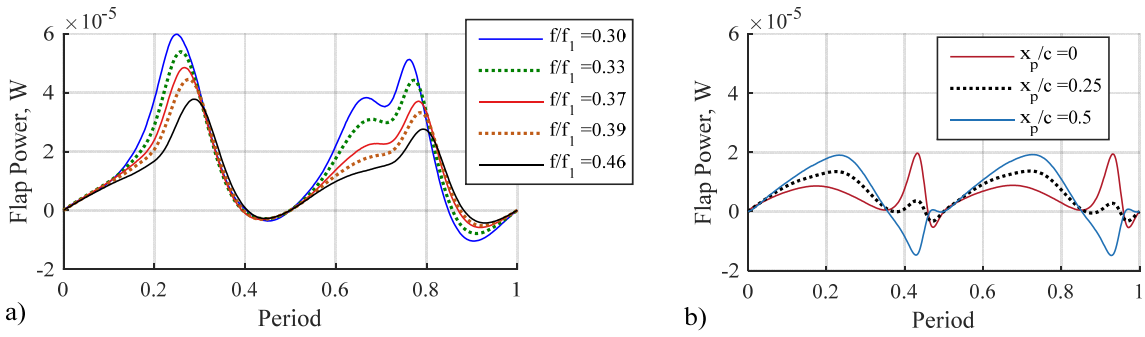

Figure 5.10. Time histories of flapping power for selected frequency ratios f/f_1 (a) and pitch axis locations x_p/c for rigid wings (b) with abstracted kinematics (i.e. A = 50°, $C_\alpha = 4.1$, and $\alpha_\varphi = 0.3$).

Figure 5.11 shows that the aerodynamic contribution is significantly larger than the inertia contribution to flapping power for the flexible wing. The inertial terms consist almost exclusively of the flapping inertia, $I_{yy,w,o}$ (i.e. the flapping inertia I_{yy} of the wing about the wing root, w,o). Additionally, we plot the contributions to flapping power that arise due to changes in the pitch inertia in Figure 5.11(b). In Section 4.4, these terms

added significantly to the flapping power for rigid wings. However, for flexible wings, these terms are four orders of magnitude smaller than the contribution of the flapping inertia itself, which is in contrast to the active flapping of the rigid wing in Chapter 4. This is largely because the pitching motion of the wing is passive, so the coupling of the pitch and flapping inertia is already considered in producing the instantaneous passive pitch angle.

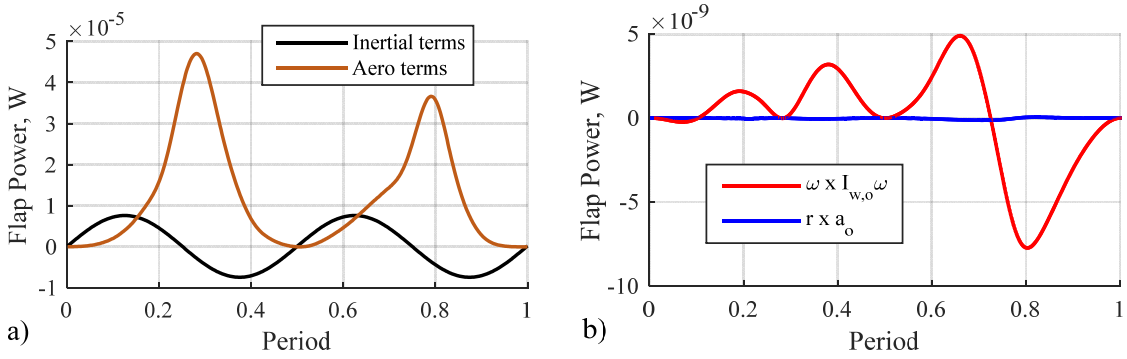

Figure 5.11. The time histories of the inertial (black) and aerodynamic (brown) contributions to flapping power (a) as well as the time histories of the second and third terms of inertial power from equation (3.41) (b). These terms couple in the pitching inertia to the flapping power required, and they become negligibly small for flexible wing motion.

Figure 5.12(a) depicts the average required power to achieve hovering flight for different values of wing stiffness as expressed by the frequency ratio. For the range of stiffness considered in this study, the power required monotonically decreases as the wing become more flexible. The stiffest wing requires 38.5 W/kg of power, which is 66% higher than the most flexible wing studied. This is reflected in the larger lift coefficients and smaller flapping amplitudes corresponding to flexible wings in the previous sections. Despite the larger flapping power amplitudes in Figure 5.10 for flexible wings, the total required power is only slightly larger than the rigid wings with

abstracted kinematics. A primary reason for this is that the flexible wings require no active pitching, and therefore the pitching power is identically zero. Although the power required to hover is not as low as the lowest-power rigid wing configurations, the power required compares favorably to the ranges of power required reported in the literature: 18±6 W/kg [57] and 34.5±9 W/kg [32], which is also plotted in Figure 5.12(a). Furthermore, the passive pitching of flexible wings eliminates any need for active pitching mechanisms, which simplifies the design of a FWMAV and reduces weight.

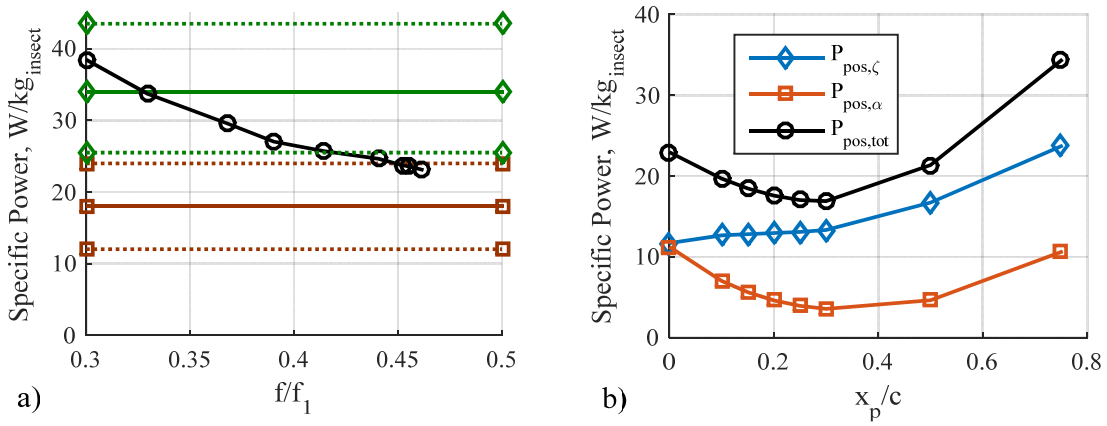

Figure 5.12. The power required to hover for the flexible wing versus various frequency ratios (a) and for the rigid wing with abstracted kinematics (b) versus various pitch axes (A = 50°, C_α = 4.1, and α_φ = 0.3). The required power of fruit flies from Lehmann and Dickinson [57] (□)**and Fry et al.** [32] (◇)**, are also plotted with the average values (solid) and range (dotted) both depicted. The power required reported in this figure is calculated based on Section 3.3, which averages only the positive power contributions across a wing stroke.**

5.5. Stability of Flexible Wings

In addition to the power consequences of adding wing flexibility, the stability consequences of wing flexibility are of particular interest, and have not been previously studied. As mentioned in the sections on the stability of various rigid wing

configurations, the stability can be assessed by examining the open loop poles of the system in equilibrium. In the previous sections, we displayed the NS and QS predictions on the open loop poles. However, when wing flexibility is permitted, only the coupled CFD-CSD results are depicted because QS-CSD models are unavailable.

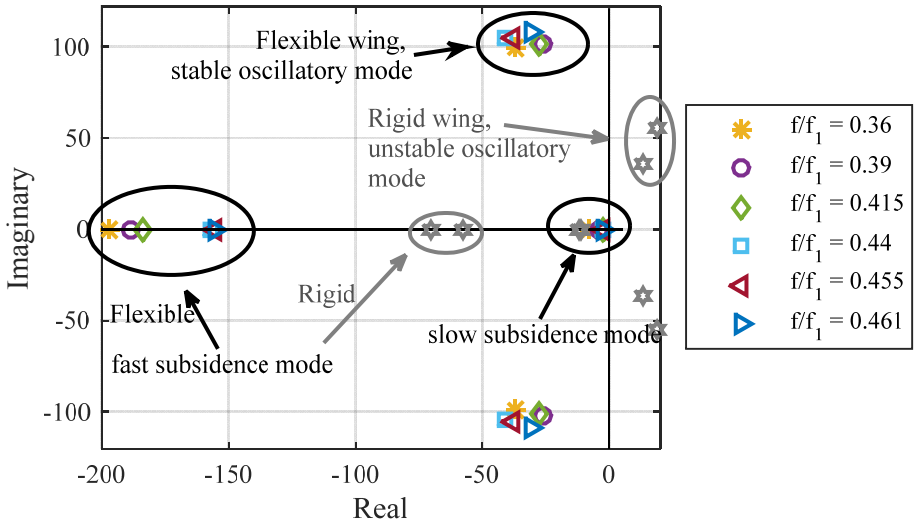

Figure 5.13. The variation in longitudinal open loop poles for various values of frequency ratio f/f_1 based on the coupled fluid-structure-flight dynamics. The poles associated with f/f_1 = 0.3 are not fully converged at hover with accelerations in excess of 5%G, so they are not included. The units associated with each axis are s^{-1}. Rigid wing poles using abstracted kinematics are plotted in gray (A = 50°, C_α = 4.1, and α_φ = 0.3) for comparison.

Figure 5.13 depicts the open loop poles for a fruit fly with flexible wings. Intriguingly, the first observation is that all of the open loop poles for all flexible wings studied have negative real parts, indicating that they are stable. In particular, the unstable oscillatory mode from the rigid wing simulations has become stable and its frequency has increased substantially. Additionally, the least stable mode has now become the slow subsidence mode associated with the heave dynamics. This mode is now more lightly

damped than the rigid wing cases. In the rigid cases, the slow subsidence mode typically had $\lambda_{slow} < -5.0$, whereas for the flexible cases the same pole varies from $-2 < \lambda_{slow} < -5$ for all but the stiffest wing. Finally, the fast subsidence mode has become much more stable than in the rigid wing case by a factor of 2 to 3. The eigenvalues for each value of frequency ratio are provided in Table 5.2.

Table 5.2. Poles of the FWMAV with flexible wings.

E (Pa)	f/f_1	$\lambda_{oscillatory}$ (1/seconds)	λ_{fast} (1/seconds)	λ_{slow} (1/seconds)
7.50×10^8	0.329	$-36.87 \pm 99.3i$	-197.3	-7.94
7.00×10^8	0.368	$-26.21 \pm 102.0i$	-188.4	-4.36
6.50×10^8	0.390	$-27.49 \pm 101.0i$	-183.8	-2.85
6.00×10^8	0.414	$-40.85 \pm 104.6i$	-157.0	-2.56
5.50×10^8	0.441	$-37.83 \pm 105.3i$	-155.3	-2.74
5.30×10^8	0.452	$-31.35 \pm 105.6i$	-160.6	-3.91
5.25×10^8	0.455	$-31.08 \pm 108.5i$	-155.7	-2.16
5.15×10^8	0.461	$-33.26 \pm 111.3i$	-147.3	-2.36

Wing flexibility affects each pole in a different manner. First, increasing the flexibility decreases the magnitude of the fast subsidence pole, but this mode is so highly damped that it is not of further interest. Additionally, as flexibility increases, the slow subsidence mode becomes less stable moving to a lighted damped value of $\lambda_{slow} = -2.15$. Therefore, it appears that the heave dynamics are sensitive to the amount of wing flexibility. The stable oscillatory mode does not show a particular trend with respect to wing flexibility. For all cases that converged within the error tolerance defined in Section 3.5.2 for hover equilibrium, the oscillatory poles are confined to real values of

-27 to -41 s^{-1} and natural frequencies of 99 to 111 rad/s. This mode is similar to the stable oscillatory mode reported in Taylor and Thomas' experiments on live desert locusts [74], which also had large natural frequencies (55 to 100 radians/second). Their experiments, however, were conducted in a simulated forward flight environment in a wind tunnel, so direct comparisons are difficult.

5.5.1. Stability Derivatives and Their Physical Underpinnings.

As we have done for the rigid wing cases, in order to determine the physical causes for the changes in the stability characteristics, the stability derivatives that populate the system matrix must be directly examined. It is helpful to compare the flexible stability derivatives to those of a representative rigid case. Figure 5.14 shows the stability derivatives for the frequency ratios represented in Figure 5.13 along with the stability derivatives for several values of pitch axis location from Section 4.5.1.

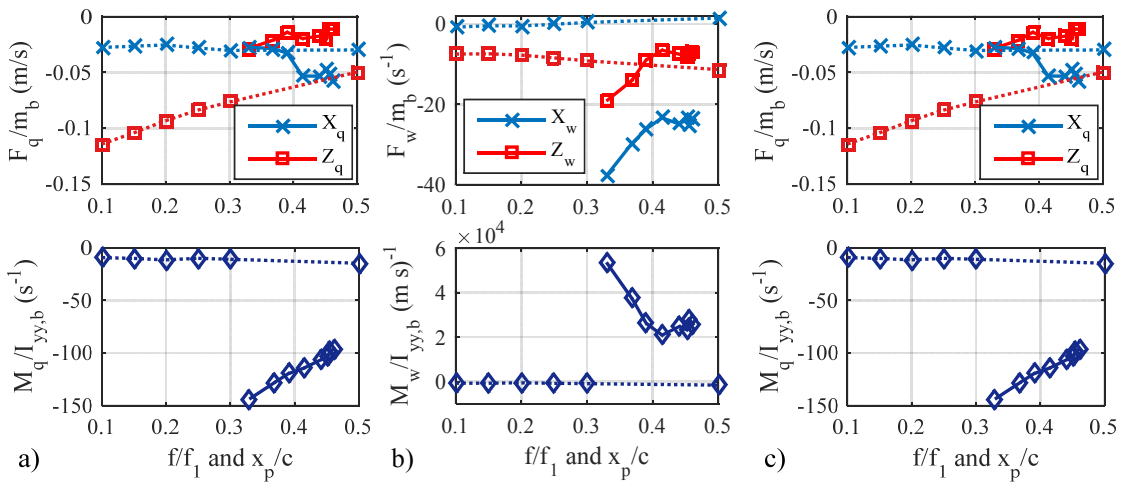

Figure 5.14. Stability derivatives for the flexible wing vs. changes in f/f_1 (solid lines); the stability derivatives for the rigid wings vs. varying pitch axis x_p/c (dotted lines) based on the NS model are included for comparison.

This comparison demonstrates the main differences between the system matrices and the relative sizes of key stability derivatives. Clearly, wing flexibility changes most of the stability derivatives by large factors—an order of magnitude or more in some cases. Three exceptions are the Z_w, X_q, and Z_q derivatives, which are very close to the rigid values. However, these stability derivatives have been previously shown [5,16] not to impact the resulting open loop system dynamics significantly. Therefore, we focus on the remaining stability derivatives to determine the physical causes for the stable open loop poles exhibited by the flexible wing.

Prior to describing the source of the new stability derivatives, we demonstrate the collective effect that varying each stability derivative individually has on the overall system dynamics. Motivated by the presentation of Taha et al. [77], in Figure 5.15, we plot nine root locus diagrams that result from changing the stability derivatives individually for both a representative system matrix from the rigid wings as well as a representative system matrix from the flexible wings. The flexible case depicted in Figure 5.15 and in the following sections is for a frequency ratio of 0.41. Both the flexible and rigid wings exhibit similar modes. The eigenvectors associated with the nominal eigenvalues are listed in Table 5.3, and they represent the participation of each degree of freedom in the mode governed by each eigenvalue.

The modes of the vehicle with flexible and rigid wings are similar. The oscillatory mode consists primarily of pitch rate, then pitch, then horizontal velocity and finally vertical velocity for both rigid and flexible wings. The fast subsidence mode is also governed by the pitch rate, followed by the pitch angle and horizontal velocity. The pitch rate is 180° out of phase with the disturbance in both rigid and flexible wings.

There are differences in the slow subsidence mode for the flexible wing, where now the pitch rate is again the largest contributor. But this mode remains the mode with the largest contribution from the vertical degree of freedom.

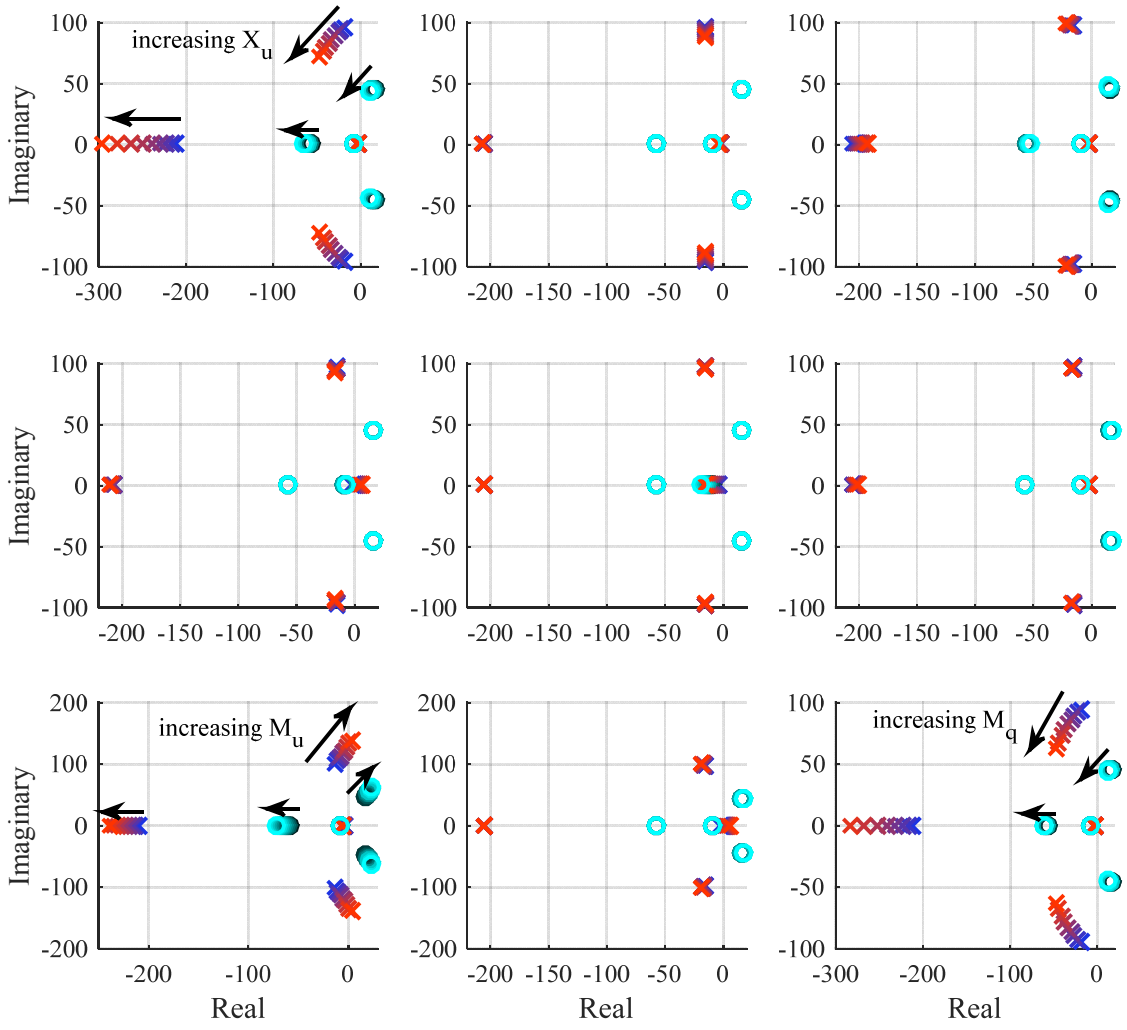

Figure 5.15. The open loop poles are plotted for rigid (×) and flexible wings (o) while manually varying each of the nine primary stability derivatives and holding all the rest constant. In each plot, a single stability derivative is varied from its nominal value to a factor 2.5 of its base value. As the stability derivative is increased, the flexible results vary from blue to red and the rigid results vary from black to cyan. Top left demonstrates the effect of X_u, center left isolates the effect of Z_u, bottom left isolates the effect of M_u, and bottom right illustrates the effect of M_q. The nominal flexible poles are for $f/f_1 = 0.41$. The nominal rigid poles are for A = 50°, $C_\alpha = 4.1$, and $\alpha_\varphi = 0.3$ and $x_p/c = 0.25$.

Table 5.3. Natural modes of motion (eigenvalues and eigenvectors) for rigid and flexible wings.

Rigid	Oscillatory Mode		Fast Subsidence		Slow subsidence	
Pole	$16.5 \pm 45.5i$		-56.9		-8.4	
Eigenvectors	magnitude	phase angle	magnitude	phase angle	magnitude	phase angle
u (m/s)	0.0039	-119.1°	0.0034	0°	0.051	0°
w (m/s)	0.0016	-64.4°	0.0018	180°	0.95	0°
q (rad/s)	0.9998	180.0°	0.9998	180°	0.306	0°
θ (rad)	0.0207	110.0°	0.0176	0°	0.036	180°

Flexible	Oscillatory Mode		Fast Subsidence		Slow subsidence	
Pole	$-27.5 \pm 101i$		-183.3		-2.85	
Eigenvectors	magnitude	phase angle	magnitude	phase angle	magnitude	phase angle
u (m/s)	0.0006	43.4°	0.0003	0°	0.028	180°
w (m/s)	0.0004	110.0°	0	0°	0.239	0°
q (rad/s)	0.9999	0.0°	0.9999	180°	0.916	0°
θ (rad)	0.0096	-105.2°	0.0054	0°	0.321	180°

Figure 5.15 also illustrates that only a few stability derivatives have any significant effect on the open loop poles. In particular, only variations in X_u, M_u, and M_q have much of an effect on the stability of the system for either the flexible or rigid wings. Indeed, a change in X_u of 2.5 causes an increase in stability of the oscillatory poles by a factor 2.5 and 1.5 for the flexible and rigid wings respectively, while changing the slow subsidence pole by only 7%. Thus, increasing the horizontal velocity damping X_u significantly enhances the stability of the oscillatory mode and the fast subsidence mode, and has virtually no effect on the slow subsidence mode. The slow subsidence mode has been previously shown [15] to consist almost exclusively of the dynamics in the vertical degree of freedom. Furthermore, increasing the pitch rate damping M_q by the same factor of 2.5 results in increasing the stability by 2.1 and 1.3 for the flexible and rigid wings respectively. On the other hand, increasing the speed derivative M_u by 2.5 causes the

flexible wing's oscillatory mode to change from stable to unstable, and for the rigid wing, the instability grows by a factor of 1.4.

From the root locus plots in Figure 5.15, we also learn why the flexible wing is stable. Although M_u rises by a factor of 10.6 (which is destabilizing), both X_u (horizontal velocity damping) and M_q (pitch rate damping) increase by factors of 8.5 and 14.6 respectively. This rise in the damping terms ultimately permits the stable poles that are depicted in Figure 5.13. Because only three stability derivatives affect the oscillatory mode (unstable for rigid, stable for flexible), we focus the following discussion on X_u, M_u, and M_q.

5.5.2. Horizontal Velocity Damping, X_u

To determine the reason that the horizontal velocity damping is so high for the flexible wing, we compare the forces and accelerations in the horizontal direction with and without a horizontal perturbation. Figure 5.16 includes the change in horizontal acceleration, the horizontal forces, the angular rotation rate, and the passive pitch angle which directly informs the stability derivative X_u. We obtain the rigid wing results by running the flexible simulation without a gust and solving for the trim control inputs and initial conditions. The resulting passive pitch angle is stored, and once the solution becomes periodic, the wing motion is expressed as a sixth order Fourier series. This pitching schedule is then played back in a rigid wing simulation using the Navier Stokes aerodynamic model, where the stability derivatives, time histories of forces and moments, and other pertinent data are stored. Because we replay the hover passive pitch angles

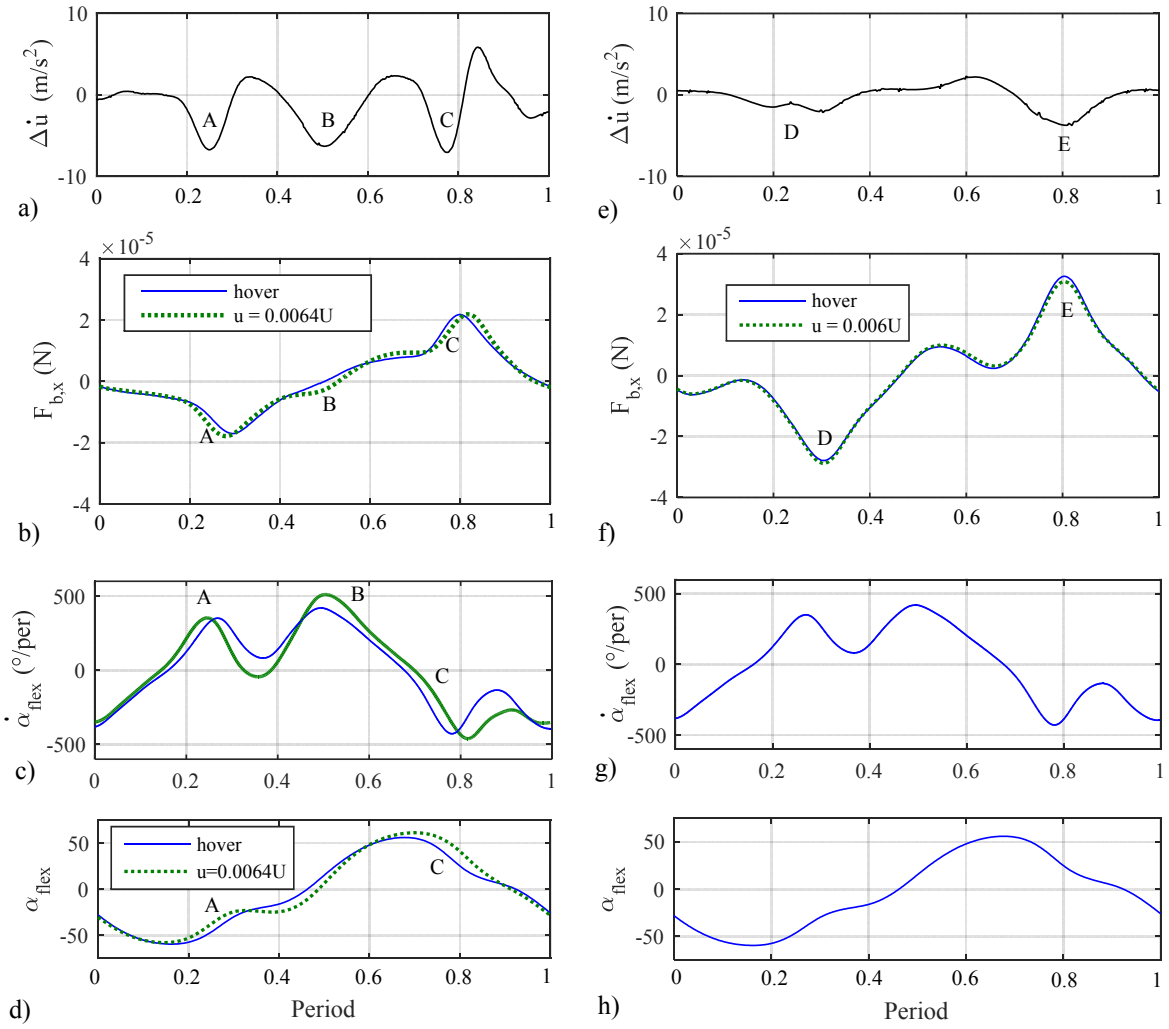

Figure 5.16. Contributions to the horizontal rate damping, X_u. The change in horizontal acceleration, horizontal forces, angular rotation rates, and passive pitch angles for flexible (left) and rigid (right) wings in response to a perturbation in the x_b direction, $u = 0.0064U$. The hover condition is in blue, and the perturbation condition is in green.

(with no perturbation), the only differences between the flexible and rigid results that appear below are from the reduced wing wake interaction of flexible wings and the ability of the flexible wing to deform differently in the presence of a gust. One of the most obvious differences, therefore, in the flexible versus rigid wing comparisons in Figure 5.16 is that the flexible wing is able to change its response (including wing shape) due to the perturbation while the rigid wing is not.

As shown in Figure 5.16, there are portions of the wing stroke where the horizontal rate damping for the flexible wing is enhanced (labeled A, B, C), where the change in horizontal acceleration ($\Delta \dot{u}_b$) is a large negative value. The first occurs from τ = 0.2 to 0.3 (station A in Figure 5.16) in the dorsal to ventral stroke when the horizontal perturbation is opposing the wing motion. The relative velocity of the wing is higher than at hover. This higher relative velocity causes horizontal rate damping ($-X_u$) in both the rigid motion (see also station D) and the flexible motion, and was also noted by previous researchers [8,15]. However, the rate damping in the flexible case is much higher in this portion of the stroke. The primary reason is because the wing's flexible response is different in the presence of the horizontal perturbation. In particular, we see that at τ = 0.25 (where relative velocity is the highest) the pitch angle of the perturbed flexible wing is lower, yielding a higher angle of attack (AoA = 52.3°) than the rigid wing (AoA = 43.5°). The higher angle of attack indicates that the instantaneous orientation of the wing is more vertical, leading to a higher drag. Figure 5.17 provides the deformed wing position and shape with and without a gust for a representative flapping period. The wing's response to the perturbation is not simply a matter of the wing being "blown back" by the higher relative wind in the advancing stroke. Rather, the entire dynamic

response changes the time history of deformation throughout the stroke. Since the flapping (forcing) frequency is lower than the natural frequency of the wing, one would expect a phase delay in the response [89]. Indeed, the largest wing deformation (relative to hover) does not occur at the midstroke ($\tau = 0.25$), but rather near the end of the stroke near $\tau = 0.41$. Finally, the wing's rotation rate is also higher for the flexible wing at $\tau =$ 0.2 to 0.3 when the relative flow velocity is highest, which results in slightly larger forces as well.

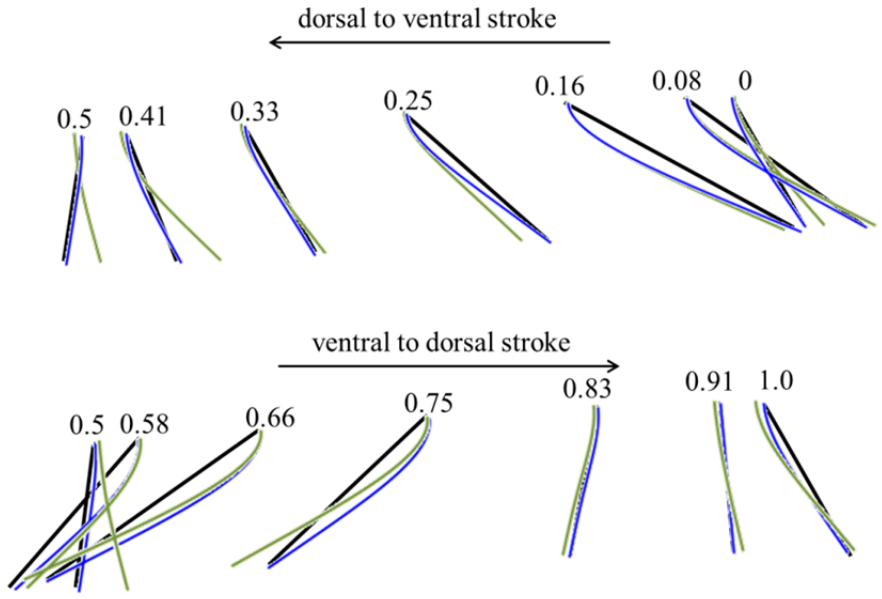

Figure 5.17. Deformed wing motion for hover (blue) and under a horizontal perturbation (green) of $u = 0.0064U$. The wing motion used in the rigid wing simulations is also provided (black). The structural response of the flexible wing in a hover and a gust is not the same, leading to higher horizontal velocity damping (larger $-X_u$).

Secondly, there is significant horizontal rate damping X_u in the flexible wing case at $\tau = 0.4$ to 0.6 (station B in Figure 5.16) where no rate damping exists at all for the rigid wing. This arises primarily due to the larger rotational rate in this portion of the stroke

along with a higher *AoA* (the wing is nearly vertical). Not only does the wing shape change due to the perturbation, but also its rate. For example, the unperturbed flexible wing has a rotation rate of 369°/period when it is vertical at $\tau = 0.463$, but the perturbed flexible wing has a rotation rate of 492°/period when it is vertical ($\tau = 0.487$), resulting in a larger force oriented in the $-x_b$ direction.

Finally, at $\tau = 0.7$ to 0.8, the wing is flapping with the relative wind, resulting in a lower relative fluid velocity. This reduces the drag compared to the hover condition in both the flexible wing case (station C of Figure 5.16) and the rigid wing (station E of Figure 5.16), which contributes to $-X_u$. However, the flexible wing has lower drag in this portion of the stroke because it has higher passive pitch and therefore lower *AoA*. Additionally it has a lower rotational velocity than the hover condition in this portion of the stroke as well. Indeed, after $\tau = 0.8$, both the *AoA* and the rotational velocity of the perturbed flexible wing are higher, and there is a spike in drag that occurs near $\tau = 0.85$, resulting in a small region of $+X_u$. However, the $-X_u$ contributions overwhelm the positive contributions, leading to significantly higher horizontal rate damping in the flexible case than the rigid case. This stabilizing influence result from a mechanism that is only possible in flexible wings: the modified wing motion and deformation in response to the new aerodynamic environment created by the perturbation.

5.5.3. Growth in the Speed Derivative, M_u

Wing flexibility makes the FWMAV exhibit greater pitch accelerations in the presence of horizontal velocity perturbations, as measured by the speed derivative M_u. Although the growth in the speed derivative is generally destabilizing (Figure 5.15), this effect is masked by the simultaneous growth in X_u and M_q, which are stabilizing.

Nonetheless, it is still helpful to see how the flexibility affects the pitch sensitivity to horizontal gusts as many of these themes will reappear when we discuss pitch rate damping M_q.

As in the case of the horizontal rate damping, we demonstrate the effect of flexibility by simultaneously analyzing the flexible wing response, the force and moments that are generated and the change in pitch acceleration for both flexible and rigid wings in hover and u-perturbation conditions in Figure 5.18. In order to resolve the various elements that contribute to the moment about the body CG, we plot both the horizontal and vertical forces as well as the contribution to the moment due to the moment arm at which they act. In Figure 5.18 and Figure 5.19, the $\mathbf{r}_{ac/o} \times \mathbf{F}_{aero}$ term primarily represents the effect of lift acting at moment arm fore and aft of the CG due to wing flapping, and the $\mathbf{r}_{o/CG} \times \mathbf{F}_{aero}$ term primarily captures the drag force acting at a vertical offset above the body CG. Although the change in moments appear to be quite small due to the small perturbations used in constructing the linearized system matrix, the pitch accelerations that they produce are significant due to the low rotational inertia of the body ($I_{b,yy} = 5\times10^{-13}$ kgm^2). The stability derivatives (e.g. M_u and M_q) are based on the net body accelerations due to velocity perturbations. We therefore display both the forces and moments that cause the accelerations and the net acceleration itself in Figure 5.18 and Figure 5.19. The acceleration includes contributions from both forces and moments and from the wing inertial terms. However, the wing inertial terms are not shown in Figure 5.18 and Figure 5.19 because their influence on the stability is negligible [77], even in the case of flexible wings.

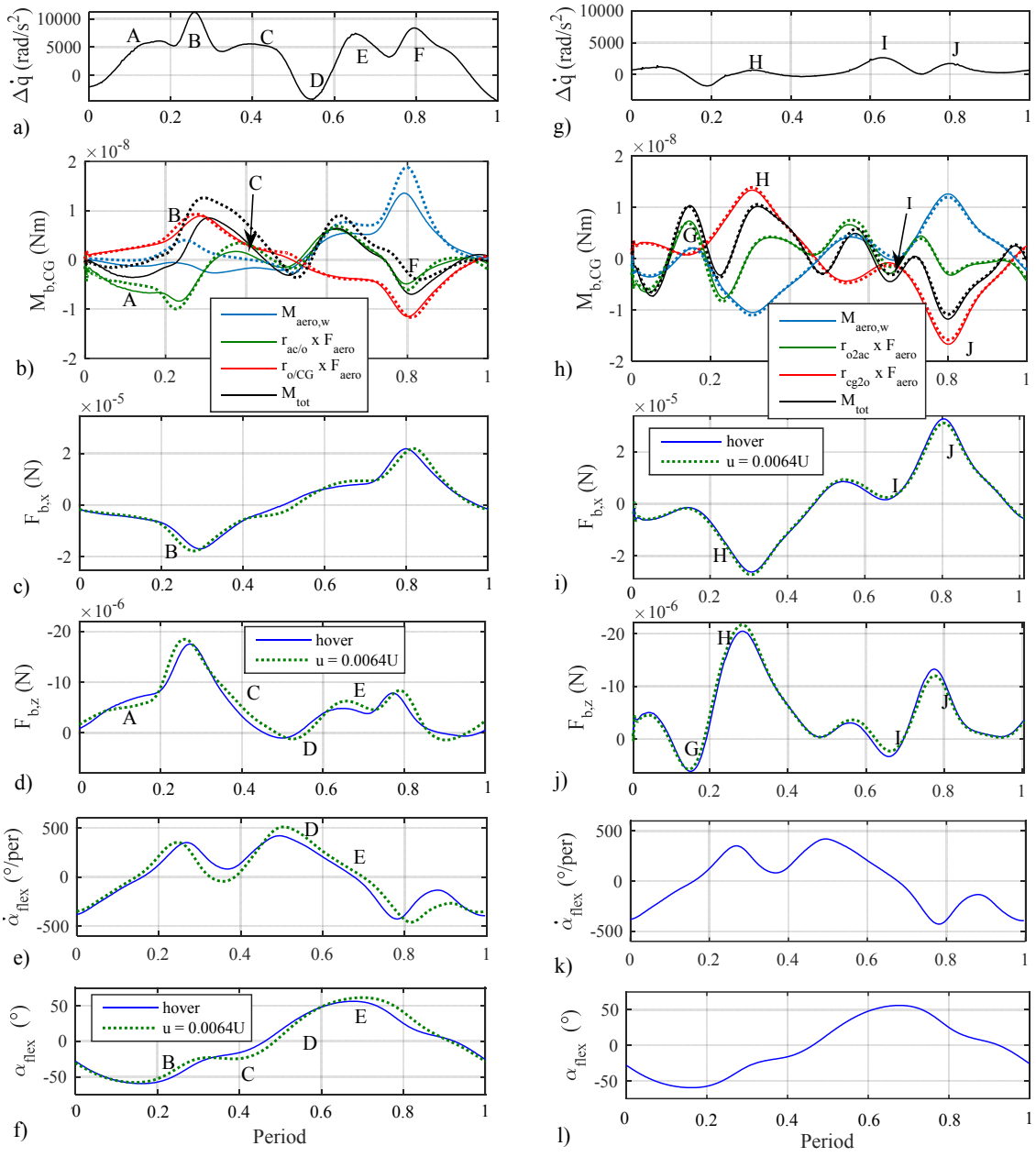

Figure 5.18. The forces, moments, and wing motion that cause the speed derivative M_u for flexible (left) and rigid wings (right). The perturbation case of $u = 0.0064U$ is plotted in the green dotted lines and the hover case is in blue solid. $\Delta\dot{q}$ in (a) and (g) is the difference in pitch acceleration between hover and the perturbation. The first (green) r × F term in subfigures (b, c, h, and i) primarily captures the contribution from lift acting at an offset in the spanwise direction. The second r × F term (red) primarily captures the contribution from the drag acting at a vertical offset above the body CG. Flexible wing motion (e) and (f) reacts to the perturbation; rigid wing motion, by definition, does not (k) and (l).

In this study, the two primary locations where the moment calculation is important are about the pitch axis of the wing and the body CG. The pressure distribution around the wing results in both a force and a pure aerodynamic moment about the pitch axis of the wing. The pitch axis of the wing is taken to be the leading edge for both flexible and rigid wings, which is one reason why the relative magnitude of the aerodynamic moment is higher than it was for the rigid cases in Chapter 4. This moment will usually be termed the "aerodynamic moment about the pitch axis." The moment about the body CG is the moment that causes pitch accelerations and affects the stability derivative.

There are multiple influences that increase the speed derivative during different portions of the stroke. However, the trend in the flexible case is to consistently increase the nose up moment in the presence of a *u*-perturbation. Beginning at $\tau = 0.15$ (station A in Figure 5.18), a *u*-perturbation slightly changes the wing wake interaction, reducing lift. Since the lift is acting behind the CG, a reduction in lift yields a nose up moment, contributing to $+M_u$. Then at $\tau = 0.25$ (station B), the drag and the pure moment contribute to the nose pitch $+M_u$ in a gust. The relative wind is higher due to the perturbation. Hence, the increased drag acting at a moment above the body CG causes a nose up moment. Additionally, the relative wind and decreased wing deformation increases the magnitude of the pure moment developed by the pressure distribution along the wing. The wing response is the same as that depicted in Figure 5.17. At $\tau = 0.35$ to 0.45, the lift is higher because the wing adopts a more advantageous *AoA* in this region under a perturbation. This lift is now in front of the CG, further contributing to $+M_u$. At $\tau = 0.5$ to 0.6 (station D in Figure 5.18), there is a brief region where the moment is negative with the perturbation. In this region, it is due to reduced lift from a small pitch

angle (and very high *AoA*). Also, the wing's rotation rate is higher, which imparts a negative moment simply due to the pure couple that resists rotation in a fluid. Then from $\tau = 0.6$ to 0.7 the lift in the perturbation case is higher than hover, primarily due to a larger angular rotation rate and better *AoA*. More lift in front of the CG increases $+M_u$. Finally, at $\tau = 0.8$ (station F in Figure 5.18), we see an increase in pitching moment about the body CG during a perturbation. Here the largest contributor is again the pure moment developed on the wing. Therefore, influences that only exist in flexible wing cases (the wing's response to the perturbation and reduced wing wake interaction) modify the speed derivative relative to the rigid wing.

In the rigid case, the amplitude of variation in pitch acceleration is much lower. The sources of the speed derivatives for the rigid motion (using the flexible pitching schedule) are largely the same as those discussed for rigid wings using abstracted prescribed kinematics (Section 4.5.2), but we review them here as well. The most significant contribution to $+M_u$ is the drag term acting above the body CG, which is increased in the advancing half stroke (station H in Figure 5.18) and decreased in the opposite half stroke (station J in Figure 5.18), both of which yield a nose up moment. Additionally, the wing wake interaction affects the forces and moments near $\tau = 0.15$ (station G) and $\tau = 0.65$ (station I). As described in Section 5.3 and [1], rigid wings are not able to adapt to the aerodynamic forces, and therefore, their motion produces vortical structures with increased strength in the wake that impact the force production in the following half-stroke. The effect of this wing wake interaction is to decrease the lift particularly at $\tau = 0.65$ (station I) in both the hover and perturbation cases. However, the decrease in lift in the perturbation cases is smaller, which increases the $+M_u$, by

effectively increasing the lift in front of the body CG. Finally, there is a $-M_u$ associated with the pure moment about the pitch axis of the wing. However, in the rigid wing, the change in pure moment is small and strictly the result of the relative velocity at $\tau = 0.25$ and 0.75 since no changes in wing shape are possible with the rigid wing.

5.5.4. Pitch Rate Damping, M_q

As demonstrated in Figure 5.15, the pitch rate derivative M_q is the third stability derivative that has a large effect on the stability of the overall system. Pitch rate damping exists when $M_q < 0$, when a nose up (positive) pitch rate of the body yields a nose down (negative) moment and pitch acceleration. As $-M_q$ increases in magnitude, the stability improves. Figure 5.19 depicts the relevant contributors to the moment about the body CG due to a body pitch rate for flexible (left panel) and rigid wings (right panel). In both panels, the change in pitch acceleration is plotted first, followed by the moment contributors, the pitch angle, and the pitch rate. The first noticeable difference between this perturbation and the horizontal velocity perturbation studied in the last section for M_u is that the passive pitch angle is not as strongly affected by the pitch rate perturbation. As in Figure 5.18, the $\mathbf{r}_{ac/o} \times \mathbf{F}_{aero}$ term primarily represents the effect of lift acting at moment arm fore and aft of the CG due to wing flapping. The $\mathbf{r}_{o/CG} \times \mathbf{F}_{aero}$ term primarily captures the drag force acting at a vertical offset above the body CG. Although the change in moments appear to be quite small due to the small perturbations used in constructing the linearized system matrix, the pitch accelerations that they produce are significant due to the low rotational inertia of the body ($I_{b,yy} = 5\times10^{-13}$ kgm^2).

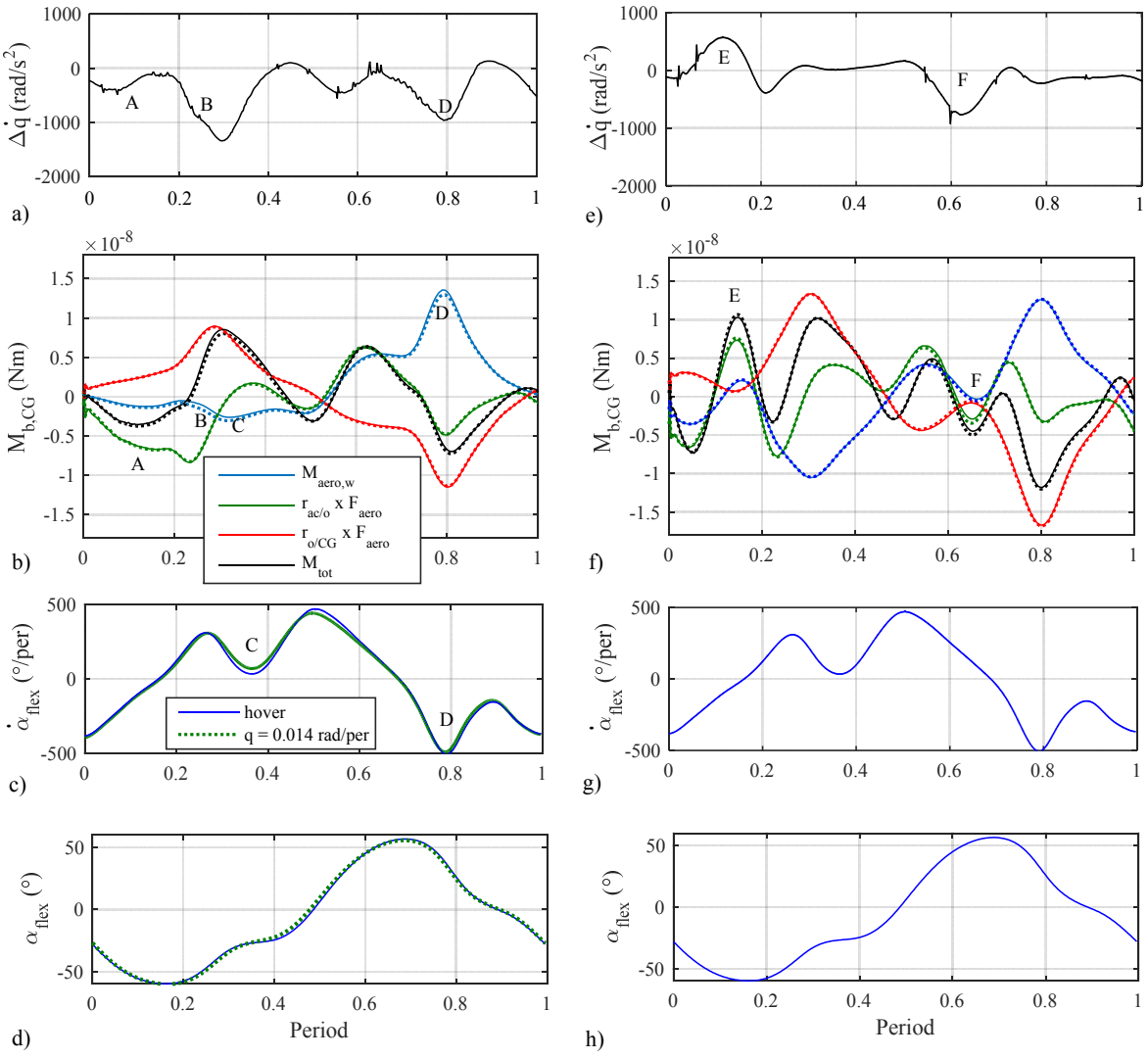

Figure 5.19. The forces, moments, and wing motion that cause the speed derivative M_q for flexible (left) and rigid (right) wings. The perturbation case of q = 0.014 radians/period is plotted in the green or dotted lines.

Beginning at $\tau = 0.1$ to 0.2 (station A in Figure 5.19(a,b)) the increase in lift in the perturbation (dotted green line in Figure 5.19(b)) contributes to the nose down moment about the body CG for the flexible wing. This small increase in the magnitude of the lift is due a slightly better *AoA*, which is a result of both the passive pitch angle and the new effective *AoA* produced by the pitch rotation itself. This lift is created aft of the wing root, producing a nose down moment about the body CG.

A nose down aerodynamic moment (blue curve in Figure 5.19(b)) also arises in the presence of a body nose up pitch rate throughout the stroke as described in Fung [98]. This moment is also dependent on the velocity of the relative wind, so it is most evident at station B. But it applies throughout the entire stroke for both flexible and rigid wings (although it can be overwhelmed by other features).

There an additional contribution from the pure aerodynamic moment about the wing leading edge (blue line in Figure 5.19(b)) that appears at the midstroke and lasts until stroke reversal ($\tau = 0.25$ to 0.5 marked by station C). In this region the wing rotational velocity of the flexible wing in the *q*-perturbation is slightly larger (Figure 5.19(d) and Figure 5.20). This larger wing rotation rate adds to the nose down aerodynamic moment about the wing pitch axis. It is analogous to the moment produced by rotation of a body per Fung [98]. The higher rotation rate of the flexible wing about the leading edge results in a higher relative velocity at the trailing edge. As a result, a lower pressure region forms behind the wing and, hence, a larger nose down pitch moment about the leading edge is created. This is the same mechanism that causes increased aerodynamic forces during regions of wing rotation rate. We do not see a significant effect on the lift or drag in this portion of the stroke ($\tau = 0.25$ to 0.5), however,

because the relative velocity of the fluid is lower in the first half stroke due to the *q*-perturbation.

There is a similar phenomenon between $\tau = 0.7$ and 0.85 (station D), where a nose down change in aerodynamic moment about the leading edge (blue line in Figure 5.19(b)) develops. In this portion of the stroke, the pressure distribution causes a nose up aerodynamic moment about the pitch axis (which also produces a nose up moment about the body CG) with and without a *q*-perturbation. However, the nose up moment is lower in a *q*-perturbation, which yields a further contribution to the stabilizing $-M_q$. In this portion of the stroke, we have a lower wing rotation rate (station D in Figure 5.19(d)) as a result of the wing's response to the perturbation. In this case, the reduction in the wing rotation rate produces a lower aerodynamic moment for the same reasons that occurred at station C. We do not see a drop in the rotational forces at this portion of the stroke because the body rotation slightly increases the wing velocity.

For the rigid wing, the pitch rate damping arises for the same reasons that were identified in Section 4.5.4. First, as in the flexible case, there is a small negative moment developed throughout the stroke simply from the restoring moment that generally accompanies a pitching flat plate in a fluid. However, the wing wake interaction dominates the moment production in both halves of the stroke. Specifically, at $\tau = 0.1$ to 0.2 (station E in Figure 5.19(e) and (f)), the loss of lift in the "wake valley" [31] behind the body CG causes a nose up moment, which is destabilizing. This occurs in the same portion of the stroke that the flexible wing experiences a stabilizing tendency due to increased lift to the body pitch rotation. In the next half stroke, the loss of lift in the wake valley at $\tau = 0.6$ to 0.7 (station F in Figure 5.19(f)) in front of the body CG causes a nose

down moment and is stabilizing. The loss of lift in the first half stroke is weaker than the loss of lift in the second half stroke, so the overall effect is a nose down moment. The primary reason that there is a difference in the wing wake interaction between the hover and pitch rate perturbation cases was previously suggested by Cheng and Deng [8]. The pitch up motion imparts a downward vertical velocity to the wing when the wing is behind the wing root, and an upward vertical velocity when in front of the wing root. The downward vertical velocity for $\tau < 0.25$ causes an apparent upwash on the wing in this portion of the stroke, which enhances lift, and the opposite effect is seen in the opposite half stroke. This works in tandem with the wing wake interaction to produce the negative pitching moment, although it is clearly not large enough to stabilize the FWMAV as it is for flexible wings.

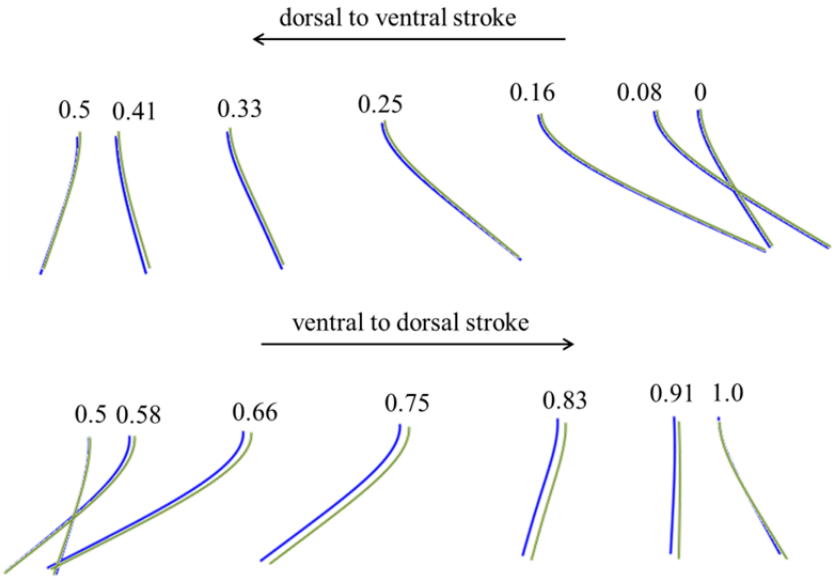

Figure 5.20. Deformed wing motion for hover (blue) and under a pitch rate perturbation (green) of q = 0.014 radians/period. The flexible wing motion in a hover and a gust is more similar than in the horizontal perturbation case, but some differences are evident.

Thus, the flexible wing has a higher magnitude of $-M_q$ compared to its rigid counterpart for two primary reasons. First, the flexible wing does not have to overcome the destabilizing tendency of the wing wake interaction. Secondly, the aerodynamic pitch moment about the flexible wing is more negative, largely because of the faster passive pitch rate due to the wing deformation between the hover and q-perturbation case.

5.6. Evolution of Flight from Hover

Based on the open loop poles of the system, the FWMAV appears to have a stable response. In this section, we simulate the flight of the FWMAV as it evolves after beginning near hover. We compare the results of the flexible wing with two different rigid wing simulations: one with abstracted kinematics from Chapter 4 and the other with a pitch schedule that matches the flexible wing's passive pitch.

Figure 5.21 depicts the response of a representative flexible wing ($f/f_1 = 0.41$) to the rigid wing setup from Section 4.5 (A = 50°, $C_\alpha = 0.1$, $\alpha_\varphi = 0.3$ and $x_p/c = 0.25$). The first observation is that the trimming procedure described in Section 3.5 effectively identifies trim conditions within the given convergence margin. Even for the unstable response of the rigid wing, the growth in the highest response (vertical velocity rate) is still less than 1 chord per period after ten cycles. Additionally, the non-zero initial conditions that are required for trim can be seen in each degree of freedom at $\tau = 0$. Secondly, the periodic forcing of both wings causes cyclic variations in all three degrees of freedom. The horizontal velocity u for both the rigid and flexible wing has a one-per-cycle pattern with a similar amplitude and shape indicating that integrated effects of the drag forces are similar despite the different kinematics.

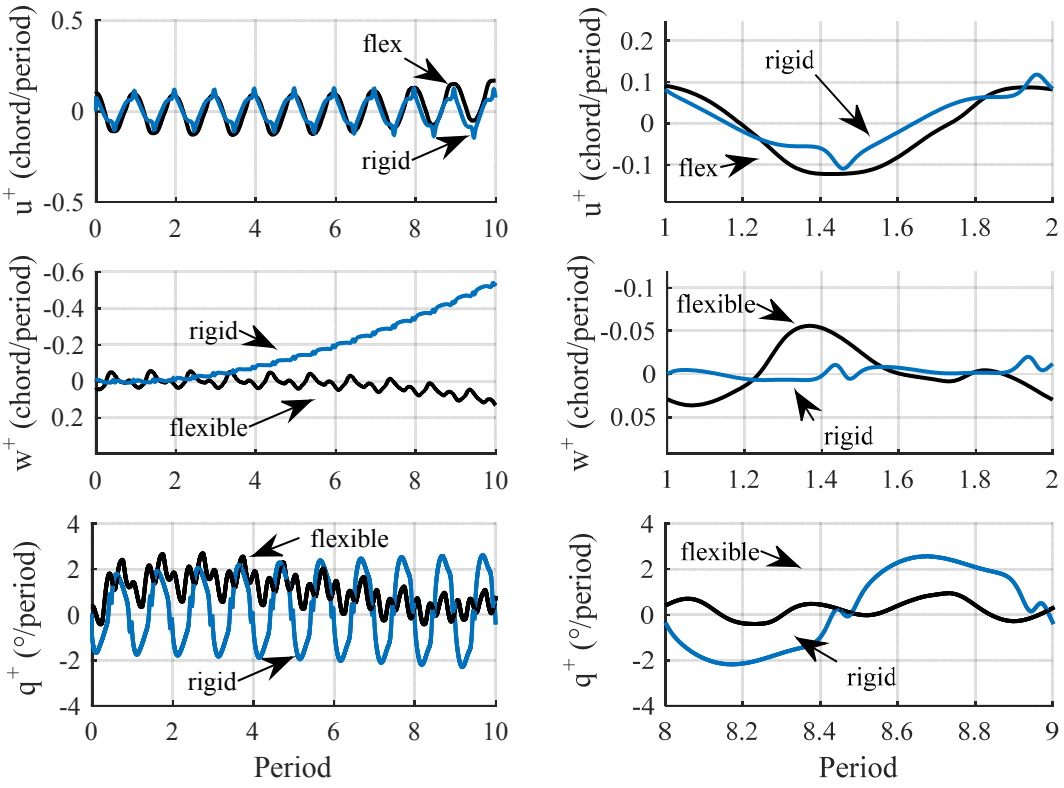

Figure 5.21. The longitudinal evolution of flight when started from equilibrium conditions in hover for flexible and rigid wings. The flexible wing has a frequency ratio f/f_1 = 0.41, and the rigid wing uses abstracted kinematics with A = 50°, C_a = 4.1, α_φ = 0.3 and x_p/c = 0.25. The left side depicts the simulation for ten full cycles. The right side shows the details of a single period.

The vertical velocity *w*, however, shows several differences. The first is that the rigid wing is unable to maintain a zero vertical velocity, whereas the flexible wing is able to remain closer to an average velocity of zero. The rigid wing begins to depart from equilibrium after the eighth cycle. Additionally, the velocity profile itself is quite different, which can be seen in Figure 5.21(b). The rigid wing, however, which holds a constant pitch angle for most of the stroke, exhibits much less variation in vertical velocity. On the other hand, the passive pitching of the flexible wing results in a larger range of pitch angles and also causes most of the lift to be created in the mid-stroke.

This force profile causes larger half-cycle variations in the vertical force. This gives rise to a larger amplitude of vertical velocity and a clear two-per-cycle lift profile seen in Figure 5.7.

Finally, the pitch rate profile for the flexible and rigid wings is also different. Both seem to be able to hold their position well, with an average pitch rate very close to zero. In this degree of freedom, however, the pitch rate variation of the rigid wing has a much higher amplitude and lower frequency of once per cycle, whereas the flexible wing has a three-per-cycle oscillation and lower amplitude. The reason for this is evident from the total moment about the CG in hover (solid black line depicted in Figure 5.18(b)), where the moment about the body CG changes sign six times in the course of a single cycle. On the other hand, the moment about the CG for a rigid wing changes sign twice per cycle. This also contributes to the high natural frequency of the body motion (i.e. $\omega_{1,2}$) relative to the rigid case.

Figure 5.22(a) depicts the response of the same flexible wing in comparison to a rigid wing simulation using the passive pitching schedule obtained during the flexible wing simulation. In this situation, the vehicle is re-trimmed, resulting in a new set of control inputs and initial conditions even though the same pitch schedule is used. The flap amplitude of the rigid wing using the flexible pitch schedule is 85.0° whereas the flap amplitude of the flexible wing was 72.8° as shown in Figure 5.22(b).

The rigid wing, therefore, requires 40.1 Watts/kg of power to flap versus 27.1 Watts/kg for the flexible wing, or a 48% increase in required flapping power for the rigid wing. This is primarily due to the higher lift generation for the flexible wing by

streamlining its wing shape, reducing the lift-degradative wing wake interaction (see Section 5.3).

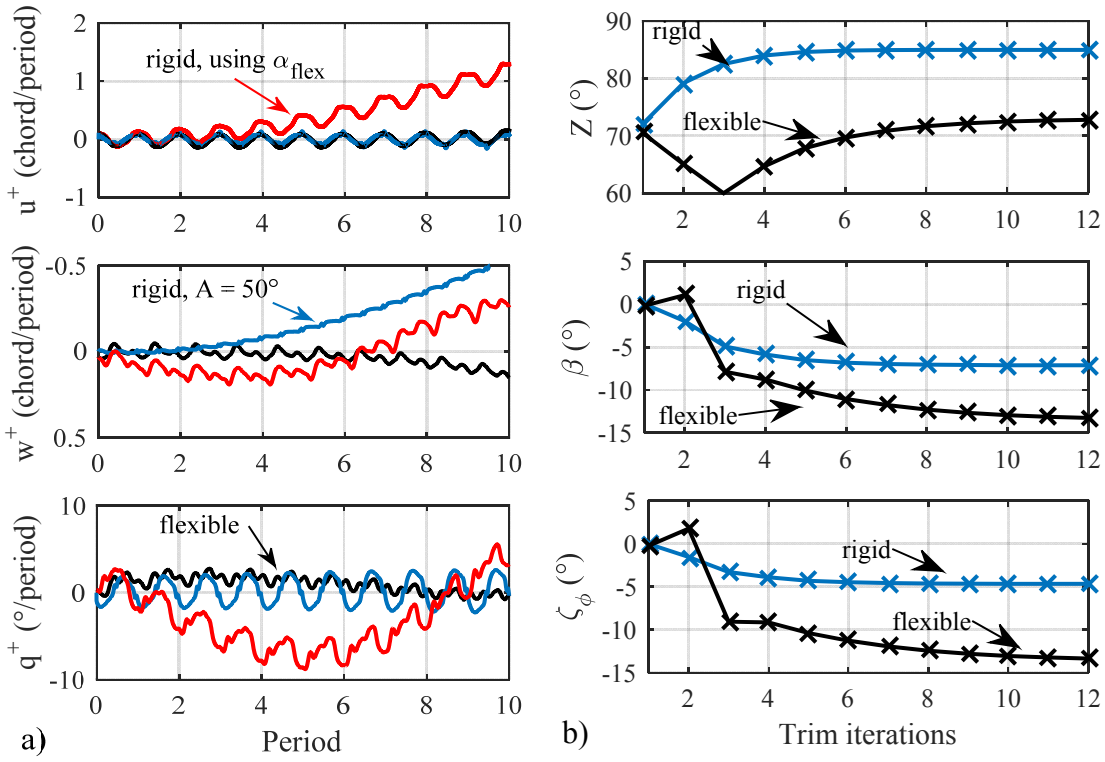

Figure 5.22. The longitudinal evolution of flight when released from hover for flexible and rigid wings (a). The rigid wing from Figure 5.21 is retained (blue), and a rigid wing that the pitch schedule based on the flexible wing response is included (red). The required control inputs (b) are plotted vs. trimming iteration for the flexible wing where f/f_1 = 0.41 (black) and a rigid wing (blue) using the passive pitch angles produced by the flexible wing. Both flexible and rigid wings are trimmed in less than fifteen iterations of the rigid NS or coupled CFD-CSD solver.

Figure 5.22 shows that the longitudinal response of the rigid wing using the flexible pitching schedule also has a significantly larger response in all degrees of freedom than the flexible wing itself. This demonstrates that the pitching schedule alone is not enough to stabilize the FWMAV. As discussed in Section 5.5, the other effects of the flexible wing (reduced wing wake interaction and the ability of the wing shape to respond to perturbations) are more important than the pitching schedule itself.

This might also explain why the experimentally observed pitching schedule reported by Fry et al. [32] that is shown in Figure 3.3 did not appear to confer any benefits on the FWMAV when simulated with rigid wings. The power and stability results of these simulations are show in Figure 5.23. The power is higher than the abstracted kinematics, and the stability is not significantly better – it certainly does not exhibit stable open loop poles. When a biological pitching schedule, which itself results from wing flexibility, is reproduced using a rigid wing simulation, the benefits are not seen because the true source of these benefits, i.e. the ability to adjust the wing shape and its dynamics under some perturbation, is not simulated.

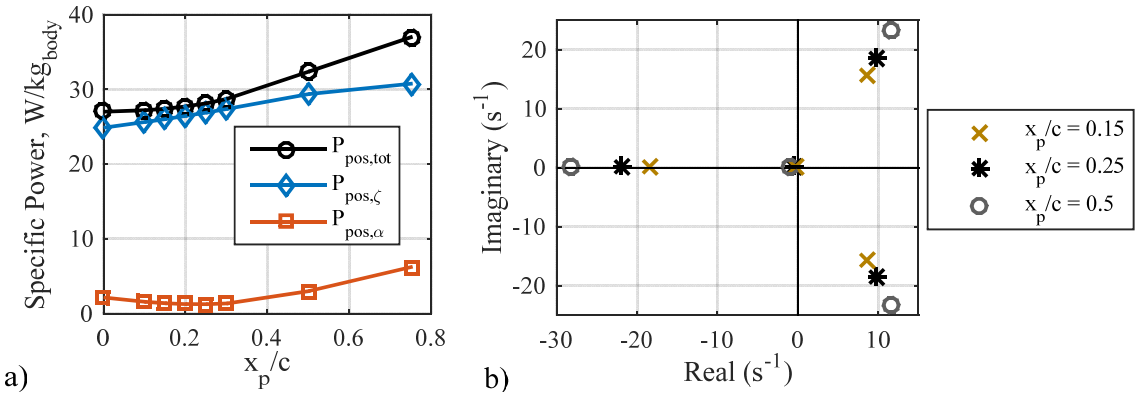

Figure 5.23. The required specific power (a) and open loop poles (b) of a rigid wing simulation using biologically observed time history of pitch angle from [32]**.**

5.7. Summary of Flexible Wing Results

The introduction of wing flexibility has significant ramifications on the performance and stability of a FWMAV. The passive pitching motion is not controlled

or prescribed. Rather, it is allowed to develop as a result of the dynamic balance of the wing inertia, material stiffness, and fluid forces.

Since the aerodynamic forces are a direct function of the pitching kinematics and wing shape deformations, the forces produced by flexible wings are quite different from those of rigid wings using abstracted kinematics. One of the main differences is the much lower wing wake interaction that is evident in flexible wings. This was previously identified in Kang and Shyy [1] and Sridhar and Kang [13], and it is evident in this study as well. Both the lift enhancing and lift reducing effects of the wake are reduced for flexible wings because the flexible wing adapts its shape to the flow field and does not shed as much vorticity from the trailing edge. Therefore, most of the lift is produced in the mid-stroke, and less lift is produced at the stroke reversals, in contrast to the rigid wing studies of Dickinson and coworkers [25–27]. The power required to flap with a flexible wing varies significantly, with the stiffest wings requiring much more power since they also require larger flapping amplitudes.

Perhaps the most significant difference that flexible wings entail is that the open loop poles of the linearized system are now all stable. Most, if not all, rigid wing studies showcase unstable oscillatory poles. This suggests a qualitatively different response than the FWMAV with rigid wings. The flexible wing has different stability characteristics than its rigid counterpart for two main reasons. The first is that the wing shape and its time rate of change adjusts to different perturbation conditions — something that a rigid wing cannot do. The compliant nature of the flexible wing enhances the X_u and M_q damping. Additionally, the wing wake interaction, which has been previously shown to be destabilizing is significantly mitigated. Although these differences can appear to be

subtle, their integrated effect on the stability derivatives is quite significant and large enough to stabilize the FWMAV.

Interestingly, the abstracted kinematics used by Sun and coworkers seem better suited to rigid wings than the flexible or biological pitching schedules. From Section 4.4, they require less power, and the stability characteristics of all rigid wings (whether using abstracted kinematics of passive pitch angles) are unstable. However, wing flexibility provides a significantly more stable platform with only a small increase in power required, and furthermore, it does not need an active pitching mechanism to achieve a desired pitching motion. It is also possible that the sensing and control system could be reduced in view of the more stable dynamics of flexible wings. Such reductions in weight and complexity are highly attractive to designers since the physical dimensions of FWMAVs are, by definition, extremely small compared to typical air vehicles. Additionally, flexible wings are likely to be made from lighter materials than rigid wings. These combined weight savings might also yield significantly higher payload, range, endurance or agility.

CHAPTER 6

CONCLUSION

6.1. Summary

The research in this dissertation was motivated by the lack of any treatment of wing flexibility on the stability and flight performance of FWMAVs. The primary objective of this study, therefore, was to determine what effect introducing wing flexibility into a high fidelity model of flapping wing flight dynamics would have on the longitudinal open loop stability and the power requirements of a fruit fly scale robotic vehicle.

The performance and stability of a FWMAV was evaluated by creating a multi-fidelity flight simulator capable of using three different aerodynamic models: i) a quasi-steady model for rigid wings, ii) a fully validated 2D Navier Stokes solver capable of simulating pitching and plunging motion for rigid wings, and a iii) fully coupled, fully validated Navier Stokes – Euler Bernoulli beam solver, which determines both the instantaneous wing shape and the resulting aerodynamic forces and moments. These aerodynamic models were tightly coupled to the flight dynamics equations of motion. The coupling considers both the motion of the body in the calculation of aerodynamic forces as well as the inertia of the wings in determining the net forces acting on the body.

One of the most significant developments in this research is developing a trim algorithm in order to find the necessary control inputs and initial conditions to place the FWMAV in hovering equilibrium for both rigid and flexible wings. Equilibrium is defined such that average accelerations across a cycle are within an error tolerance of 3% of gravitational acceleration. We calculated power by directly measuring the moments and angular velocities associated with wing motion. We then averaged the positive power contributions in accordance with the consensus from the literature.

The most significant results from the research are that the FWMAV with the flexible wing exhibits open loop poles in hover that all have negative real parts whereas the rigid wing simulations for multiple pitch axes and also for biologically observed pitching motions have a set of poles with positive real parts. In other words, the flexible wings appear to provide stability to the FWMAV dynamic system that the rigid wings do not. This is a novel finding as most, if not all, rigid flapping wing studies have report a hover equilibrium with at least one pole with positive real part. The primary reason for the different behavior of the flexible wing system is precisely that the flexible wing structure can respond to perturbations while the rigid wing cannot. This increases the damping in two key stability derivatives, the horizontal velocity damping and the pitch rate damping that ultimately drive the poles into the left half of the complex plane. Additionally, in our rigid wing simulations, we demonstrated the destabilizing influence of wing wake interaction. The stability of flexible wings is facilitated because they experience significantly reduced wing wake interaction, which positively contributes to the lift generation as well as stability.

We also showed that the power requirements of a flexible wing are reduced for increasing frequency ratios (corresponding to decreasing stiffness). The lowest power we obtained for flexible wings was 23.1 W/kg, which is within the calculations made by biologists observing live fruit flies. Although this power is 36.8% larger than the best power prediction that we observed in our rigid wing simulations (16.9 W/kg), passive rotation of a flexible wing precludes the need for pitch actuation mechanisms and has the potential to reduce complexity and save on weight and power. Thus, wing flexibility has the potential to simplify FWMAV design while providing beneficial stability characteristics without prohibitive power penalties. Additionally, the reduced weight of flexible wings and the potential to relax the demands on an active controller might translate into higher performance such as increased range, endurance, payload, or agility over similar designs using rigid wings.

6.2. Original Contributions

In the course of this research, we made several innovations that are new to the technical community. We have also made several observations and conclusions that have not been previously reported concerning FWMAVs.

Novel contributions to the modeling of flapping wing flight dynamics include the following:

1.Development of a quasi-steady model that includes NS-informed rotational lift coefficients better representative of the actual rotation rates of insect wings as well as modeling of the pure aerodynamic moments generated from flapping wing motion.

2.Development of a fully coupled flight simulator that can model rigid and flexible wings, find equilibrium control inputs and initial conditions, and perform time-marching

simulations of flight while capture all relevant flow features, as well as wing and body dynamics.

3.Development and validation of a new trim algorithm to find equilibrium of this nonlinear, time varying system with coupled aerodynamics, structural dynamics and flight dynamics considered.

New discoveries, observations, and conclusions include:

1.Wing rotational forces significantly affect the flapping amplitude and power required to hover for rigid wings. Not properly accounting for this lift generation mechanism leads to erroneous predictions of required control inputs, required power, and stability characteristics.

2.Wing rotational forces significantly affect the flapping amplitude and power required to hover for flexible wings. Rotational mechanism enables flexible wings to create more lift during mid-stroke than the typical kinematics of rigid wings. This has not been previously observed or reported upon.

3.Wing wake interaction affects the flapping amplitude and power required to hover for both rigid and flexible wings. Not properly accounting for this nonlinear mechanism leads to erroneous predictions of required control inputs, required power, and stability characteristics.

4.A flexible wing responds to free flight body oscillations by modifying its wing shape, the rates of wing shape deformations and aerodynamic forces. This is the first time this has been modeled or observed. This implies that even in equilibrium (no perturbation), the wing's dynamics are coupled to the body dynamics, even for very high flapping frequencies.

5. A flexible wing responds to external perturbations by modifying its wing shape and the rates of wing shape deformations and aerodynamic forces, such that all open-loop poles are stabilizing. This is the first time this has been modeled or observed. The stabilizing effects of wing flexibility and the physical sources thereof primarily extend from two features of flexible wings which are not possible in rigid wings:

a. Flexible wings significantly reduce wing wake interaction, and therefore are not subject to the destabilizing influences of wing wake interaction.

b. The wing deformation itself can respond to the perturbed flow field in nontrivial ways that significantly increase the damping in key stability derivatives that ultimately return stable open loop poles. This deformation produces both modified passive pitch and pitch rates, which beneficially affect the stability.

6.3. Recommendations for Future Research

Although this research has answered some open questions of interest to the flapping wing community, there are several new directions that could be pursued. Also, there are several ways that the modeling in the current study could be improved upon.

One of the biggest simplifying assumptions made in the study is that we solve the 2D Navier Stokes equations on a 2D computational mesh. Repeating much of the research on a 3D wing could potentially yield more insights into the role of wing rotation and wing wake interaction in rigid wings. Furthermore, if a full 3D flexible wing model could be developed and coupled to the aerodynamics and flight dynamics, we could determine the influence of spanwise effects in both the flow and the structural dynamics.

Additionally, investigation of higher Reynolds number flight can be investigated. This could be valuable to those designing and prototyping FWMAVs since the state of manufacturing technology currently prevents construction of a true fruit fly sized vehicle.

Improving the beam model is another area of potential research. Our range of wing stiffness was limited by the ability of the linear solver to accurately represent the wing deformation. Considering a geometrically nonlinear structural dynamics model would address many of these issues and would allow for a more thorough search of the flexible design space.

Using the current flight simulator, several new directions could be pursued. Some insects are known to possess the musculature to change the pitch of the wings even though their wings are flexible. Additionally, insects utilize out of plane deviation angles in their flapping motion. The current model also permits active pitch in the context of wing flexibility and vertical deviation could easily be added to the wing kinematics. Combining these features would permit exploration of a different parametric design space. Using an out of plane deviation angle might also provide increased damping to the vertical degree of freedom, which our flexible wing model showed is now the least stable mode.

Several new directions could be explored by conducting full 6DOF simulations with the simulator. One of these includes determining the extent to which the lateral directional modes are affected by wing flexibility. Furthermore, adding additional wings to the simulation could be interesting. Additionally, forward flight, climbing, descending, and turning modes could be simulated and investigated, both using the QS

model and the NS model. If non-hover flight modes or the full 6DOF system is investigated, the aerodynamic forces on the body would need to be considered.

Having developed a multi-fidelity nonlinear flight dynamics model which includes both states and control inputs that can evolve in time, we are able to simulate the flight of a FWMAV. Therefore we are able to apply control strategies and determine their effectiveness in simulation. We have already successfully applied Lyapunov-based sliding mode control to stabilize the FWMAV in hover [122]. We used the quasi-steady model of a FWMAV with rigid wings, which is inherently unstable, and successfully rejected gusts up to 50% the flapping wing velocity, U [122]. There are several new directions that could be pursued to include testing if the sliding mode control strategy can accommodate wing damage as well as actuator uncertainty. Investigating other control strategies that have been recently developed for nonlinear systems is also of interest.

Finally, utilizing more advanced mathematical tools might yield further insights into the dynamics of the flexible wing system. Currently we evaluate the stability of the equilibrium point using linear analysis. Nonlinear analysis of this time-varying system might uncover novel dynamic features that insects may use or can be used for next-generation micro-air vehicles.

APPENDIX

A.1 Method of Solving the Navier Stokes Equations and Case Setup

The Navier Stokes equations are solved using an in-house two-dimensional, structured, pressure-based finite volume solver [123,124]. It employs implicit first or second order time stepping and treats the convection terms using the second order upwind-type scheme and the pressure and viscous terms using second order schemes. The geometric conservation law, a necessary consideration in domains with moving boundaries, is satisfied [125]. We use the radial basis function interpolation method to deform the computational mesh at each time step [118] in accordance with the prescribed kinematics.

The grid is a structured, rectangular grid with 102 points along the top and bottom of the airfoil, 13 points along the leading and trailing edges, and 102 points in the radial direction for a total of 113,424 points. The outer boundary of the domain is located 50 chord lengths from the wing. The wing section is also rectangular with a 2% thickness to chord ratio. The solver determines forces and moments at a rate of 480 time steps per flapping period. The boundary conditions are no-slip on the surface of the wing and extrapolated pressure at the boundary. The initial conditions are quiescent flow. The wing is moved at each time step in accordance with the prescribed wing kinematics and body motion.

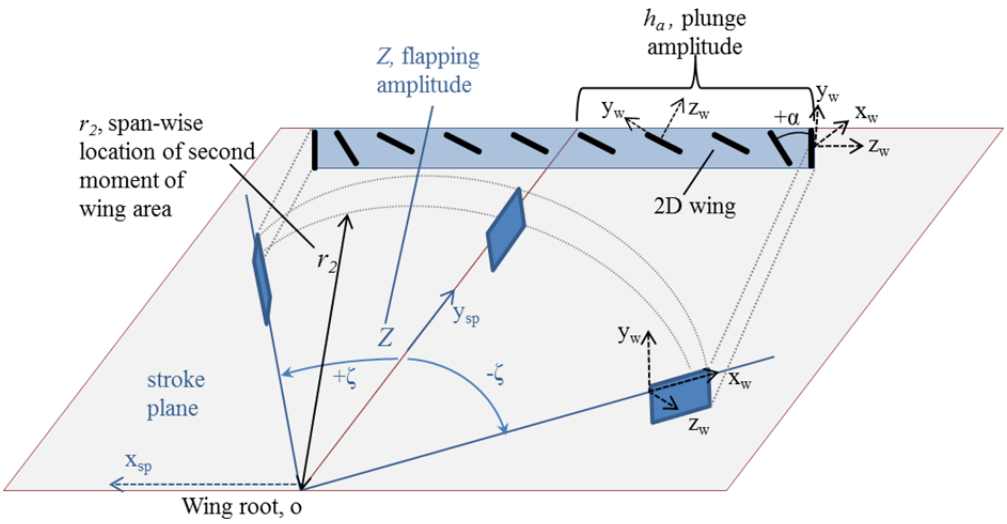

Figure A.1. Visual depiction of the 3D flapping motion and the 2D plunging motion used to model wing flapping in the 2D Navier Stokes solver.

The three-dimensional flapping is converted to a two-dimensional plunge motion in order to facilitate the solution of the Navier Stokes equations in two dimensions. The arc length of the second moment of wing area is set equal to the plunge amplitude h_a, according to $h_a = Zr_2$ and Figure A.1.

A.2 Grid and time step convergence

In order to assess the effects of grid resolution and time step size at the fruit fly scale at Re=1×10^3, grid and time step convergence studies were conducted to determine the optimal grid resolution, domain size, and time step.

A motion based on Xiong and Sun [15] was prescribed on the rigid wing. A no-slip boundary condition was prescribed on the flat plate surface, and outer boundaries of the domain were set as inlet. A rectangular domain showed a better convergence rate and fewer velocity-pressure coupling iterations per time step than a circular domain. After

assessing the effects of domain shape and domain size, we found that a rectangular domain with outer boundary at 50 chords lengths in the direction normal to the wing had an optimal distribution (see Figure A.2). Lift histories for each grid are provided in Figure A.3.

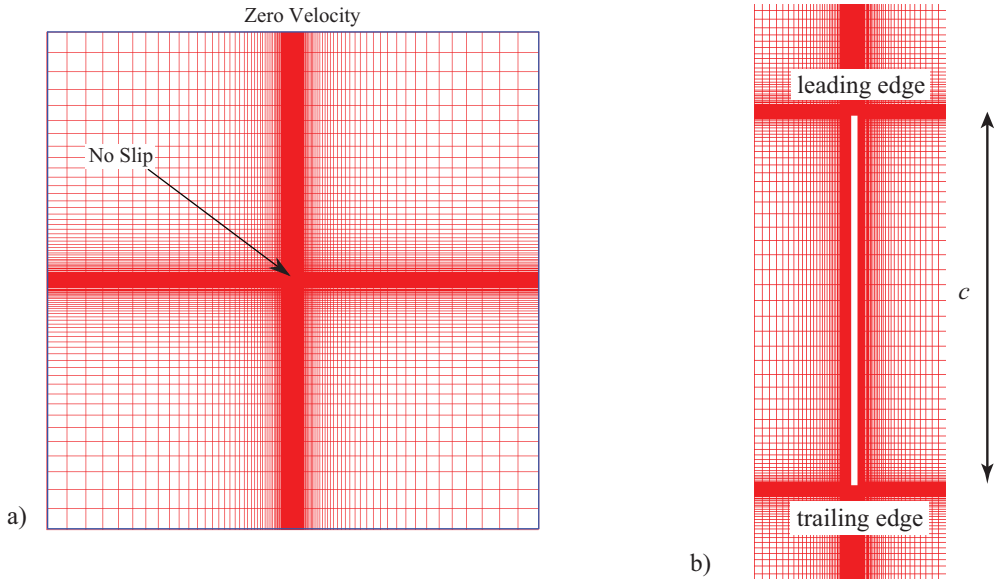

Figure A.2. Overview of the computational mesh for 61×101 grid. (a) Computational domain and boundary conditions. (b) Zoomed in view of the mesh around the flat plate shows the rectangular computational domain around the flat plate.

Four levels of grids were created ranging from a coarse to extra-fine grid with resolutions 31×51, 61×101, 121×201 and 241×401 respectively. In comparison, Xiong and Sun [15] used a three dimensional O-H type computational grid with the outer boundary fixed at 20 chord lengths from the wing and 71×73×96 points in the normal direction, along the body axis and in the azimuthal direction, respectively. Convergence was assessed systematically based on the error norms of lift coefficient C_L over two motion cycles with the solution on the 241×401 grid considered as an estimate of the exact solution. The L_1 and L_2 norms were calculated with 480 time steps per motion cycle

per equation (A.1), where k indicates the mesh level and N is 480, the total number of time steps over which the norm is calculated. Based on the L_1 and L_2, tabulated in Table A.1, we chose 121×201 grid for all Navier-Stokes equation computations.

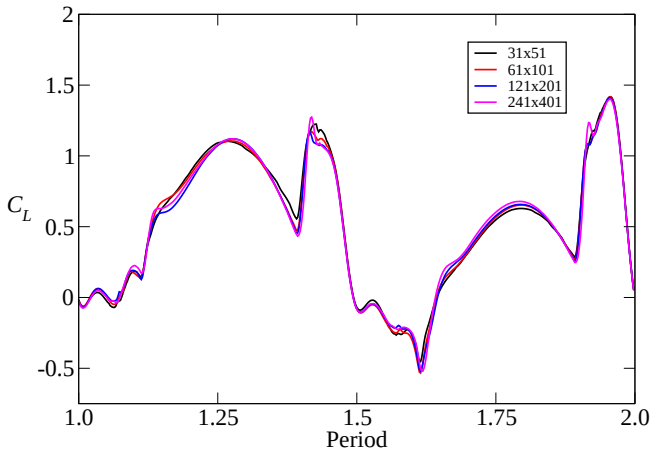

Figure A.3. The lift history over one motion cycle for four grid levels shown in Table A.1.

$$L_1\text{norm}_k = \sum_{n=1}^{N} | f_{k,n} - \tilde{f}_{exact,n} | \Big/ N \qquad L_2\text{norm}_k = \left(\sum_{n=1}^{N} | f_{k,n} - \tilde{f}_{exact,n} |^2 \Big/ N \right)^{\frac{1}{2}} \tag{A.1}$$

Time sensitivity was also performed in the same manner on the 121×201 grid. Four levels of time steps per motion cycle were chosen: 240, 480, 960, and 1920. The criteria for assessing temporal convergence was based on the L_1 and the L_2 norms of lift coefficient C_L with solution at 1920 time steps per motion cycle considered as the most accurate solution. Based on the convergence seen in Table A.1, 960 time steps per flapping cycle were considered for all computations.

Table A.1. Spatial and temporal sensitivity study at fruit fly scale.

	L_1 Norm of C_L	L_2 Norm of C_L

Spatial	31×51	0.060	0.085
	61×101	0.034	0.051
	121×201	0.022	0.035
	241×401 (baseline)		
Temporal (time steps)	240	0.496	3.90
	480	0.311	2.57
	960	0.152	1.40
	1920 (baseline)		

A.3 Discussion regarding wing kinematics

The kinematics used by Sun and coworkers [15,35] and also Park and Choi [126] are intuitive because they express the timing of wing rotation in terms of the percent of the flapping cycle, $\Delta\tau_R$. However, we were unable to use these expressions because they result in non-smooth accelerations. When this motion was provided to the NS solver in our study, the discontinuity in acceleration produced unwanted and most likely nonphysical oscillations in the forces. These oscillations do not occur with Berman and Wang [4] kinematics because their expressions are infinitely differentiable. In order to translate the commonly used $\Delta\tau_R$ into the smoothing parameter C_α the equation (A.2) is used.

$$C_\alpha = -10.267\Delta\tau_R + 5.1578 \tag{A.2}$$

A.4 Regarding the calculation of the rotational lift coefficient

When calculating rotational lift, the rotational force coefficient is an important parameter. Bisplinghoff [97] demonstrated that the theoretical value of $C_{rot} = -\pi(0.75 - x_p/c)$. On the other hand, Sane and Dickinson [27] showed that for low Reynolds number flows, the value of C_{rot} is also function of the nondimensional rotational velocity

$\hat{\omega} = \omega c / U_{tip}$. In their experiments, they systematically vary $\hat{\omega}$ between 0.374 and 0.166 and demonstrate that the corresponding C_{rot} varies between 0 and 2.7 as a function of both $\hat{\omega}$ and x_p/c. Taking a linear regression of their data yields a purely experimentally based value of $C_{rot,exp}$ = (-11.77 $\hat{\omega}$ + 0.8152)(0.75- x_p/c).

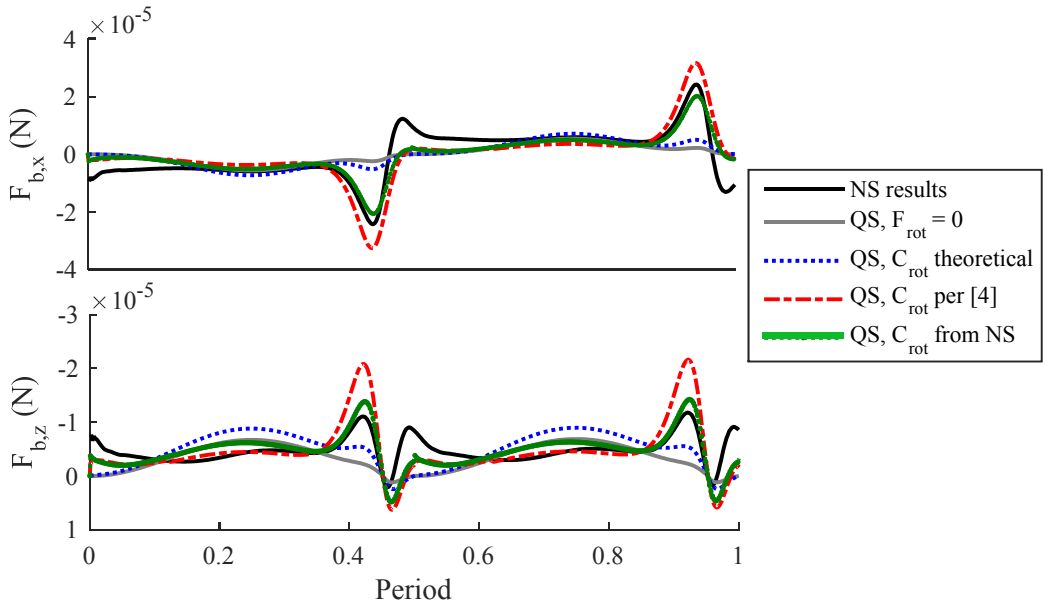

Figure A.4. Comparison of the NS solution to various QS models with and without rotational lift.

Using Sane and Dickinson's [27] $C_{rot,exp}$ directly in our simulations, however, caused a significant over-prediction in the rotational forces generated, as illustrated by the red dash-dotted line in Figure A.4. The reason for this is that we typically obtain $\hat{\omega}$ in the range of 0.5 to 1.75, which lies completely outside the range of $\hat{\omega}$ reported in Sane and Dickinson [27]. Ellington [127] reported that real insects also exhibit $\hat{\omega}$ between 0.64 and 1.44, which is much larger than the range studied by Sane and Dickinson [27]. In order to account for this, we modified Sane and Dickinson's [27] prediction of $C_{rot,exp}$ by comparing it against numerous NS simulations, where we found that the following

expression yielded much better agreement with the NS results across a range of rotational velocities and pitch axes: $C_{rot} = (-11.77\,\hat{\omega} + 0.8152)(0.871x_p/c + 0.17125)(0.75 - x_p/c)$. This is illustrated in Figure A.4 with the green line.

A.5 Calculation of Wing Inertia while Varying the Pitch Axis Location

Properly determining the wing inertia is important in accurately predicting the power required since wing inertia is such a large contributor to power for flapping wing designs. The inertia tensor for a three dimensional body can have up to six unique terms that describe three moments of inertia, I_{xx}, I_{yy}, and I_{zz}, and three products of inertia, I_{xy}, I_{yz}, I_{xz}. The values of wing inertia from actual insects are given in several sources, but care must be taken to ensure that the inertia is tracked properly about the correct axis, and about the proper location (about the CG vs. the wing root). We define the wing inertia about the wing root in terms of the wing reference frame so that the inertia is not a function of time. Due to the various presentations of the inertia matrix in textbooks on rigid body dynamics, we will specifically detail our usage here. We follow the convention used in Ginsberg [128] for the inertia matrix, equation (A.3), that allows the angular momentum vector **H** to be described by equation (A.4).

$$I = \begin{bmatrix} I_{xx} & -I_{xy} & -I_{xz} \\ -I_{yx} & I_{yy} & -I_{yz} \\ -I_{zx} & -I_{zy} & I_{zz} \end{bmatrix}, \quad I_{xy} = I_{yx} = \iiint xydm \tag{A.3}$$

$$\mathbf{H} = I\boldsymbol{\omega} \tag{A.4}$$

Based on our wing-fixed reference frame, the pitching and flapping moments of inertia are I_{xx} and I_{yy} respectively. Ellington [88] gives the flapping inertia (i.e. second

moment of mass about the flapping axis) as $I_{w/o,flapping} = m_w R^2 \hat{r}_2^2(m)$ = (0.0052)(175×10^{-6} kg)(13.2mm)^2(0.44)^2 = 3.07×10^{-11} kg-m^2. Then we take the ratio of I_{pitch}/I_{flap} = 0.04358 that Wu and Sun [17] report for the drone fly, which has a wing of similar shape. We assume that this is the value of pitch inertia that goes through the CG of the wing: I_{xx} = 1.338×10^{-12} kg-m^2. For situations where the pitch axis does not coincide with the wing CG, we use the parallel axis theorem to adjust the pitch inertia. The I_{zz}, which corresponds to the inertia associated with angular deviation can be calculated using the perpendicular axis theorem.

There is a plane of symmetry in the *x*-*y* plane of the wing, which means that I_{xz} = I_{yz} = 0. However, the product of inertia I_{xy} is nonzero. As such, the flapping acceleration will affect the pitch acceleration. Given the proper kinematics and a large enough I_{xy}, it is possible to achieve passive pitch rotation simply due to flapping motion. We calculate I_{xy} = -1.45×10^{-13} kg-m^2 about the axis that intersects the wing CG from Ennos's wing planform and mass distribution [45]. We then apply the parallel axis theorem for products of inertia to get $I_{xy,o}$, about the wing root when the pitch axis does not coincide with the wing CG. Note that this results in a negative value for $I_{xy,o}$ when the CG of the wing is co-located with or behind the pitch axis (and when substituted in the inertia matrix, makes all terms positive). However, as the pitch axis moves away from the wing CG, the pitch inertia itself, I_{xx}, also increases.

We also provide a graphical depiction of the relative location of the wing CG, the pitch axis, the wing aerodynamic center in Figure A.5. As the pitch axis location changes, we simultaneously adjust the distance of the wing root above the body CG in order to maintain a consistent vertical offset between the aerodynamic center and the

body CG. Not doing so would potentially obscure the aerodynamic features of adjusting the pitch axis by changing the moments produced by the aerodynamic forces.

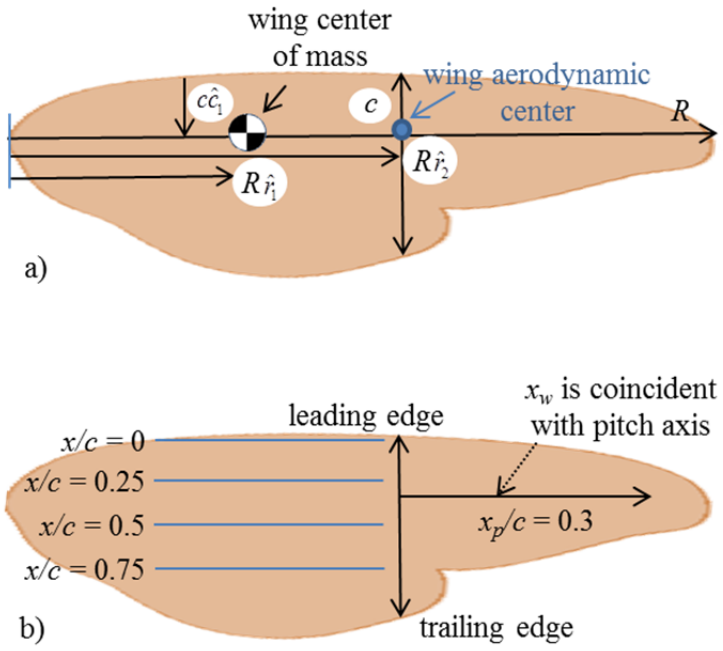

Figure A.5. Planform of wing with relative position of wing center of mass and wing aerodynamic center (a) which are assumed constant for all simulations. The pitch axis (b) is systematically changed in the course of the study, which affects the wing inertia.

A.6 Detailed Listing of Reference Frames and Transformation Matrices

Due to the number of reference frames used in this dissertation, they are concisely summarized in Table A.2.

Combining the individual rotation matrices into commonly used transformations is convenient. We define the transformation from the body to the wings as follows

$$R_{b\to w} = R_\alpha R_\delta R_\zeta R_{sp\to usp} R_\beta =$$

$$\begin{bmatrix} c_\beta c_\delta s_\zeta - s_\beta s_\delta & c_\delta c_\zeta & -c_\beta s_\delta - s_\beta c_\delta s_\zeta \\ -c_\beta\left(s_\alpha c_\zeta + c_\alpha s_\delta s_\zeta\right) - c_\alpha c_\delta s_\beta & s_\alpha s_\zeta - c_\alpha s_\delta c_\zeta & s_\beta\left(s_\alpha c_\zeta + c_\alpha s_\delta s_\zeta\right) - c_\alpha c_\delta c_\beta \\ c_\delta s_\alpha s_\beta - c_\beta\left(c_\alpha c_\zeta - s_\alpha s_\delta s_\zeta\right) & c_\alpha s_\zeta + s_\alpha s_\delta c_\zeta & s_\beta\left(c_\alpha c_\zeta - s_\alpha s_\delta s_\zeta\right) + s_\alpha c_\delta c_\beta \end{bmatrix} \quad \text{(A.5)}$$

Additionally, the transformation from the wing to the body is given by

$$R_{w\to b} = R_\beta^T R_{sp\to usp}^T R_\zeta^T R_\delta^T R_\alpha^T \quad \text{(A.6)}$$

Since the body rotations happen in their own local frame, they require their own rotation matrix, which is a rate transformation matrix and is denoted by $R_{\omega\to b}$ in equation (A.7).

$${}_b\boldsymbol{\omega}_{b/I} = \begin{bmatrix} p \\ q \\ r \end{bmatrix} = R_{\omega\to b}\begin{bmatrix} \dot\phi \\ \dot\theta \\ \dot\psi \end{bmatrix} = \begin{bmatrix} 1 & 0 & -\sin\theta \\ 0 & \cos\phi & \sin\phi\cos\theta \\ 0 & -\sin\phi & \cos\phi\cos\theta \end{bmatrix}\begin{bmatrix} \dot\phi \\ \dot\theta \\ \dot\psi \end{bmatrix} \quad \text{(A.7)}$$

Additionally, it is important to relate the angular rates in the inertial frame. Thus, the rate transformation matrix must be inverted to yield equation (A.8) also per Etkin [89]

Table A.2. Summary of reference frames, rotation angles, and rotation matrices used in this study.

Name of Frame	Sequence	Rotations about	by	Transformation Matrix

Inertial (Z down, X north)	I	n/a	n/a	n/a
	1	z_I and z_1	ψ	$R_\psi = \begin{bmatrix} \cos\psi & \sin\psi & 0 \\ -\sin\psi & \cos\psi & 0 \\ 0 & 0 & 1 \end{bmatrix}$
	2	y_1 and y_2	θ	$R_\theta = \begin{bmatrix} \cos\theta & 0 & -\sin\theta \\ 0 & 1 & 0 \\ \sin\theta & 0 & \cos\theta \end{bmatrix}$
Body	3	x_2 and x_3	φ	$R_\phi = \begin{bmatrix} 1 & 0 & 0 \\ 0 & \cos\phi & \sin\phi \\ 0 & -\sin\phi & \cos\phi \end{bmatrix}$
Stroke Plane	4	y_3 and y_4	β	$R_\beta = \begin{bmatrix} \cos\beta & 0 & -\sin\beta \\ 0 & 1 & 0 \\ \sin\beta & 0 & \cos\beta \end{bmatrix}$
Upright Stroke Plane	5	All axes swapped		$R_{sp\to usp} = \begin{bmatrix} 0 & 1 & 0 \\ 0 & 0 & -1 \\ -1 & 0 & 0 \end{bmatrix}$
	6	y_{usp} and y_6	ζ	$R_\zeta = \begin{bmatrix} \cos\zeta & 0 & -\sin\zeta \\ 0 & 1 & 0 \\ \sin\zeta & 0 & \cos\zeta \end{bmatrix}$
	7	z_6 and z_7 (z_{usp}')	δ	$R_\delta = \begin{bmatrix} \cos\delta & \sin\delta & 0 \\ -\sin\delta & \cos\delta & 0 \\ 0 & 0 & 1 \end{bmatrix}$
Right wing frame	8	x_7 and x_8 (x_{usp}'')	α	$R_\alpha = \begin{bmatrix} 1 & 0 & 0 \\ 0 & \cos\alpha & \sin\alpha \\ 0 & -\sin\alpha & \cos\alpha \end{bmatrix}$

$$ {}_I\begin{bmatrix} \dot{\phi} \\ \dot{\theta} \\ \dot{\psi} \end{bmatrix} = \begin{bmatrix} 1 & \sin\phi\tan\theta & \cos\phi\tan\theta \\ 0 & \cos\phi & -\sin\phi \\ 0 & \sin\phi\sec\theta & \cos\phi\sec\theta \end{bmatrix} \begin{bmatrix} p \\ q \\ r \end{bmatrix} \tag{A.8} $$

A similar process must be applied between the wing and the body rates in order to express the wing rates in the wing frame or the body frame. The rate transformation matrix that allows wing rotational velocities to be expressed in the wing frame is

$$R_{\omega\to w} = \begin{bmatrix} 1 & \mathrm{s}_\delta & 0 \\ 0 & \mathrm{c}_\delta \mathrm{c}_\alpha & \mathrm{s}_\alpha \\ 0 & -\mathrm{c}_\delta \mathrm{s}_\alpha & \mathrm{c}_\alpha \end{bmatrix} \tag{A.9}$$

and its derivative, which is needed in determining the angular acceleration of the wing, is given by

$$\dot{R}_{\omega\to w} = \begin{bmatrix} 0 & \dot{\delta}\,\mathrm{c}_\delta & 0 \\ 0 & -\dot{\delta}\,\mathrm{s}_\delta \mathrm{c}_\alpha - \dot{\alpha}\,\mathrm{c}_\delta \mathrm{s}_\alpha & \dot{\alpha}\,\mathrm{c}_\alpha \\ 0 & \dot{\delta}\,\mathrm{s}_\delta \mathrm{s}_\alpha - \dot{\alpha}\,\mathrm{c}_\delta \mathrm{c}_\alpha & -\dot{\alpha}\,\mathrm{s}_\alpha \end{bmatrix} \tag{A.10}$$

A.7 Discussion Regarding Equations of Motion

The acceleration of the wing's center of mass, expressed in the body frame, is given by equation (A.11)

$$\begin{aligned} {}_b\mathbf{a}_{wg/I} = {}& {}_b\mathbf{a}_{cg} + {}_b\boldsymbol{\omega}_b \times {}_b\mathbf{v}_{cg} + {}_b\dot{\boldsymbol{\omega}}_b \times {}_b\mathbf{r}_{o/cg} + {}_b\boldsymbol{\omega}_b \times {}_b\boldsymbol{\omega}_b \times {}_b\mathbf{r}_{o/cg} \\ & + R_{w\to b}\left({}_w\mathbf{a}_{wg/o} + 2\,{}_w\boldsymbol{\omega}_w \times {}_w\mathbf{v}_{wg/o} + {}_w\dot{\boldsymbol{\omega}}_w \times {}_w\mathbf{r}_{wg/o\ w} + {}_w\boldsymbol{\omega}_w \times {}_w\boldsymbol{\omega}_w \times {}_w\mathbf{r}_{wg/o} \right) \end{aligned} \tag{A.11}$$

We need to express equation (A.11) in a way that isolates those components that have second order derivatives of the state variables, which then becomes equation (A.12)

where the double underlined terms are those that contain state derivatives and need to be isolated, and the single underlined terms arise from flexible motion of the wing, but are otherwise zero.

$$
\begin{aligned}
{}_b\mathbf{a}_{wg/I} = {} & \underline{\underline{{}_b\dot{\mathbf{v}}_{cg} - \left({}_b\mathbf{r}_{o/cg} \times {}_b\dot{\boldsymbol{\omega}}_b + \left(R_{w\to b}\, {}_w\mathbf{r}_{wg/o} \right) \times {}_b\dot{\boldsymbol{\omega}}_b \right)}} \\
& + R_{w\to b} \left[\begin{array}{c} \left(R_{b\to w} \begin{bmatrix} p \\ q \\ r \end{bmatrix} \times R_{\omega\to w} \begin{bmatrix} \dot{\alpha} \\ \dot{\zeta} \\ \dot{\delta} \end{bmatrix} + \dot{R}_{\omega\to w} \begin{bmatrix} \dot{\alpha} \\ \dot{\zeta} \\ \dot{\delta} \end{bmatrix} + R_{\omega\to w} \begin{bmatrix} \ddot{\alpha} \\ \ddot{\zeta} \\ \ddot{\delta} \end{bmatrix} \right) \\ \times {}_w\mathbf{r}_{wg/o} + {}_w\boldsymbol{\omega}_w \times {}_w\boldsymbol{\omega}_w \times {}_w\mathbf{r}_{wg/o} \end{array} \right] \\
& + {}_b\boldsymbol{\omega}_b \times {}_b\mathbf{v}_{cg} + {}_b\boldsymbol{\omega}_b \times {}_b\boldsymbol{\omega}_b \times {}_b\mathbf{r}_{o/cg} + R_{w\to b} \left[\underline{{}_w\dot{\mathbf{v}}_{wg/o} + 2\, {}_w\boldsymbol{\omega}_w \times {}_w\mathbf{v}_{wg/o}} \right]
\end{aligned}
\tag{A.12}
$$

The first line of equation (A.12) can be rearranged to equation (A.13) which allows for insertion into *H*, which is the mass matrix that must be inverted to isolate $\dot{u} \quad \dot{v} \quad \dot{w} \quad \dot{p} \quad \dot{q} \quad \dot{r}$ per equation (A.13)

$$
\begin{bmatrix} \dot{u} \\ \dot{v} \\ \dot{w} \end{bmatrix} - \left(\begin{bmatrix} 0 & -z_{o/cg} & y_{o/cg} \\ z_{o/cg} & 0 & -x_{o/cg} \\ -y_{o/cg} & x_{o/cg} & 0 \end{bmatrix} + R_{w\to b} \begin{bmatrix} 0 & -z_{wg/o} & y_{wg/o} \\ z_{wg/o} & 0 & -x_{wg/o} \\ -y_{wg/o} & x_{wg/o} & 0 \end{bmatrix} R_{w\to b}^T \right) \begin{bmatrix} \dot{p} \\ \dot{q} \\ \dot{r} \end{bmatrix} \tag{A.13}
$$

Substituting these expanded relationships into the equations of motion results in equations (3.18) and (3.19), which represent the full equations of motion for the multibody model of the insect for the linear and angular force-acceleration balance. Although the terms are grouped differently, they are the same relations presented by Wu, Zhang, and Sun [17]. In this form, equations can be expressed as equation (A.14) where

H is a 6x6 matrix, defined by equation (A.15) and the right hand sides (RHS) of equations (3.18) and (3.19) are not repeated in equation (A.14).

$$\begin{bmatrix} \dot{u} \\ \dot{v} \\ \dot{w} \\ \dot{p} \\ \dot{q} \\ \dot{r} \end{bmatrix} = [H]^{-1} \begin{bmatrix} RHS\ of\ equation\ 3.18 \\ RHS\ of\ equation\ 3.19 \end{bmatrix} \tag{A.14}$$

$$[H] = \begin{bmatrix} m_{tot}[I_{3x3}] & \left[\sum_{i=1}^{\#wings} m_{w,i}\left(\tilde{r}_{o/cg,i} + {}_{w,i\to b}R\,\tilde{r}_{wg/o,i}\,{}_{w,i\to b}R^{T}\right)\right] \\ \left[\sum_{i=1}^{\#wings} m_{w,i}\left(\tilde{r}_{o/cg,i} + {}_{w,i\to b}R\,\tilde{r}_{wg/o,i}\,{}_{w,i\to b}R^{T}\right)\right] & \begin{bmatrix} {}_{b}\underline{I}_{b,cg} + {}_{w,i\to b}R\,{}_{w}\underline{I}_{wg}\,{}_{w,i\to b}R^{T} - \\ \sum_{i=1}^{\#wings} m_{w,i}\,{}_{w,i\to b}R\,\tilde{r}_{wg/o,i}\,{}_{w,i\to b}R^{T}\,{}_{b}\tilde{r}_{o/cg,i} \\ -\sum_{i=1}^{\#wings} m_{w,i}\tilde{r}_{o/cg,i}\left(\tilde{r}_{o/cg,i} + {}_{w,i\to b}R\,\tilde{r}_{wg/o,i}\,{}_{w,i\to b}R^{T}\right) \end{bmatrix} \end{bmatrix} \tag{A.15}$$

A.8 Full Coupling of the Flight Dynamics to the Fluid-Structure Interaction

An important reason that tight coupling is required in this study is the spurious nature of the solution when larger intervals are used for integrating the equations of motion. In Fig. 14 we demonstrate the effect of averaging the forces prior to applying them to the equations of motion at a sampling frequency less than that of the fluid-structure simulation. Other researchers have also discussed different averaging methods, most notably Orlowski and Girard[11], who recommend using quarter-cycle averaging in lieu of full-cycle averaging. Our attempts to apply any kind of averaging other than

coupling the equation of motion to the high fidelity fluid solution at each step resulted in non-smooth, spiky force responses. Figure 15 shows the effect of integrating the equations of motion every four time steps and every eight time steps, which is still much more tightly coupled than quarter-cycle averaging. The introduction of the body displacement every four or eight time steps produced significant forces and caused the oscillations in the numerical solution that are seen in Figure A.6.

A potential cause for the peaks in the aerodynamic forces is that the change in the body displacement from the equation of motion into the Navier-Stokes equation solver increases with the length of the averaging intervals. Conserving the momentum of the fluid under these large body displacements causes significant changes in the pressure distribution around the wing, resulting in the force spikes. This is seen for 20 time steps of the solution in Figure A.7. When the body displacements are provided to the FSI routine every time step, the change in the wing displacement is smooth and therefore the numerical derivatives of that motion are also smooth. If the body displacements are provided less frequently (e.g. every four steps), the additional change in the position of the wing at the fourth step, though small compared to the plunge displacements, causes the velocity and acceleration to exhibit non-physical spikes due to the averaging. These force spikes disappear when the Navier-Stokes equation solver and the equation of motion are coupled at every time step.

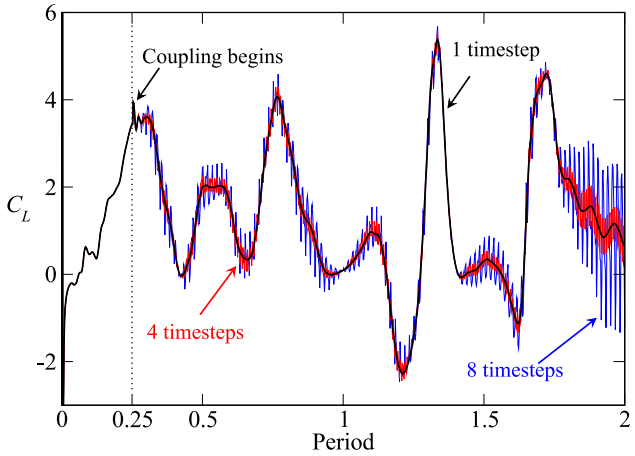

Figure A.6. Effect of integrating the equations of motion over longer time intervals than the CFD-CSD solver. Introducing displacements in 4-step or 8-step intervals introduces the forces spikes (red and blue lines).

On the other hand, a quasi-steady aerodynamics model assumes that the forces and moments depend on the instantaneous wing velocities and accelerations. The relation between the force coefficients and the wing motion is partly based on the linearized aerodynamic theories and in part on empirically obtained parameters. These quasi-steady models neglect history effects, under-representing wing wake interactions that are typical to hovering insects. As a consequence, a flight dynamics framework coupled to a quasi-steady aerodynamics model may seem to be more robust as it does not account for the flow physics occured at earlier time instances. However, the apparent robustness also suggests that the solution from a quasi-steady model may be artificial, not satisfying the first principles of physics under certain conditions. Assessment of the accuracy of the use of the quasi-steady models in the flight dynamics modeling is one of our future studies.

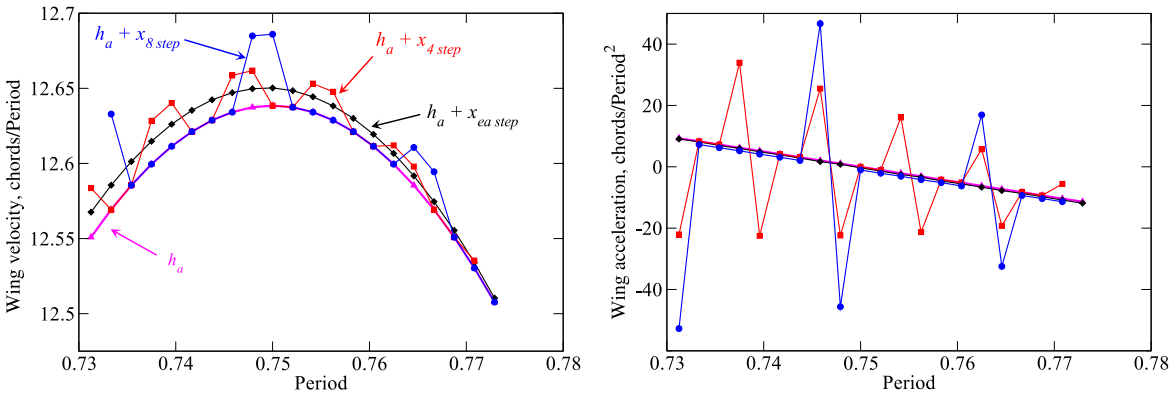

a) **b)**

Figure A.7. Velocity (a) and acceleration (b) of the wing using the following intervals between integrating the equations of motions: 1 step, 4 steps, and 8 steps. The parameter, h_a, is the translation of the wing due solely to flapping.

REFERENCES

1. Kang C-K, Shyy W. Scaling law and enhancement of lift generation of an insect-size hovering flexible wing. J R Soc Interface. 2013;10(85):20130361.

2. Kang C-K, Shyy W. Analytical model for instantaneous lift and shape deformation of an insect-scale flapping wing in hover. J R Soc Interface. 2014; 11(101):20140933.

3. Theodorsen T. General theory of aerodynamic instability and the mechanism of flutter. NACA Rep 496. 1935.

4. Berman GJ, Wang ZJ. Energy-minimizing kinematics in hovering insect flight. J Fluid Mech. 2007;582:153–68.

5. Taha HE, Hajj MR, Nayfeh AH. Longitudinal Flight Dynamics of Hovering MAVs/Insects. J Guid Control Dyn. 2014;37(3):970–9.

6. Taha HE, Hajj MR, Nayfeh AH. Flight dynamics and control of flapping-wing MAVs: a review. Nonlinear Dyn. 2012;70(2):907–39.

7. Sun M. Insect flight dynamics: Stability and control. Rev Mod Phys. 2014;86(2):615–46.

8. Cheng B, Deng X. Translational and rotational damping of flapping flight and its dynamics and stability at hovering. IEEE Trans Robot. 2011;27(5):849–64.

9. Faruque I, Humbert JS. Dipteran insect flight dynamics. Part 1 Longitudinal motion about hover. J Theor Biol. 2010;264(2):538–52.

10. Orlowski CT, Girard AR. Dynamics, stability, and control analyses of flapping wing micro-air vehicles. Prog Aerosp Sci. 2012;51:18–30.

11. Orlowski CT, Girard AR. Modeling and simulation of nonlinear dynamics of flapping wing micro air vehicles. AIAA J. 2011;49(5):969–81.

12. Kang C-K, Aono H, Cesnik CES, Shyy W. Effects of flexibility on the aerodynamic performance of flapping wings. J Fluid Mech. 2011;689:32–74.

13. Sridhar MK, Kang C. Aerodynamic performance of two-dimensional, chordwise flexible flapping wings at fruit fly scale in hover flight. Bioinspir Biomim. 2015;10(3):1–14.

14. Orlowski CT, Girard AR. Longitudinal Flight Dynamics of Flapping-Wing Micro Air Vehicles. J Guid Control Dyn. 2012;35(4):1115–31.

15. Sun M, Xiong Y. Dynamic flight stability of a hovering bumblebee. J Exp Biol. 2005;208(3):447–59.

16. Sun M, Wang JK, Xiong Y. Dynamic flight stability of hovering insects. Acta Mech Sin. 200723(3):231–46.

17. Wu JH, Zhang Y-L, Sun M. Hovering of model insects: simulation by coupling equations of motion with Navier-Stokes equations. J Exp Biol. 2009;212(20):3313–29.

18. Liang B, Sun M. Nonlinear flight dynamics and stability of hovering model insects Nonlinear flight dynamics and stability of hovering model insects. J R Soc Interface. 2013;10(85):20130269.

19. Combes SA, Daniel TL. Flexural stiffness in insect wings I. Scaling and the influence of wing venation. J Exp Biol. 2003;206(17):2979–87.

20. Combes SA, Daniel TL. Flexural stiffness in insect wings II. Spatial distribution and dynamic wing bending. J Exp Biol. 2003;206(17):2989–97.

21. Shyy W, Aono H, Chimakurthi SK, Trizila P, Kang C, Cesnik CES, et al. Recent progress in flapping wing aerodynamics and aeroelasticity. Prog Aerosp Sci. 2010;46(7):284–327.

22. Shyy W, Aono H, Kang C, Liu H. An Introduction to Flapping Wing Aerodynamics. Cambridge University Press, New York, USA; 2013.

23. Sane SP. The aerodynamics of insect flight. J Exp Biol. 2003;206(23):4191–208.

24. Ansari SA, Żbikowski R, Knowles K. Aerodynamic modelling of insect-like flapping flight for micro air vehicles. Prog Aerosp Sci. 2006;42(2):129–72.

25. Dickinson MH, Lehmann F-O, Sane SP. Wing Rotation and the Aerodynamic Basis of Insect Flight. Science. 1999;284:1954–60.

26. Sane SP, Dickinson MH. The control of flight force by a flapping wing: lift and drag production. J Exp Biol. 2001;204:2607–26.

27. Sane SP, Dickinson MH. The aerodynamic effects of wing rotation and a revised

quasi-steady model of flapping flight. J Exp Biol. 2002;205(8):1087–96.

28. Liu H, Ellington CP, Kawachi K, Van Den Berg C, Willmott AP. A computational fluid dynamic study of hawkmoth hovering. J Exp Biol. 1998;201:461–77.

29. Sun M, Tang J. Unsteady aerodynamic force generation by a model fruit fly wing in flapping motion. J Exp Biol. 2002;205(1):55–70.

30. Tang J, Viieru D, Shyy W. Effects of Reynolds Number and Flapping Kinematics on Hovering Aerodynamics. AIAA J. 2008;46(4):967–76.

31. Trizila P, Kang C-K, Aono H, Shyy W, Visbal M. Low-Reynolds-Number Aerodynamics of a Flapping Rigid Flat Plate. AIAA J. 2011;49(4):806–23.

32. Fry SN, Sayaman R, Dickinson MH. The aerodynamics of hovering flight in Drosophila. J Exp Biol. 2005;208(12):2303–18.

33. Altshuler DL, Dickson WB, Vance JT, Roberts SP, Dickinson MH. Short-amplitude high-frequency wing strokes determine the aerodynamics of honeybee flight. Proc Natl Acad Sci. 2005;102(50):18213–8.

34. Gao N, Aono H, Liu H. Perturbation analysis of 6DoF flight dynamics and passive dynamic stability of hovering fruit fly Drosophila melanogaster. J Theor Biol. 2011;270(1):98–111.

35. Meng XG, Xu L, Sun M. Aerodynamic effects of corrugation in flapping insect wings in hovering flight. J Exp Biol. 2011;300:432–44.

36. Wang ZJ, Birch JM, Dickinson MH. Unsteady forces and flows in low Reynolds number hovering flight: two-dimensional computations vs robotic wing experiments. J Exp Biol. 2004;207(Pt 3):449–60.

37. Bergou AJ, Xu S, Wang ZJ. Passive wing pitch reversal in insect flight. J Fluid Mech. 2007;591:321–37.

38. Wu JH, Sun M. Unsteady aerodynamic forces and power requirements of a bumblebee in forward flight. Acta Mech Sin. 2005;21(3):207–17.

39. Zhang Y-L, Sun M. Dynamic flight stability of hovering model insects: theory versus simulation using equations of motion coupled with Navier-Stokes equations. Acta Mech Sin. 2010;26(4):509–20.

40. Sun M, Wang JK. Flight stabilization control of a hovering model insect. J Exp Biol. 2007;210(Pt 15):2714–22.

41. Faruque I, Humbert JS. Dipteran insect flight dynamics. Part 2: Lateral–directional

motion about hover. J Theor Biol. 2010;265(3):306–13.

42. Humbert JS, Faruque I. Analysis of Insect-Inspired Wingstroke Kinematic Perturbations for Longitudinal Control. J Guid Control Dyn. 2011;34(2):618–23.

43. Whitney JP, Wood RJ. Aeromechanics of passive rotation in flapping flight. J Fluid Mech. 2010;660:197–220.

44. Dudley R, Ellington CP. Mechanics of Forward Flight in Bumblebees: I. Kinematics and Morphology. J Exp Biol. 1990;148(1):19–52.

45. Ennos AR. The inertial cause of wing rotation in Diptera. J Exp Biol. 1988;140(1):161–169.

46. Madangopal R, Khan ZA, Agrawal SK. Biologically Inspired Design Of Small Flapping Wing Air Vehicles Using Four-Bar Mechanisms And Quasi-steady Aerodynamics. J Mech Des. 2005;127(4):809.

47. Khan ZA, Agrawal SK. Optimal Hovering Kinematics of Flapping Wings for Micro Air Vehicles. AIAA J. 2011;49(2):257–68.

48. Ishihara D, Horie T, Denda M. A two-dimensional computational study on the fluid-structure interaction cause of wing pitch changes in dipteran flapping flight. J Exp Biol. 2009;212(Pt 1):1–10.

49. Gerdes JW, Gupta SK, Wilkerson SA. A review of bird-inspired flapping wing miniature air vehicle designs. J Mech Robot. 2012;4(2):21003.

50. Wu P, Stanford B, Sällström E, Ukeiley L, Ifju P. Structural dynamics and aerodynamics measurements of biologically inspired flexible flapping wings. Bioinspir Biomim. 2011;6(1):16009.

51. Eldredge JD, Toomey J, Medina A. On the roles of chord-wise flexibility in a flapping wing with hovering kinematics. J Fluid Mech. 2010;659:94–115.

52. Heathcote S, Gursul I. Flexible Flapping Airfoil Propulsion at Low Reynolds Numbers. AIAA J. 2007;45(5):1066–79.

53. Heathcote S, Wang Z, Gursul I. Effect of Spanwise Flexibility on Flapping Wing Propulsion. 36th AIAA Fluid Dynamics Conference, AIAA 2006-2870:1–17.

54. Ellington CP. The Aerodynamics of Hovering Insect Flight. VI. Lift and Power Requirements. Philos Trans R Soc B Biol Sci. 1984;305(1122):145–81.

55. Dudley R, Ellington CP. Mechanics of Forward Flight in Bumblebees: II. Quasi-Steady Lift and Power Requirements. J Exp Biol. 1990;148(1):53–88.

56. Willmott AP, Ellington CP. The mechanics of flight in the hawkmoth Manduca sexta. II. Aerodynamic consequences of kinematic and morphological variation. J Exp Biol. 1997;200(21):2723–2745.

57. Lehmann F-O, Dickinson MH. The changes in power requirements and muscle efficiency during elevated force production in the fruit fly Drosophila melanogaster. J Exp Biol. 1997;200(Pt 7):1133–43.

58. Engels T, Kolomenskiy D, Schneider K, Lehmann F-O, Sesterhenn J. Bumblebee Flight in Heavy Turbulence. Phys Rev Lett. 2016;116(2):28103.

59. Sun M, Du G. Lift and power requirements of hovering insect flight. Acta Mech Sin. 2003;19(5):458–69.

60. Engels T, Kolomenskiy D, Schneider K, Lehmann FO, Sesterhenn J. Bumblebee Flight in Heavy Turbulence - Supplemental Material. Phys Rev Lett. 2016;116(2):1–11.

61. Liu H. Integrated modeling of insect flight: From morphology, kinematics to aerodynamics. J Comput Phys. 2009;228(2):439–59.

62. Margaria R. Positive and negative work performances and their efficiencies in human locomotion. Int Zeitschrift für Angew Physiol einschließlich Arbeitsphysiologie. 1968;25(4):339–51.

63. Sun M, Wu JH. Aerodynamic force generation and power requirements in forward flight in a fruit fly with modeled wing motion. J Exp Biol. 2003;206(17):3065–83.

64. Gao N, Aono H, Liu H. A numerical analysis of dynamic flight stability of hawkmoth hovering. J Biomech Sci Eng. 2009;4(1):105–16.

65. Oppenheimer MW, Doman DB, Sigthorsson DO. Dynamics and Control of a Biomimetic Vehicle Using Biased Wingbeat Forcing Functions. J Guid Control Dyn. 2011;34(1):204–17.

66. Doman DB, Oppenheimer MW, Sigthorsson DO. Dynamics and control of a biomimetic vehicle using biased wingbeat forcing functions: Part II: Controller. 48th AIAA Aerospace Sciences Meeting; AIAA 2010-1024.

67. Doman DB, Oppenheimer MW, Sigthorsson DO. Wingbeat Shape Modulation for Flapping-Wing Micro-Air-Vehicle Control During Hover. J Guid Control Dyn. 2010;33(3):724–39.

68. Xinyan Deng, Schenato L, Sastry SS. Flapping flight for biomimetic robotic insects: part II-flight control design. IEEE Trans Robot . 2006;22(4):789–803.

69. Schenato L, Campolo D, Sastry S. Controllability issues in flapping flight for biomimetic Micro Aerial Vehicles (MAVs). Proc IEEE Conf Decis Control. 2003;6:6441–7.

70. Chirarattananon P, Ma KY, Wood RJ. Adaptive control of a millimeter-scale flapping-wing robot. Bioinspir Biomim. 2014;9(2):25004.

71. Shyy W, Kang C, Chirarattananon P, Ravi S, Liu H. Aerodynamics, Sensing, and Control of Insect-scale Flapping-Wing Flight. Proc R Soc A. 2016;472(2186):20150712.

72. Ristroph L, Ristroph G, Morozova S, Bergou AJ, Chang S, Guckenheimer J, et al. Active and passive stabilization of body pitch in insect flight. J R Soc Interface. 2013;10(85).

73. Padfield GD. Helicopter Flight Dynamics: The Theory and Application of Flying Qualities and Simulation Modeling. American Institute of Aeronautics and Astronautics; 2007.

74. Taylor GK, Thomas ALR. Dynamic flight stability in the desert locust Schistocerca gregaria. J Exp Biol. 2003;206(16):2803–29.

75. Cheng B, Deng X, Hedrick TL. The mechanics and control of pitching manoeuvres in a freely flying hawkmoth (Manduca sexta). J Exp Biol. 2011;214(24):4092–106.

76. Hedrick TL, Cheng B, Deng X. Wingbeat time and the scaling of passive rotational damping in flapping flight. Science. 2009;324(5924):252–255.

77. Taha HE, Tahmasian S, Woolsey C, Nayfeh AH, Hajj MR. The need for higher-order averaging in the stability analysis of hovering, flapping-wing flight. Bioinspir Biomim. 2015;10(1):16002.

78. Xiong Y, Sun M. Dynamic flight stability of a bumblebee in forward flight. Acta Mech Sin. 2008;24(1):25–36.

79. Zhang Y-L, Sun M. Dynamic flight stability of a hovering model insect: lateral motion. Acta Mech Sin. 2010;26(2):175–90.

80. Zhang Y-L, Sun M. Stabilization control of a hovering model insect: Lateral motion. Acta Mech Sin. 2011;27(5):823–32.

81. Wu JH, Sun M. Floquet stability analysis of the longitudinal dynamics of two hovering model insects. J R Soc Interface . 2012;9(74):2033–46.

82. Mou X, Sun M. Dynamic Flight Stability of a Model Hoverfly in Inclined-Stroke-

Plane Hovering. J Bionic Eng. 2012;9(3):294–303.

83. Xu N, Sun M. Lateral dynamic flight stability of a model bumblebee in hovering and forward flight. J Theor Biol. 2013 Feb;319:102–15.

84. Xu N, Sun M. Lateral dynamic flight stability of a model hoverfly in normal and inclined stroke-plane hovering. Bioinspir Biomim. 2014;9(3):36019.

85. Liang B, Sun M. Dynamic flight stability of a hovering model dragonfly. J Theor Biol. 2014;348:100–12.

86. Templin RJ. Spectrum of animal flight: Insects to pterosaurs. Prog Aerosp Sci. 2000;36(5):393–436.

87. Shyy W, Kang C, Chirarattananon P, Ravi S, Liu H. Aerodynamics, sensing and control of insect-scale flapping-wing flight. Proc R Soc London, Ser A Math Phys Eng Sci. 2016;472.

88. Ellington CP. The Aerodynamics of Hovering Insect Flight. II. Morphological Parameters. Philos Trans R Soc B Biol Sci. 1984;305(1122):17–40.

89. Etkin B. Dynamics of Atmospheric Flight. New York: Wiley; 1972.

90. Liu H, Nakata T, Gao N, Maeda M, Aono H, Shyy W. Micro air vehicle-motivated computational biomechanics in bio-flights: aerodynamics, flight dynamics and maneuvering stability. Acta Mech Sin. 2010;26(6):863–79.

91. Badrya C, Macfarlane K, Baeder J, Humbert JS. Insect Kinematics in Trimmed Flight at Low Reynolds Numbers Using CFD. In: 53rd AIAA Aerospace Sciences Meeting. AIAA 2015-0045, Kissimmee, FL; 2015. p. 1–18.

92. Weis-Fogh T. Energetics of Hovering Flight in Hummingbirds and in Drosophila. J Exp Biol. 1972;56(1):79–104.

93. Lua KB, Lim TT, Yeo KS. Scaling of Aerodynamic Forces of Three-Dimensional Flapping Wings. AIAA J. 2014;52(5):1–7.

94. Ellington CP. The Aerodynamics of Hovering Insect Flight. IV. Aeorodynamic Mechanisms. Philos Trans R Soc B Biol Sci. 1984;305(1122):79–113.

95. Leishman JG. Principles of Helicopter Aerodynamics. Second Ed. New York: Cambridge University Press, New York, USA; 2006.

96. Babinsky H, Stevens PRRJ, Jones AR, Bernal LP, Ol M V. Low Order Modelling of Lift Forces for Unsteady Pitching and Surging Wings. 54th AIAA Aerospace Sciences Meeting. AIAA2016-0290. p. 1–12.

97. Bisplinghoff RL, Ashley H, Halfman RL. Aeroelasticity. Mineola, NY: Dover Publications, Inc. 1996.

98. Fung YC. An Introduction to the Theory of Aeroelasticity. Mineola, NY: Dover Publications, Inc. 2008.

99. Andersen a., Pesavento U, Wang ZJ. Unsteady aerodynamics of fluttering and tumbling plates. J Fluid Mech. 2005;541(1):65.

100. Xinyan Deng, Schenato L, Wei Chung Wu, Sastry SS. Flapping flight for biomimetic robotic insects: part I-system modeling. IEEE Trans Robot. 2006;22(4):776–88.

101. Zhao L, Huang Q, Deng X, Sane SP. Aerodynamic effects of flexibility in flapping wings. J R Soc Interface. 2010;7(44):485–97.

102. Truong TQ, Phan VH, Sane SP, Park HC. Pitching moment generation in an insect-mimicking flapping-wing system. J Bionic Eng. 2014;11(1):36–51.

103. Doman DB, Oppenheimer MW, Sigthorsson DO. Dynamics and control of a minimally actuated biomimetic vehicle: Part I-aerodynamic model. AIAA Guidance, Navigation, and Control Conf. AIAA 2009-6160. p. 10–13.

104. Usherwood JR, Ellington CP. The aerodynamics of revolving wings I. Model hawkmoth wings. J Exp Biol. 2002;205(Pt 11):1547–64.

105. Usherwood JR, Ellington CP. The aerodynamics of revolving wings II. Propeller force coefficients from mayfly to quail. J Exp Biol. 2002;205(Pt 11):1565–76.

106. Wu JH, Sun M. Unsteady aerodynamic forces of a flapping wing. J Exp Biol. 2004;207(7):1137–50.

107. Bush BL, Baeder JD. Computational Investigation of Flapping-Wing Flight. 37th AIAA Fluid Dyn Conf. AIAA 2007-4209. p. 1–15.

108. Birch JM, Dickinson MH. Spanwise flow and the attachment of the leading-edge vortex on insect wings. Nature. 2001;412(6848):729–33.

109. Shyy W, Trizila P, Kang C-K, Aono H. Can Tip Vortices Enhance Lift of a Flapping Wing? AIAA J. 2009;47(2):289–93.

110. Birch JM, Dickinson MH. The influence of wing-wake interactions on the production of aerodynamic forces in flapping flight. J Exp Biol. 2003;206(13):2257–72.

111. Shyy W, Liu H. Flapping wings and aerodynamic lift: the role of leading-edge

vortices. AIAA J. American Institute of Aeronautics and Astronautics; 2007 Dec;45(12):2817–9.

112. Kang C-K, Shyy W. Modeling of Instantaneous Passive Pitch of Flexible Flapping Wings. 43rd Fluid Dynamics Conf. AIAA 2013-2469. p. 1-12.

113. Lehmann F-O, Gorb S, Nasir N, Schutzner P. Elastic deformation and energy loss of flapping fly wings. J Exp Biol. 2011;214(17):2949–61.

114. Sunada S, Zeng L, Kawachi K. The Relationship Between Dragonfly Wing Structure and Torsional Deformation. J Theor Biol. 1998;193(1):39–45.

115. Ol M V., Bernal L, Kang C-K, Shyy W. Shallow and deep dynamic stall for flapping low Reynolds number airfoils. Anim Locomot. 2010;46(5):321–39.

116. Kang C, Aono H, Sik Baik Y, Bernal LP, Shyy W. Fluid Dynamics of Pitching and Plunging Flat Plate at Intermediate Reynolds Numbers. AIAA J. 2013;51(2):315–29.

117. Vandenheede RBR, Bernal LP, Morrison CL, Gogulapati A, Friedmann PP, Kang C-K, et al. Experimental and Computational Study on Flapping Wings with Bio-Inspired Hover Kinematics. AIAA J. 2014;1–12.

118. de Boer a., van der Schoot MS, Bijl H. Mesh deformation based on radial basis function interpolation. Comput Struct. 2007;85(11–14):784–95.

119. Taha HE, Hajj MR, Nayfeh AH. Wing Kinematics Optimization for Hovering Micro Air Vehicles Using Calculus of Variation. J Aircr. 2013;50(2):610–4.

120. Mountcastle AM, Combes SA. Wing flexibility enhances load-lifting capacity in bumblebees. Proc Biol Sci. 2013;280(1759):20130531.

121. Ramananarivo S, Godoy-Diana R, Thiria B. Rather than resonance, flapping wing flyers may play on aerodynamics to improve performance. Proc Natl Acad Sci. 2011;108:5964–9.

122. Bluman JE, Kang C-K, Shtessel YB. Sliding Mode Control of a Biomimetic Flapping Wing Micro Air Vehicle in Hover. AIAA Atmos Flight Mech Conf. AIAA2017-1633. p. 1–16.

123. Smith RW, Wright JA. An implicit edge-based ALE method for the incompressible Navier–Stokes equations. Int J Numer Methods Fluids. 2003 Sep;43(3):253–79.

124. Wright JA, Smith RW. An Edge-Based Method for the Incompressible Navier–Stokes Equations on Polygonal Meshes. J Comput Phys. 2001 May;169(1):24–43.

125. Kamakoti R, Shyy W. Evaluation of geometric conservation law using pressure-based fluid solver and moving grid technique. Int J Heat Fluid Flow. 2004;14(7):851–65.

126. Park H, Choi H. Kinematic control of aerodynamic forces on an inclined flapping wing with asymmetric strokes. Bioinspir Biomim. 2012;7(1):16008.

127. Ellington CP. The Aerodynamics of Hovering Insect Flight. III. Kinematics. Philos Trans R Soc B Biol Sci. 1984 Feb [cited 2014 Oct 20];305(1122):41–78.

128. Ginsberg J. Engineering Dynamics. New York, NY: Cambridge University Press, New York, USA; 2008.